USE OF MULTI-TEMPORAL HIGH-RESOLUTION SAR IMAGES FOR MONITORING FLOOD SITUATION AND TYPHOON EFFECTS

多時期の高分解能SAR画像を用いた洪水状況と台風被害の監視

January 2017

Pisut Nakmuenwai

Graduate School of Engineering

CHIBA UNIVERSITY

(千葉大学審査学位論文)

USE OF MULTI-TEMPORAL HIGH-RESOLUTION SAR IMAGES FOR MONITORING FLOOD SITUATION AND TYPHOON EFFECTS

多時期の高分解能SAR画像を用いた洪水状況と台風被害の監視

January 2017

Pisut Nakmuenwai

Graduate School of Engineering

CHIBA UNIVERSITY

Table of Contents

ACKNOWLEDGEMENTS

CURRICULUM VITA

July 31, 1975   Born, Nai Mueang, Nakhon Ratchasima, Thailand

Education

1994-1997   Bachelor of Science (Forestry), Department of Forest Biology, Faculty of Forestry, Kasetsart University, Bangkok, Thailand

1998-2001   Master of Science (Forestry), Department of Forest Biology, Faculty of Forestry, Kasetsart University, Bangkok, Thailand

2013-2017   Doctoral student, Department of Urban Environmental Systems, Graduate School of Engineering, Chiba University, Chiba, Japan

Employment

2000-2002   Forest Technical Officer, Royal Forest Department, Bangkok, Thailand

2003-2005   Computer Scientist, Research and Development Section, Geo-Informatics and Survey Engineering Office, Consultant of Technology Co. Ltd. Bangkok, Thailand

2005-2010   Computer Scientist, Geo-Informatics and Space Technology Development Agency, Bangkok, Thailand

2010-Present   Senior Computer Scientist, Geo-Informatics and Space Technology Development Agency, Bangkok, Thailand

PUBLICATIONS

Nakmuenwai, P., Yamazaki, F., and Liu, W. (2017) Automated Extraction of Inundated Areas from Multi-Temporal Dual-Polarization RADARSAT-2 Images for the 2011 Central Thailand Flood. *Remote Sens.* (In Review).

Nakmuenwai, P., Yamazaki, F., and Liu, W. (2016) Multi-temporal Correlation Method for Damage Assessment of Buildings from High-Resolution SAR Images of the 2013 Typhoon Haiyan. *JDR.* Vol.11, No.3, 577-592.

Nakmuenwai, P., Yamazaki, F. (2014) Damage Investigation for The 2013 Typhoon Haiyan in The Philippines using Multi-Temporal Cosmo-Skymed Images, *The 35th International Geoscience and Remote Sensing Symposium (IGARSS)*, 2261-2264.

Nakmuenwai, P., Yamazaki, F. (2014) Extraction of Flooded Areas in The 2011 Thailand Flood from Radarsat-2 and ThaiChote Images, *The 35th International Geoscience and Remote Sensing Symposium*, 3354-3357.

Nakmuenwai, P., Yamazaki, F. (2013) Flooded Areas Extraction due to The 2011 Thailand Flood Using Radarsat-2 And Thaichote Imagery Data. *The 34th Asian Conference on Remote Sensing (ACRS)*, 8 pages.

Kaewsing, W., Nakmuenwai, P., Luckkum, M. (2012) Development of Automated Displaying System of Numerous Reports for Satellite Based Surface Water Maps. *The 33rd Asian Conference on Remote Sensing (ACRS)*, 7 pages.

Nakmuenwai, P. (2006) The Dynamic WMS Web Client Development with AJAX. *The 6th Free and Open Source Software for Geoinformatics (FOSS4G)*, 7 pages.

ABSTRACT

USE OF MULTI-TEMPORAL HIGH-RESOLUTION SAR IMAGES
FOR MONITORING FLOOD SITUATION AND TYPHOON EFFECTS

Pisut Nakmuenwai

Doctor of Engineering

Chiba University, 2017

This dissertation focuses on the application of multi-temporal high-resolution Synthetic Aperture Radar (SAR) images for detecting and monitoring the natural disasters effects. Because SAR sensors emitting microwave are independent on sunlight conditions and microwave can penetrate the cloud-cover, it can be used under all the weather conditions in the daytime and nighttime to detect natural disaster even in the bad weather environment. Although a single image could capture the event, multi-temporal images based on multiple time series provide more information in another dimension. The multi-temporal information is not only useful for the change detection, but it also provides an excellent tool to monitor the event progress. Change detection which is considering just two points in time is suitable for emergent disasters, e.g., typhoon, landslide, earthquake, and volcanic eruption. In this case, the damage assessment of buildings due to the 2013 typhoon Haiyan in the Philippines is selected to illustrate the potentiality of the interferometry SAR pairs. On the other hand, the incremental disaster needs more points in time to capture its progress. The extraction of inundated areas due to the 2011 flood in Thailand is decent to be an example for monitoring the progress of the disaster. The flood duration map was obtained from the series of dual polarization SAR images. Both the events are the biggest natural disaster in this decade and affected a broad area in those countries.

Keywords: multi-temporal SAR, flood detection, building damage detection

ABSTRACT

多時期高解像度 SAR 画像を用いた洪水のモニタリングと台風被害の抽出

Pisut Nakmuenwai

Doctor of Engineering

Chiba University, 2017

　　　センサの進歩により，高解像度の合成開口レーダ(SAR)画像が高頻度で得られるようになった。SAR センサは雲が透過できるマイクロ波を放射するため，天候に影響されず昼夜撮影できることから，災害後の緊急対応に有効である。また，多時期の SAR 画像を用いることで，地震，台風などの短期間災害による被害だけでなく，洪水などの長期間災害のモニタリングもできる。本研究は，多時期の高解像度 SAR 画像を用いて自然災害後の被害把握とモニタリングを行った。短期間の災害事例として，2013 年台風 Haiyan 前後の COSMO-SkyMed 干渉ペア画像から，フィリピンにおける建物の被害を抽出した。建物の被害状況を評価するために，2 時期の後方散乱係数の合計，差分と相関係数を融合した変化指標 Δh を提案した。その閾値より抽出された結果は，高解像度光学画像と比較し，精度の検証を行った。長期間災害の事例として，2011 年タイの洪水による浸水域の変化をモニタリングした。2011 年 9 月 2 日から 2012 年 2 月 14 日までに撮影された 30 枚の RADARSAT 画像を用いて，各画像から水域の閾値を自動的に算出する手法を提案した。各画像から抽出された浸水域の範囲と場所の変化から洪水被害の進行を観測できた。また，2011 年 12 月 21 日の画像から得られた浸水域について，光学画像と水深計のデータを用いて精度の検証を行った。本研究の結果により，多時期の高解像度 SAR 画像が災害把握における有用性を示した。

Chapter 1

Introduction

1.1. Overview

Synthetic aperture radar (SAR) imaging can penetrate clouds, providing an effective precipitation detector under a wide range of atmospheric conditions [1]. SAR is developed on microwave technology cover wavelength between 300 MHz (100cm) and 300GHz (0.1cm). The commonly used wavelengths are X-band (2.4-3.75 cm), C-band (3.75-7.5 cm), or L-band (15-30 cm), which is suitable for different application [2]. Shorter wavelength, such as X-band, is the suitable frequency for several high-resolution radar applications [3, 4]. Longer wavelength, such as C-band, is not hindered by atmospheric effects and is capable of 'seeing' through tropical clouds and rain showers [4]. Its penetration capability is limited and is restricted to the top layers with regard to vegetation canopies or soils.

SAR is a very powerful technique to detect environmental changes or help in the evaluation of natural disasters, according to it can operate under any weather conditions [1, 5]. Multi-temporal change detection is important for monitoring disasters, but data integration from two or more images which taken in a different time or different sensor condition is continual development and need to be improved [6].

1.2. Scope and objectives

This dissertation focuses on the capabilities of SAR satellite images as a primary data to monitoring natural disaster especially typhoon and floods. The optical sensor is expecting as a supporting data and validating data. According to SAR sensor provided several wavelengths which are suitable for a different objective. Thus, disaster effect should be monitored by specific wavelength. The main scope of this research is to enlarge the capability of SAR imagery data for a natural disaster in particular cases, typhoon, and floods. The specific objectives are outlined as follows:

Floods:
− Extract flood area using C-band SAR satellite data, case study Thailand flood 2011.
− Improve the accuracy of water extraction by using dual polarization instead of single polarization.
− Monitoring the floods situation by combining the extracted water areas from multi-temporal SAR images which were acquired from a different condition.

Typhoon:

- Evaluate damage to building using X-band SAR satellite data, case study typhoon Haiyan in Philippines 2013.
- Improve the damage of building evaluation efficiency by developing novel change index from two single polarization images which taken before and after the event.

1.3. Outline of this research

This thesis exhibits all contents in to 6 chapters. Each chapter is related as shown in a diagram of **Figure 1-1**. The contents are outlined in more detail as follows:

Chapter 2: This chapter presents and describes aspects of the natural disaster and SAR satellites. The primary natural disaster which is discussed in this section is tropical cyclones and its effects, floods caused by torrential rains, and damage to buildings resulting from high wind. There are two SAR satellites which were use in this study, RADARSAT-2, and COSMO-SkyMed. The satellite information and data pre-processing are also provide in this chapter.

Chapter 3: This chapter examines a novel extraction method for SAR imagery data of widespread flooding, particularly in the Chao Phraya river basin of central Thailand, where flooding occurs almost every year. Multi-temporal dual-polarized RADARSAT-2 images were used to classify water areas using a clustering-based thresholding technique, neighboring valley-emphasis, to establish an automated extraction system.

Chapter 4: This chapter is the reproduction of section 3 for flood extraction in 2016, newer acquired images. According to flood in Chao Phraya river basin is a corny event, flood situation assessment must regularly be performed. Proving the proposed method can work correctly and efficiently for this area, flood in 2016 was selected to be processed in the same technique. Each image in this section was clipped by water references to determine the global threshold, and then calculate the global threshold for water extraction.

Chapter 5: In this section, damage caused by Typhoon Haiyan in the city of Tacloban, Philippines was extracted from COSMO-SkyMed imagery data using a thresholding operation. A multitemporal correlation map obtained from a color composite of the backscattering coefficients and their correlation coefficients is used to indicate changes. The results were compared with WorldView-2 satellite images to assess coastal erosion and damage to buildings specifically.

Chapter 6: The general conclusions are drawn in the final section, which provides discussions obtained in this research. Please download this article as an open access publication at http://www.mdpi.com/2072-4292/9/1/78
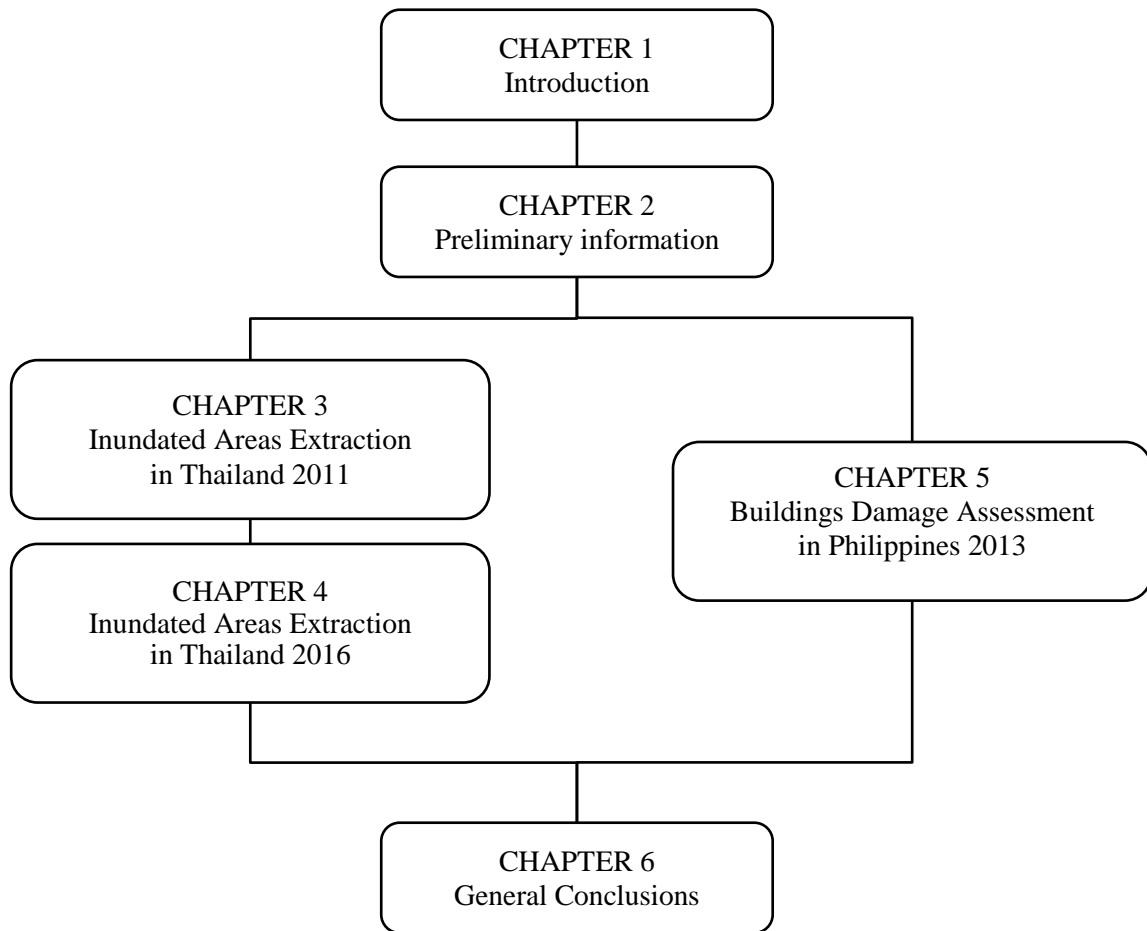
Figure 1-1 Flowchart of the dissertation

Chapter 2
State of the art and theoretical concepts

2.1. Natural Disasters

A natural disaster is any catastrophic event conducted by the natural processes, causing loss of life or property damage, and typically leaves some economic damage [1]. Natural disasters could be classified into several type geological catastrophes, hydrological disasters, meteorological disasters, health disasters [2]. The dissertation studied in these thesis unique to just only tropical cyclones and its effects as a floods situation.

2.1.1. Tropical cyclones

Tropical cyclones are "cyclonic" weather systems composed of the major rotating masses of thunderstorms. Tropical refers to the geographical origin of these systems, which form almost exclusively over tropical seas. Cyclone refers to their cyclonic nature; a wind direction of circulation is due to the Coriolis Effect. In the Southern Hemisphere, the wind blowing clockwise, while the Northern Hemisphere it blowing counterclockwise. These systems form over the warm ocean waters of the tropics and subtropics usually between the latitudes of 30°N and 30°S. Tropical cyclones originate and move within 7 tropical cyclones "basins" worldwide, 4 above the equator and 3 below the equator shown in **Figure 2-1** [3].

Tropical cyclones are classified into three main groups, based on intensity. The tropical depressions, tropical storms are groups of low and middle wind speed respectively. The third group is more intense storms, whose name depends on the region, "hurricanes" in the North Atlantic, "typhoons" in the western North Pacific, and "cyclones" in the Indian Ocean and Australasia. The National Hurricane Center (NHC Miami), the Regional Specialized Meteorological Center (RSMC Tokyo), and the Central Pacific Hurricane Center (CPHC Honolulu) classify hurricane or typhoon that has winds speeds exceed 119km/h into 5 categories; the higher value is the most sustained winds. All tropical cyclone classifications from various organizations are described in **Figure A-1** [4].

A typhoon is a tropical cyclone that develops in the Northwestern Pacific Basin, the western part of the North Pacific Ocean, between 180°E and 100°E. Accounting to almost one-third of the world's annual tropical cyclones, this tropical cyclone basin is the primary region and the most active on Earth. Typhoon paths follow three general directions. The straight track, a general westward path affects the Philippines, southern China, Taiwan, and Vietnam. Parabolic recurving track, Storms recurving affect the eastern

Philippines, east china, Taiwan, Korea, Japan, and the Russian Far East. The northward track, the storm follows a northerly direction from the point of origin, only affecting small islands [4].

The main effects of tropical cyclones include torrential rains, high wind, large storm surges at landfall and tornadoes. Tropical cyclones make the most significant effects when they cross coastlines by making landfall. The destruction from a tropical cyclone depends mainly on its intensity, its size, and its location. Typhoon Haiyan landfall in the central Philippines on Nov. 8, 2013, is the most intense tropical cyclones on record with wind speed 195 miles per hour (314 km/h) [5].

2.1.2. Floods

Flood is an overflow of a large amount of water beyond its normal limits, especially over what is usually dry land [6]. Flooding can occur due to various phenomena. Riverine flood (Fluvial flood) occurs when excessive rainfall over an extended period of time in the upstream areas of a catchment causes a river to exceed its capacity. Coastal flood (Surge flood) occurs when flat land is flooded by storm surges, sea level rise or tsunami wave. Pluvial (Surface Flood) occurs when heavy rainfall creates a flood event independent of an overflowing water body [7, 8]. Due to almost of the flood in the world generally caused by heavy rain, it's usually occurring related to tropical cyclone as shown in **Figure2-2** [7,9].

2.2. SAR Satellites

Although in a typical SAR application, a single radar antenna is attached to an aircraft or spacecraft sensor, most land-surveying applications are now carried out by satellite observation. There are two SAR constellation satellite data were be used in this dissertation.

2.2.1. RADARSAT

RADARSAT is a constellation of Canadian remote sensing earth observation satellite operated by the Canadian Space Agency (CSA). This program has consisted of RADARSAT-1 (1995-2013), and RADARSAT-2 (2007-present). Both are equipped with a high-resolution SAR instrument operating in C-Band. Both satellite orbits are Sun-Synchronous Orbit (SSO) at altitude 793-821km for RADARSAT-1 (RS1), and 798km for RADARSAT-2 (RS2). Although the exact revisit time is 24 days, observation on the left- and right-looking gives complete coverage with is 2-3 days [10].

The RS1 observes only single HH polarization on right-looking providing the highest image resolution at 8m x 8m, while RS2 can observe with full polarization (HH, HV, VV, and VH) event right- or left-looking providing the highest image at 1m x 3m. The RS2 imaging can be carried out in one of several different beam modes. Each mode offers a unique set of imaging characteristics. The ScanSAR beam mode
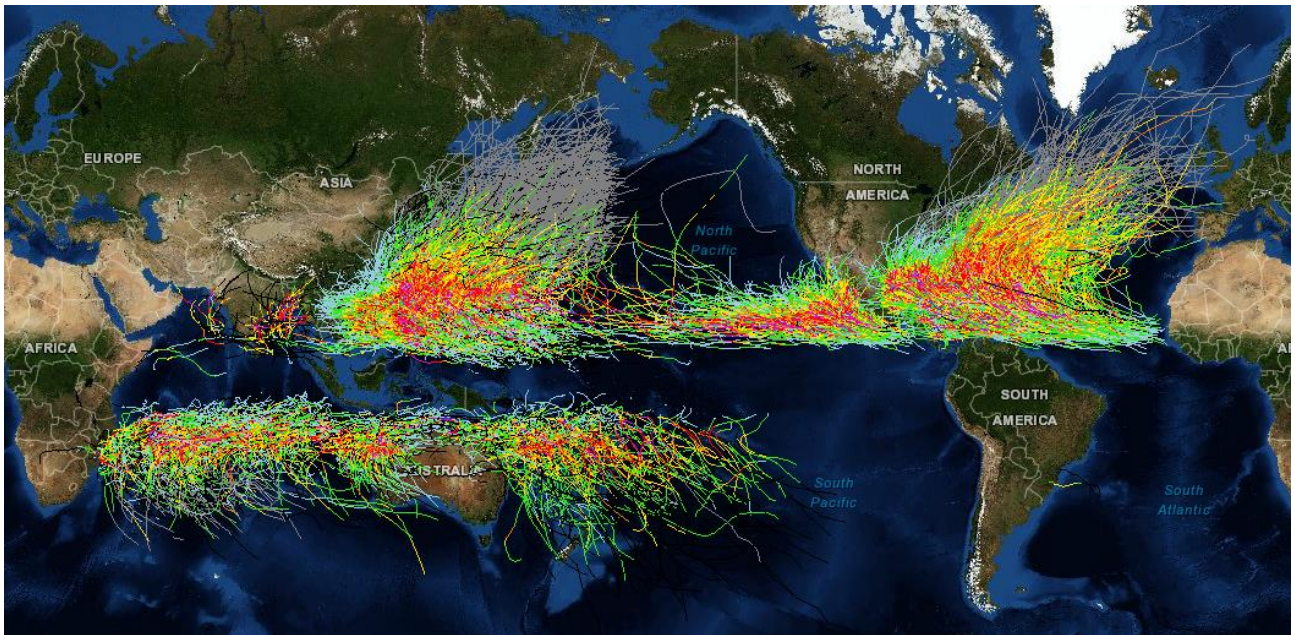
Figure 2-1. Global cyclone tracked in 1848-2013. The warmer colors indicate stronger winds.

Source: https://geozoneblog.files.wordpress.com/2014/05/globalwrappedclipped.png
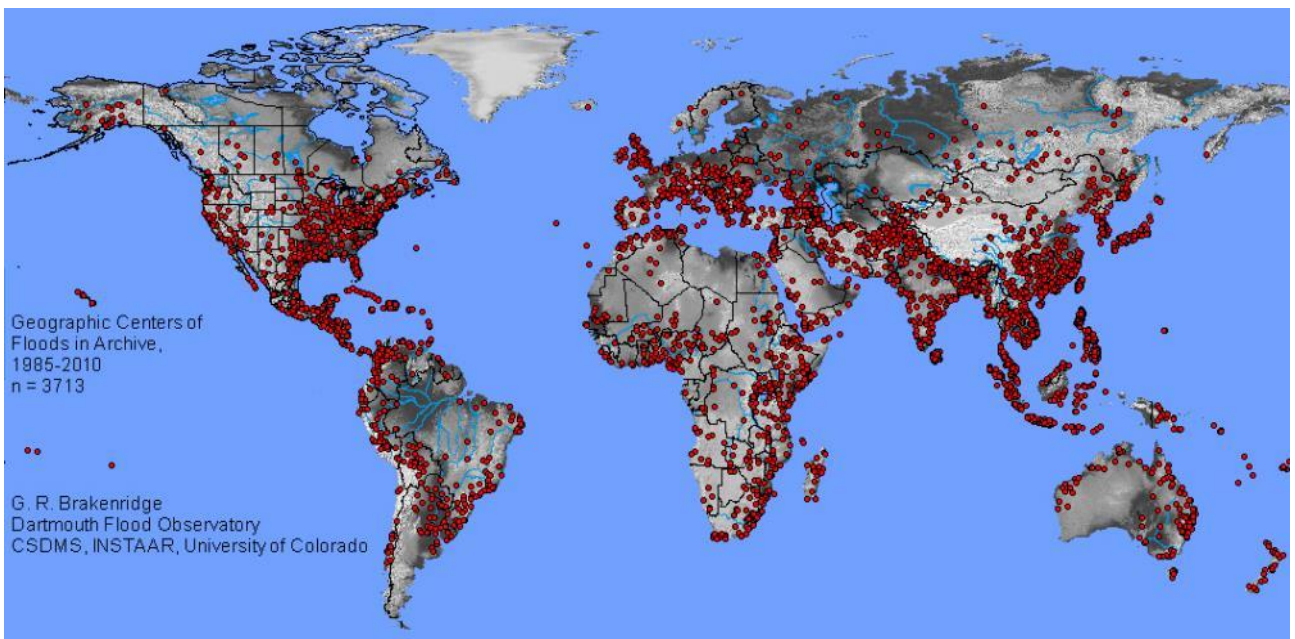
Figure 2-2. Geographic Centers of floods in the Flood Archive GIS file, 1985-2010

Source: http://floodobservatory.colorado.edu/Archives/index.html
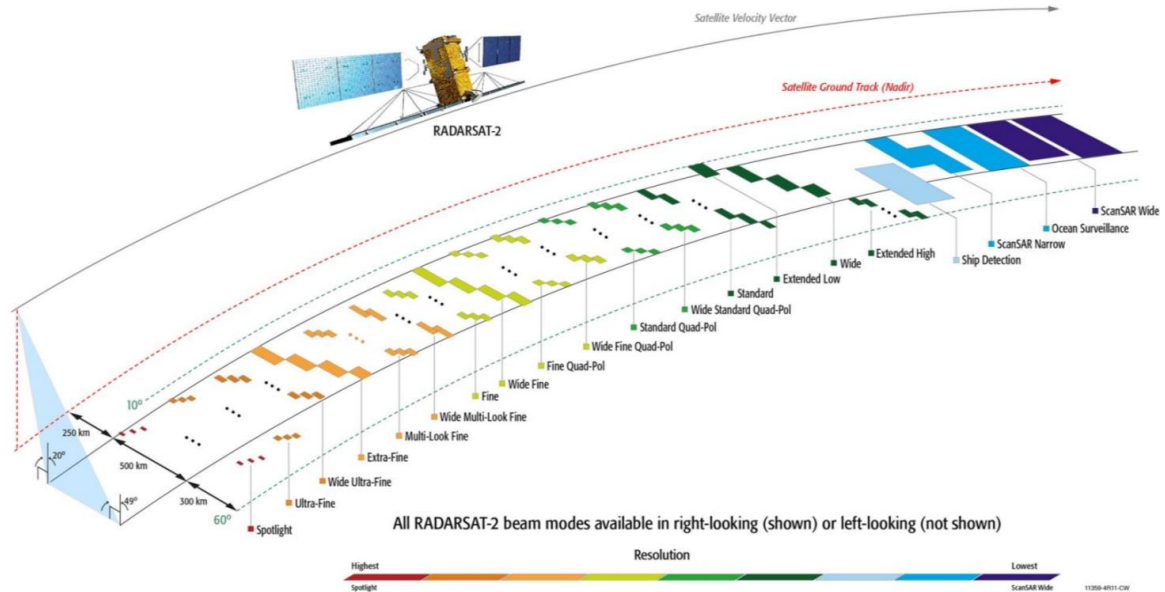
Figure 2-3. RADARSAT-2 SAR Beam Modes

Source: RADARSAT-2 Product Description, 2016

is widest swath width with the lowest resolution at around 100m. The Spotlight beam mode is narrowest swath width with the highest resolution at around 1m. The RS2 beam mode is shown in **Figure 2-3,** and its all summary, and product characteristics are shown in **Figure A-2**. Each beam mode has nominal resolutions variant by incident angle shown in **Figure A-3** [11, 12].

2.2.2. COSMO-SkyMed

COSMO-SkyMed (Constellation of small Satellites for the Mediterranean basin Observation) is an Earth observation satellite system intended for both military and civilian use, funded by the Italian Ministry of Research and Ministry of Defense and conducted by the Italian Space Agency (ASI). This constellation consists of four identical medium-sized satellites equipped with X-band SAR sensor. The first and second satellites were launched in 2007, the third one was 2008, and the last one was 2010. All satellite orbits are Sun-Synchronous Orbit (SSO) at altitude 620km. According to the orbit, the cycle is 16 days for each satellite; the revisit frequency is 8 days for 2-satellites constellation and 4 days4-satellites constellation.

The COSMO-SkyMed (CSK) satellites have three basic types of imaging modes. The spotlight is a high-resolution mode collected over a small area. Stripmap is a medium-resolution mode obtained over long, continuous swaths. ScanSAR is a low-resolution mode that creates extra-wide swaths. Each mode has two subtype modes. However, the SPOTLIGHT1 which is the highest resolution mode is military-only mode. Thus, the highest resolution available for commercial use is SPOTLIGHT2 at 1m. The incidence angle range is 25° to 59° for all modes. The 3 acquisition modes of the COSMO-SkyMed sensor and its characteristics are shown in **Figure 2-4**.
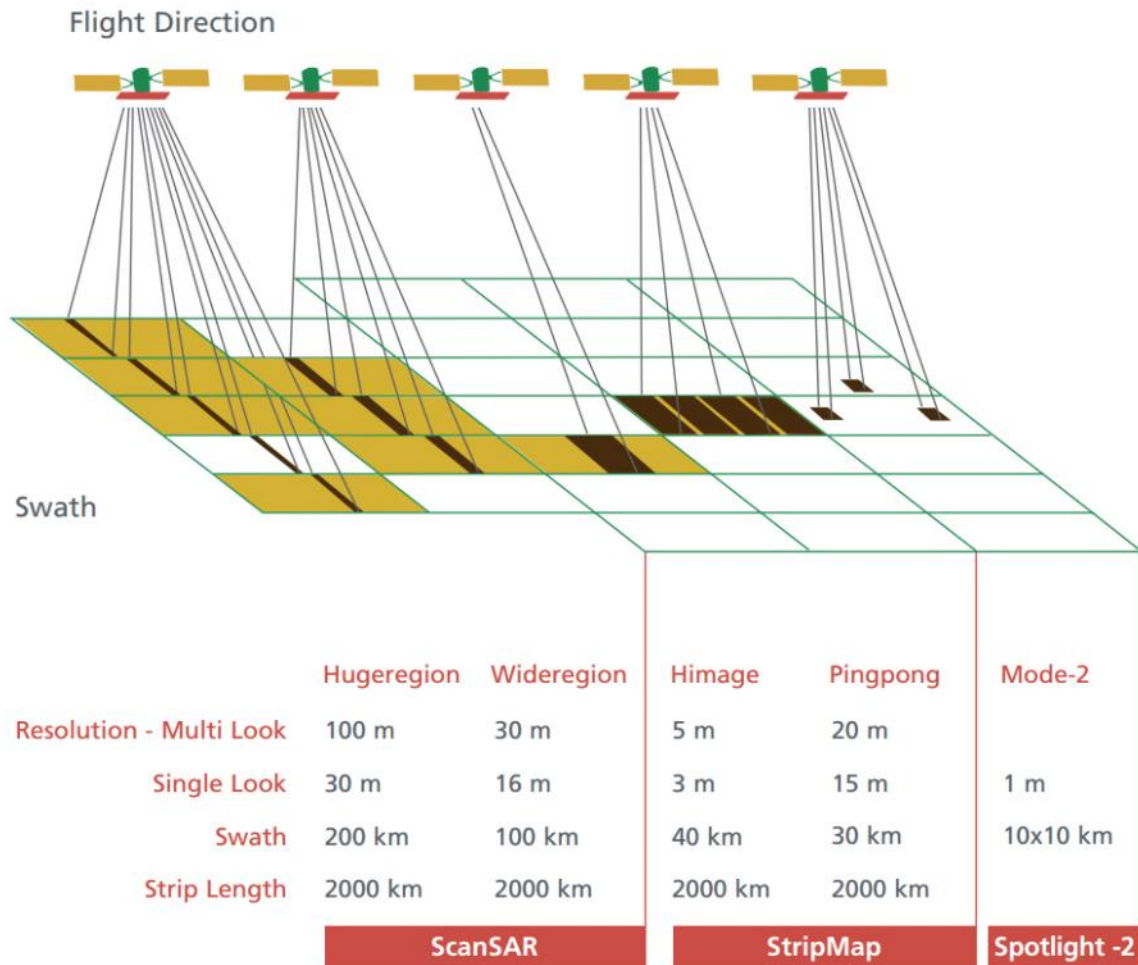
Figure 2-4. The 3 acquisition modes of the COSMO-SkyMed sensor.

Source: http://www.e-geos.it/products/pdf/e-GEOS_COSMO-SkyMed.pdf

2.3. SAR Pre-processing

2.3.1. Radiometric Calibration

The SAR calibration objective is to provide imagery that its pixel value can directly represent the radar backscatter of the reflecting surface. Although uncalibrated SAR imagery is sufficient for qualitative use, calibrated SAR images are essential to the quantitative use of SAR data.

A typical SAR level-1 image does not include radiometric corrections and significant radiometric bias remains. Therefore, it is necessary to apply the radiometric correction to SAR images. The radiometric correction is needed for the SAR images comparison acquired from the same sensor but different modes, or acquired at different times, or acquired with different sensors.

The operator performs different calibrations for each SAT satellite deriving the sigma naught images. Optionally gamma naught and beta naught images can also be created. For SAR satellites using in this dissertation are described as follow.

Radarsat-2: The operator performs absolute radiometric calibration for Radarsat-2 products by applying the sigma0, beta0 and gamma0 look-up tables provided in the product. For Radarsat-2 product calibration algorithm, the reader is referred to [13].

Cosmo-SkyMed: The operator performs absolute radiometric calibration for Cosmo-SkyMed products by applying few product factor corrections. For Cosmo-SkyMed product calibration algorithm, the reader is referred to [14].

2.3.2. Speckle Filter

An ideal speckle filter must satisfy to the following specifications [15]:

1) To preserve accurately the local mean value of the radar reflectivity.

2) To smooth homogeneous image areas as much as possible and reduce the of the radar image.

3) To preserve texture as much as possible where it exists in the image.

4) To preserve and denoised image structures (contours, lines) as well as the quasi-deterministic responses due to corner reflector effects.

5) To minimize possible prevent loss in spatial resolution during the process.

The most common and efficient speckle filtering techniques are adaptive speckle filters for single-channel detected SAR images using variants of the statistical speckle model. They also use several statistical estimators to restore the radar reflectivity, e.g., Minimum Mean Square Error (MMSE) estimators (e.g. Lee et al. filter, Kuan et al. filter, etc.), autoregressive estimators (e.g. Frost et al. filter), Bayesian estimators (e.g. Gamma-Gamma and DE-Gamma MAP filters) [15].

Lee and Kuan's filters are locally adaptive linear MMSE estimators. Lee filter is identical to the independence of noise and signal in the model used by the Kuan et al. filter. Lee uses the unit mean uncorrelated multiplicative speckle module. A linear approximation is made by developing an additive noise model different of the multiplicative speckle model used in Equation (1) and Equation (2) [16]:

$$\hat{Y}(t) = \bar{I}(t) + W(t)[I(t) - \bar{I}(t)] \tag{1}$$

$$W(t) = 1 - \frac{C_v}{C_I} \tag{2}$$

when $\hat{Y}(t)$ is the filtered image value

$\bar{I}(t)$ is the mean of I(t)

C_v is coefficient of variance of speckled image

C_I is the coefficient of variance of noise-free image

2.3.3. Terrain Correction

Mostly SAR image is side-looking observation which occurs foreshortening and layover effects. A mountaintop reaches the sensor earlier the foot of the mountain. This results in the common look of mountains seem to fall over towards the sensor. The range doppler terrain correction operator is implemented from orthorectification method. The available orbit state vector information in the metadata and topographical variations on the surface of the earth as digital elevation model (DEM) are applied to the the original image. After terrain correction, SAR image position will be closer to the real world geometry. The final product is able to overlay layers from another source [17].

In this dissertation, the most popular DEM, Shuttle Radar Topography Mission (SRTM) was used in terrain correction process for all SAR images. The SRTM DEM data originally produced by NASA for the entire globe. The first release of SRTM data in 2003 is 1-arc second tiles (approximately 30m at the equator) for the United States, but the rest of the world is 3-src second tiles (approximately 30m at the equator) [18].

2.3.4. Coregistration

SAR interferometry requires a pixel-to-pixel match between common features in SAR image pairs. Thus coregistration, the alignment of two SAR images is an essential step for the accurate determination of multi-temporal analysis, e.g., change detection, phase difference and for noise reduction.

The SAR coregistration procedure consists of two main stage, coarse coregistration and finds coregistration. The first step is pixel level accuracy. This technique is searching for coarse image offsets and shifting the slave image. The second phase is fine coregistration for subpixel accuracy. This method is searching for subpixel tie points, fitting transformation equations, and resampling the slave image [19].

Chapter 3

Automated Extraction of Inundated Areas from Multi-Temporal, Dual-Polarization RADARSAT-2 Images of the 2011 Central Thailand Flood

This study examines a novel extraction method for SAR imagery data of widespread flooding, particularly in the Chao Phraya river basin of central Thailand, where flooding occurs almost every year. Because the 2011 flood was among the largest events and of a long duration, a large number of satellites observed it, and imagery data are available. At that time, RADARSAT-2 data were mainly used to extract the affected areas by the Thai government, whereas ThaiChote-1 imagery data were also used as optical supporting data. In this study, the same data were also employed in a somewhat different and more detailed manner. Multi-temporal dual-polarized RADARSAT-2 images were used to classify water areas using a clustering-based thresholding technique, neighboring valley-emphasis, to establish an automated extraction system. The novel technique has been proposed to improve the classification speed and efficiency. This technique selects specific water references throughout the study area to estimate local threshold values and then averages them by an area weight to obtain the threshold value for the entire area. The extracted results were validated using high-resolution optical images from the GeoEye-1 and ThaiChote-1 satellites and water elevation data from gaging stations.

3.1. Introduction

Floods occur almost every year in Thailand and cause unfavorable situations. The worst flooding in the last five decades occurred in 2011 [1]. The World Bank has estimated the damage and the losses due to this flooding at approximately THB 1.43 trillion (USD 46.5 billion) in total, while the recovery and reconstruction needs were estimated to be THB 1.5 trillion (USD 50 billion) over the five-year period [2]. This flood event spread throughout the northern, northeastern, and central provinces of the country. The flooding caused heavy economic impacts by disturbing industrial production in the affected areas and the supply chains of industries worldwide [1–3]. In this study, satellite imagery data, which can effectively extract information in large-scale disasters, were introduced to evaluate the extent of the flood. Among other types of sensors, synthetic aperture radar (SAR) sensors can operate during the day and night and under all weather conditions [4]. RADARSATs, which are Canadian SAR satellites with C-band radars operating at a wavelength of 5.6 cm, have been mainly used for flood monitoring in Thailand since 2000 (RADASAT-1, RS1) and 2008 (RADARSAT-2, RS2) [5,6]. ThaiChote-1 (TH1), the first satellite of Thailand, has been used to provide optical support under clear sky conditions since 2004.

Earth terrain surfaces are considered to be rough at radar wavelengths and exhibit diffuse scattering with moderate backscatter. In contrast, water surfaces are generally smooth and can be regarded as specular reflectors that yield small backscatter at radar wavelengths. As a consequence, the surrounding terrain corresponds to brighter intensities in SAR images, whereas water is regarded as low intensity area. Therefore, SAR images are considered to be very effective and have been extensively used for water and flood mapping [7,8].

Single co-polarized HH (horizontal transmit and horizontal receive) SAR images are the most common and are useful for determining water and flood areas. Especially for C-band radars, this is the preferred polarization for mapping flooded vegetation because it maximizes canopy penetration and enhances the contrast between forests and flooded vegetation [9–12]. Although it has been used in many cases, but with respect to water surfaces, obstacle cover, floating objects, and wind ripples, affect SAR backscatter, preventing C-band from returning good results. Dual and full polarizations have been employed to enhance capability [11–13]. Dual-polarizations can potentially be used to detect and map vegetation water content (VWC) in forested areas and more reliably distinguish open water surfaces affected by wind. When an SAR image is acquired in lighter winds or under smooth water surface conditions, the HH co-polarization has been shown to be the most suitable for mapping surface waters. However, when wind or surface water roughness is present, the single cross-polarized HV (horizontal transmit and vertical receive) often yields better results for water extraction [14–16]. Unfortunately, the Thai government only uses HH polarization in most cases to monitor flood events. Therefore, the intent of this study is to improve the effectiveness of mapping surface waters by combining the depolarization information in HV with HH as the total backscatter.

Deriving the extent of inundation from a single SAR image has been carried out using several methods, e.g., pixel-based classification [17–24], segment-based classification with region growth [25–28], and mixing between the two methods [19,29,30]. The most common and efficient way is thresholding, which is a pixel-based operation. In computer vision and image processing, thresholding was introduced to reduce a gray level image to a binary image, foreground and background. The algorithm assumes that the image histogram is distributed in two classes or has a bimodal distribution. Flooded areas or foregrounds are separated from the background by a constant threshold value. Manual threshold-value selection may be faced with a problem; it is hard to judge the most suitable value objectively. Automatic thresholding methods have been introduced to overcome this issue and to improve the classification speed or efficiency. Several techniques have been proposed to determine threshold values for SAR images [17–22]. The optimum global threshold value can be obtained from the minimum within-class variance [17,18] or the minimum error thresholding [19–21], whereas some techniques look for local threshold values using auxiliary data, e.g., elevation and slope [22–24]. In this study, we selected a threshold value by a modification of the Otsu's method. The Otsu's method is a clustering based thresholding, one of the most referenced methods [31]. This technique establishes an optimum threshold by minimizing the weighted sum of within-class variances of the

foreground and background pixels [17,18,31]. This technique is robust for noisy images with Gaussian noise and is the best for presenting the inter-region contrast of SAR images [17,18].

To detect floods over large-scale areas such as the Chao Phraya river basin, identifying the global threshold value from the histogram of the entire image is almost impossible because this histogram has a unimodal distribution. The global threshold value is estimated in an indirect way as the arithmetic average of local threshold values for small areas. First, the image is divided into small portions, and then only those portions that have a bimodal distribution histogram are selected as representative. This technique can be carried out by the fully automated division of an image by a certain pattern, the bi-level quad tree [19–21]. However, the advantage of systematic hierarchical image division is location independent. It is time consuming, particularly for processing multi-temporal images in the same place, and tiled pieces at different times may not be in the same place. A permanent representative area is proposed in this study to decrease processing time and to monitor local water bodies in a time series. This is much more suitable for Thailand because floods occur almost every year.

Because the Chao Phraya river basin is located in a large flat plain, inundation always remains for an extended period of time. The damage caused by flooding depends not only on the water depth but also on the flood duration. In 2011, the inundation depths ranged between 0.6 m and 4.9 m, with an average of 2.2 m, and the mode (most frequent value) was 2.5 m. Fifty-seven (57) days was the average inundation duration, which ranged from 3 to 120 days and had a mode of 60 days [3]. The flooded areas could be captured remotely by a single satellite image, and the duration could be obtained by monitoring the flooded areas in a sequence of time. However, water depth requires auxiliary data for processing, e.g., a digital elevation model (DEM). In this study, estimating water depth was set aside for future work. Thus, only the inundation area and duration are studied in this article. Working with multi-temporal SAR images, it is very difficult to obtain images in the exact same conditions, e.g., satellite position, look-side (right/left), and incidence angle. Several methods must be introduced to normalize multi-temporal images prior to analysis [32,33]. In contrast, the proposed method, which obtains the threshold value from water references, is independent of the acquisition condition, and there is no need to normalize the images [19–21].

3.2. Study Area and Imagery Data

This paper focuses on the Chao Phraya river basin in the central part of Thailand, which has an area of approximately 7400 km2. The basin was assigned as a regularly inundated area by the Thai government. The city of Ayutthaya, which is approximately 16.5 km in width and 21.0 km in length and includes the Ayutthaya Historical Park and the Rojana and Hi-Tech Industrial Parks, was selected as a validation area for extracting water bodies during the 2011 Thailand flood, as shown in **Figure 3-1**.

The imagery data acquired by RADARSAT-2 (RS2) during that event have several beam types, i.e., Wide1 (W1), Wide2 (W2), Wide3 (W3), SCNA (W1 + W2), and SCNB (W2 + S5 + S6). The radar frequency, resolution, and incident angle varied depending on the beam type. Most of the images were taken in the HH and HV dual-polarization mode, and 30 images using that polarization were selected. The images were observed either from the ascending (ASC) or descending (DES) path. A summary of the image properties is presented in **Table 3-1**, and their color composite maps are shown in **Figure 3-2**. Because the swath width and revisit time of the satellite are limited, only some of the images could capture the whole study area.

Two optical images were also used for validation. A GeoEye-1 (GE1) image was prioritized because it had a higher resolution and was taken on 22 November 2011, which was the nearest in time to one of the RS2 images. The pan-sharpened GE1 image had four multispectral bands with a 1.0-m resolution. ThaiChote-1 (TH1) images are also important because they are used as common data. A pan-sharped TH1 image has a multispectral band with a 2.5-m resolution. A TH1 image was taken on 25 November 2011. Another TH1 image was taken prior the flood on 12 December 2009. That image was used to assess the environment in the dry season but was not used in the analysis process. All the optical images will be shown in the accuracy assessment section.

3.3. Methodology and Results

The methodology used in this study is comprised of two parts. The main part is an automated system that extracts water bodies and produces flood duration maps. The second part is an accuracy assessment, which is a process to measure the efficiency of the main part using optical images as truth data. That part did not need to be implemented in the automated system. The main part begins with preparing RS2 images by the radiometric calibration using the lookup tables provided in these products, the Refined Lee speckle filtering [34,35] with a window size of 5×5 pixels, and the terrain correction using an SRTM 90-m DEM. Radiometric calibration provides images in which pixels can be directly related to the radar backscatter of the scene by applying the sigma naught, beta naught, and gamma naught lookup tables provided in the product [32]. The pre-processing was performed using the Sentinel Application Platform (SNAP) software program. Next, RS2 images were clipped by the study area and then temporarily cut again into specific segments throughout the study area. Those particular segments were defined as water references, as mentioned in the next section. The automatic thresholding was applied to each water reference one at a time to estimate a local threshold value. In that step, water references with unimodal distribution histograms were rejected. The local threshold values were weight-averaged by area to estimate the global threshold value. Finally, the global threshold value was applied to the whole image to extract the water bodies. The flood duration map is an auxiliary product for flood management and is calculated from the cumulative days of water bodies. All these processes were developed using a Python script and applicable modules, e.g., the Geospatial Data Abstraction Library (GDAL) for reading and writing
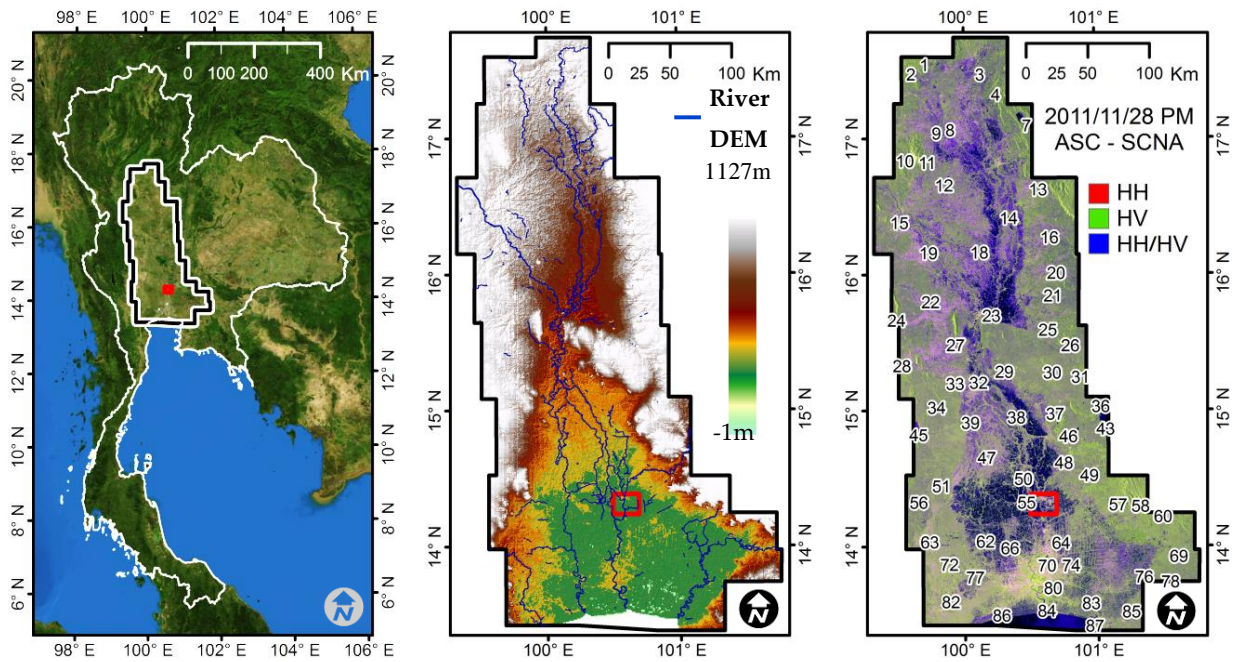
Figure 3-1. Map showing the study area (**left**), where the black border delimits the Chao Phraya river basin in central Thailand, and the red square delimits Ayutthaya City. Topographic map (**middle**), with main streams on the DEM. Water reference map showing 87 water references throughout the study area on a RADARSAT-2 image (**right**).

Table 3-1. Summary of the RADARSAT-2 image data properties used in this study.

Beam / Swatch Position	Resolution (m)	Swath Wide (km)	Pixels/ Lines	Incident Angle (degrees)		Number of Scenes	
				Near	Far	Asc.	Des.
W1 (Wide1)	12.5	170	12,930	20.0	31.9	-	5
W2 (Wide2)	12.5	150	12,930	30.6	39.5	-	1
W3 (Wide3)	12.5	130	12,930	38.7	45.3	2	-
SCNA (ScanSAR W1 + W2)	25.0	300	12,000	20.0	39.5	7	6
SCNB (ScanSAR W2 + S5 + S6)	25.0	300	12,000	30.6	46.5	4	5
Total						13	17
						30	
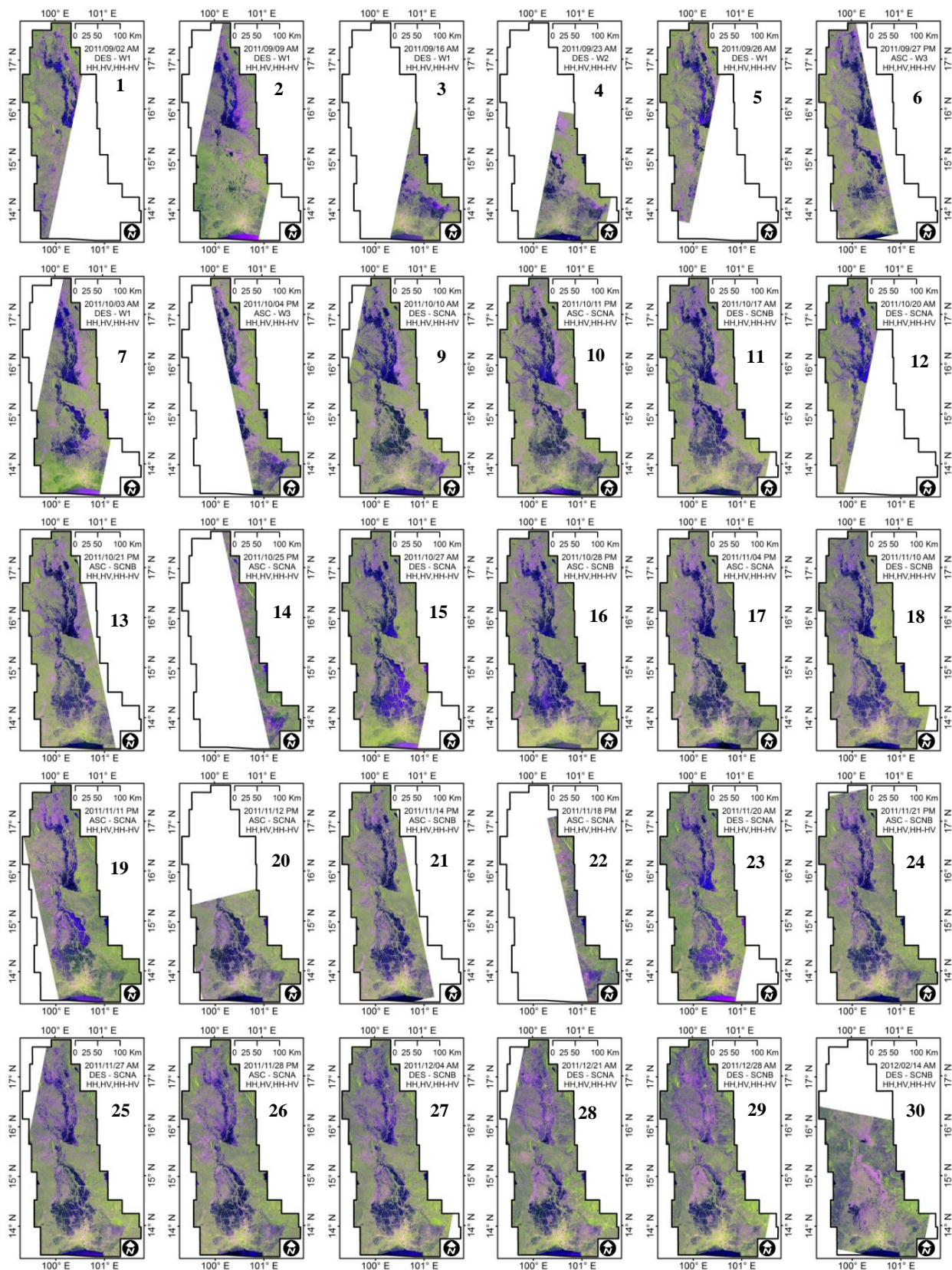
Figure 3-2. RADARSAT-2 color composite (HH as red, HV as green, and HH/HV as blue) images taken during the 2011 Thai flood event from the beginning to end.
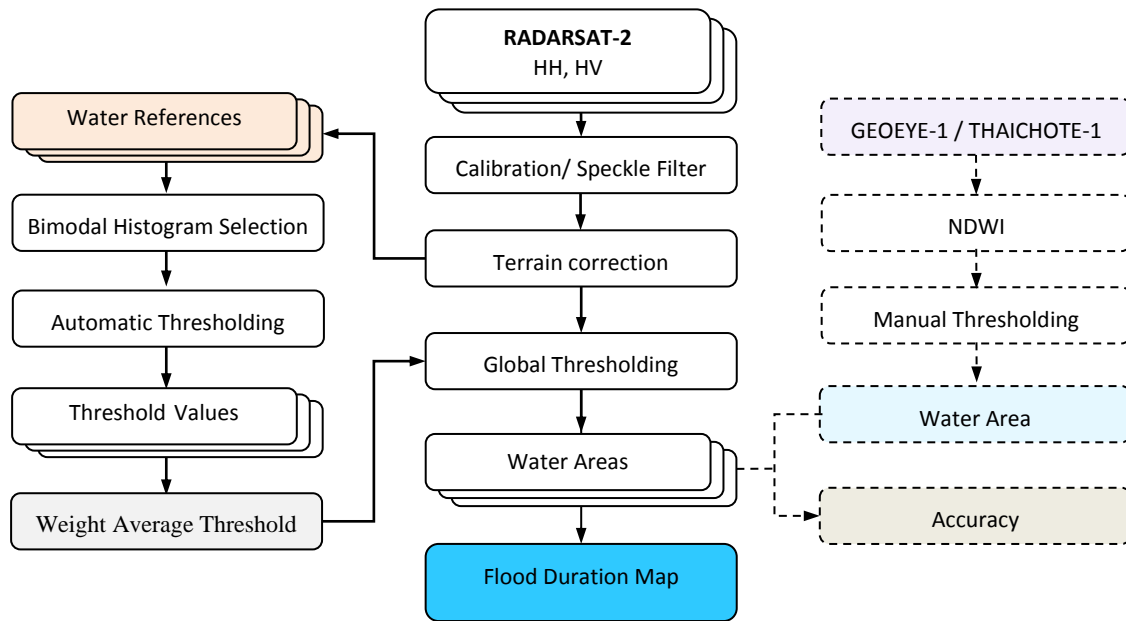
Figure 3-3. Work flow diagram for automatic flood extraction for RADARSAT-2. The optical image procedure shown by the dashed lines was used for a one-time accuracy assessment.

image data, NumPy for numerical calculation, and Matplotlib for plotting histograms. NumPy is the fundamental package for scientific computing with powerful N-dimensional array objects and linear algebra. Matplotlib is 2D and 3D plotting library which produces quality figures under interactive environments.

The purpose of the accuracy assessment was to measure the efficiency and accuracy of the final results by comparing the water areas extracted from the SAR images (RS2) with those from the optical images (GE1 and TH1). The backscattering coefficient was used for the SAR images, and the Normalized Difference Water Index (NDWI) was used for the optical images. Although the RS2 images were processed using automatic thresholding, the GE1 image was processed using manual thresholding. The RS2 and TH1 results were compared with the GE1 image to determine the most accurate thresholding. The work flow diagram used in this study is shown in **Figure 3-3**.

3.3.1. Water References and Histogram Analysis

Applying automatic clustering-based thresholding to a large area may return unsatisfying results because its histogram is not bimodally distributed [31]. This problem occurs when the ratios of the water and non-water areas are very different. A novel technique was implemented in this study to overcome this problem by applying automatic thresholding to specific smaller areas located throughout the study area.

Those small areas were defined as water references, which can be used for any satellite images acquired on a different date and time.

All the water references were selected using the following criteria: having an area larger than 320,000 m2 (512 pixels for a resolution of 25.0 m, and 2048 pixels for a resolution of 12.5 m), containing water throughout the year, not facing a flood situation, located on flat ground as much as possible, and having a water and non-water cover ratio of nearly 1:1. An irregular shape is allowed. In this study, an elliptical shape was preferred because it was easy to maintain the ratio of the water and non-water proportions. The 87 water references were selected from different types of water bodies, natural and man-made. Their locations are shown in **Figure 3-1** (right).

Because not all of the RS2 images covered the entire study area and included all the water references, only those water references whose entire areas were covered by each RS2 image were taken into account. The number of water references and their covering areas for each image are shown in **Table 3-2**. It was impossible to show all of them in this article, and thus only 10, taken on 28 February 2011, are shown in **Figure 3-4**. Smooth water surfaces are shown in black for the HH, HV, and HH + HV polarizations and in deep blue for the color composites of HH, HV, and HH/HV. "HH + HV" denotes the sum of the backscattering coefficients as the total backscattering, and "HH/HV" denotes the ratio of the backscattering coefficients as the relative backscattering. Both values were calculated on a linear scale but are presented on a logarithmic scale (dB).

The histogram plots shown in **Figure 3-4** were obtained from the RS2 images and were clipped by the selected water reference within the red elliptical boundary. The blue curve shows the HH + HV backscattering coefficient, the red curve shows the HH backscattering coefficient, and the green curve shows the HV backscattering coefficient. Theoretically, these histograms should display a bimodal distribution, but some of them were found to have unimodal distributions. Examples include water surfaces covered by floating or emerged plants or surface waves caused by strong winds. These situations cause a larger than normal amount of SAR energy to be reflected back to the sensor [11–13]. This effect can be observed in the sample images for water references 024, 028, 063, and 076.

By considering the peaks, valleys, and curvatures of the smoothed histograms, the water references with unimodal distributions were rejected, and only those with bimodal distributions were taken into account. The bimodal occurrences for the HH and HH + HV polarizations are shown in **Table 3-2**. This number indicates the occurrence probability of the bimodal distribution for each image. In that sense, HH + HV is more likely to have a bimodal distribution and is more suitable for automatic classification. In other words, the HV polarization can improve the efficiency of water surface extraction. Thus, the extracted water areas presented in this article were derived from HH + HV.

3.3.2. Automatic Thresholding

Otsu's method (OT) is one of the best threshold selection methods for general gray-level images. This technique chooses the threshold value of the minimum within-class variance (σ_W^2) or the maximum between-class variance (σ_B^2) in equation (1). Although this method can obtain satisfactory segmentation results in many cases, it is basically limited to images with background and foreground Gaussian distributions of equal variance. Therefore, images that do not meet this criterion may return unsatisfactory results, especially when the gray level histogram is unimodal or close to a unimodal distribution [33].

To address this weakness, many modifications of the Otsu method have been proposed. For example, the valley-emphasis method (VE), modified by weight σ_B^2 with p(t), the complement of a probability at a threshold value t, causes the valley in the histogram to be more likely to be better determined. The neighborhood valley-emphasis (NE) is an improvement of the valley-emphasis method by weighting σ_B^2 with the neighborhood information in n = 2m + 1 intervals at the threshold value t as in equation (2). The result is closer to the valley of the histogram because it considers the neighborhood around the threshold point in addition to the threshold point. The optimal threshold is chosen by maximizing the between-class variance function [17] as in equation (3).

$$\sigma_B^2(t) = p_w(t)(\mu_w(t) - \mu)^2 + p_n(t)(\mu_n(t) - \mu)^2 = p_w p_n (\mu_w(t) - \mu_n(t))^2, \tag{1}$$

$$\bar{p}(t) = p(t - m) + \cdots p(t - 1) + p(t) + p(t + 1) + \cdots p(t + m), \text{ and} \tag{2}$$

$$t^* = \text{Arg max } \left(1 - \bar{p}(t)\right) \sigma_B^2(t), \tag{3}$$

where $\sigma_B^2(t)$ is the between-class variance at threshold value t,

μ is the mean value of all the intervals,

$\mu_w(t)$ is the mean value of the water portion at threshold value t,

$\mu_n(t)$ is the mean value of the non-water portion at threshold value t,

$p_w(t)$ is the probability of the water portion at threshold value t,

$p_n(t)$ is the probability of the non-water portion at threshold value t,

m is the number of neighborhood intervals for threshold value t,

p(t) is the probability of the interval at threshold value t,

$\bar{p}(t)$ is the sum of the probabilities of the neighborhood interval around threshold value t,

Arg max is the argument of the maxima for threshold value t in the function, and

t^* is the optimum threshold value.

From the previous study [17] and our empirical test for all the images using three thresholding methods (OT, VE, and NE), the NE method yielded the most suitable result for water extraction from the
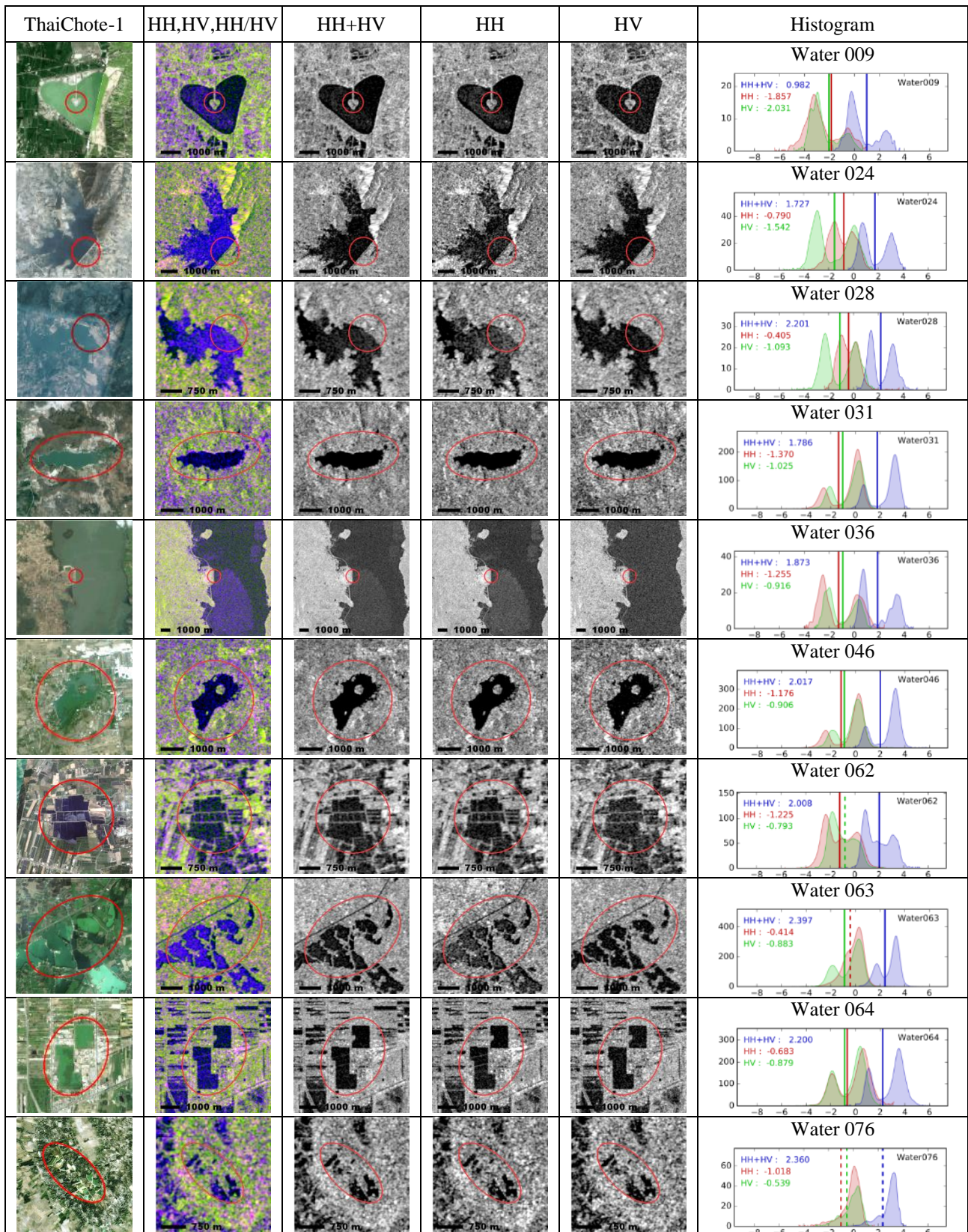
Figure 3-4. Automated threshold values using the neighborhood valley method of water references in the red elliptical areas (10 of 87) from the HH, HV and HH + HV sigma-naught values taken on 2011/11/28 PM (1 of 30 in **Table 3-2**). The dashed lines represent unimodal distributions, and the solid lines represent bimodal distributions. The ThaiChote-1 images in the first column were acquired on different dates in the dry season.

Table 3-2. List of RADARSAT-2 images and threshold values for water extraction.

No.	Local Time	Interval (days)	Path	Beam	Water References		Bimodal Occurrences		Weighted-Average Threshold (dB)	
					Count	Area (Km2)	HH	HH + HV	HH	HH + HV
1	2011/09/02 AM	-	DES	W1	36	101.02	17/36	31/36	-1.25	2.02
2	2011/09/09 AM	7.0	DES	W1	62	180.29	45/62	60/62	-1.20	2.19
3	2011/09/16 AM	7.0	DES	W1	33	116.00	32/33	32/33	-1.37	1.74
4	2011/09/23 AM	7.0	DES	W2	41	118.50	40/41	40/41	-13.96	-12.87
5	2011/09/26 AM	3.0	DES	W1	34	98.25	16/34	31/34	-1.01	2.06
6	2011/09/27 PM	1.5	ASC	W3	53	145.92	53/53	53/53	-0.84	2.21
7	2011/10/03 AM	5.5	DES	W1	61	179.86	49/61	60/61	-0.98	2.26
8	2011/10/04 PM	1.5	ASC	W3	38	115.81	37/38	37/38	-1.06	2.01
9	2011/10/10 AM	5.5	DES	SCNA	83	240.50	74/83	78/83	-1.27	1.92
10	2011/10/11 PM	1.5	ASC	SCNA	87	248.09	77/87	83/87	-1.03	2.04
11	2011/10/17 AM	5.5	DES	SCNB	84	229.70	76/84	79/84	-1.07	2.00
12	2011/10/20 AM	3.0	DES	SCNA	36	101.02	21/36	31/36	-0.30	2.50
13	2011/10/21 PM	1.5	ASC	SCNB	70	183.31	65/70	69/70	-0.92	2.08
14	2011/10/25 PM	4.0	ASC	SCNA	25	73.79	13/25	22/25	-1.04	2.18
15	2011/10/27 AM	1.5	DES	SCNA	74	209.61	54/74	70/74	-1.05	2.07
16	2011/10/28 PM	1.5	ASC	SCNB	87	248.09	78/87	82/87	-0.93	2.14
17	2011/11/04 PM	7.0	ASC	SCNA	87	248.09	80/87	80/87	-1.17	1.94
18	2011/11/10 AM	5.5	DES	SCNB	84	229.70	77/84	80/84	-0.90	2.10
19	2011/11/11 PM	1.5	ASC	SCNA	75	200.62	56/75	68/75	-1.04	2.04
20	2011/11/12 PM	1.0	ASC	SCNA	61	191.21	52/61	57/61	-15.65	-14.51
21	2011/11/14 PM	2.0	ASC	SCNB	69	181.22	64/69	66/69	-1.16	1.88
22	2011/11/18 PM	4.0	ASC	SCNA	24	72.65	13/24	21/24	-1.39	1.89
23	2011/11/20 AM	1.5	DES	SCNA	74	209.61	46/74	62/74	-1.24	2.07
24	2011/11/21 PM	1.5	ASC	SCNB	86	244.22	78/86	80/86	-1.01	2.08
25	2011/11/27 AM	5.5	DES	SCNA	83	240.50	68/83	76/83	-1.46	1.76
26	2011/11/28 PM	1.5	ASC	SCNA	87	248.09	75/87	81/87	-1.24	1.92
27	2011/12/04 AM	5.5	DES	SCNB	84	229.70	75/84	81/84	-1.21	1.91
28	2011/12/21 AM	17.0	DES	SCNA	83	240.50	68/83	74/83	-1.51	1.68
29	2011/12/28 AM	7.0	DES	SCNB	84	229.70	71/84	77/84	-1.30	1.82
30	2012/02/14 AM	48.0	DES	SCNB	68	199.03	56/68	61/68	-16.51	-15.26
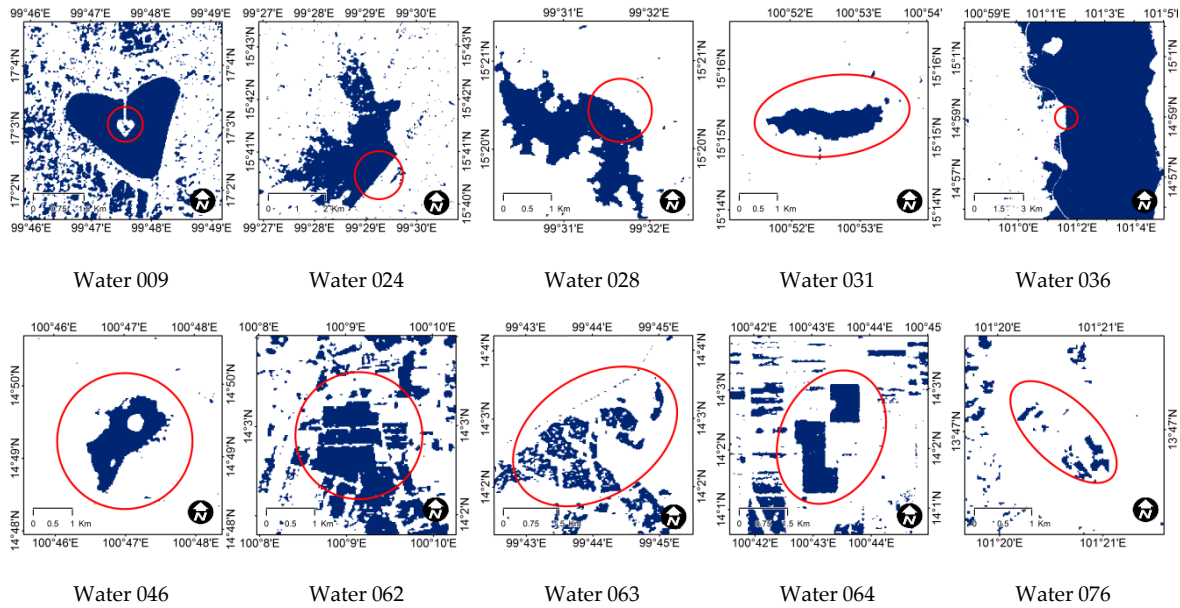
Figure 3-5. Close-ups of the extracted water extents from the RADARSAT-2 image acquired on 28 November 2011 using the HH+HV global threshold value (1.92 dB). The water areas are displayed in deep blue, and the red ellipses are the water references.

RS2 images. The threshold value of that method was close to the valley of the histogram and was able to extract water surfaces quite well. Consequently, the NE method was used for automatic thresholding in the following discussion.

All the histograms were calculated by dividing the entire range of values into 256 intervals and then setting the number of neighborhood intervals to 11 (m = 5). The results of the threshold values are displayed as vertical lines in the histogram plots in **Figure 3-4**. In the figure, the solid lines represent bimodal distributions, whereas the dashed lines represent unimodal distributions, which were excluded from the calculation of the global threshold. For example, water reference 076 was rejected when calculating the global threshold for HH+HV. The threshold values obtained from the bimodal distributions are the area-weighted average, resulting in the global threshold value. This threshold is expected to be effective for the entire image. All the global threshold values are listed in columns 10 and 11 of **Table 3-2**.

Among the 30 RS2 images, the global threshold values were slightly different. This may be because the RS2 images were acquired under different conditions. Different paths result in different azimuth angles, whereas different beam modes result in different incident angles, wave frequencies, and image resolutions. Those conditions produce different backscattering coefficients. The proposed technique has less bias for selecting the threshold value because it does not depend on the satellite mode and seasonal environment. Thus, the extracted water bodies for all the acquisition dates can be combined.
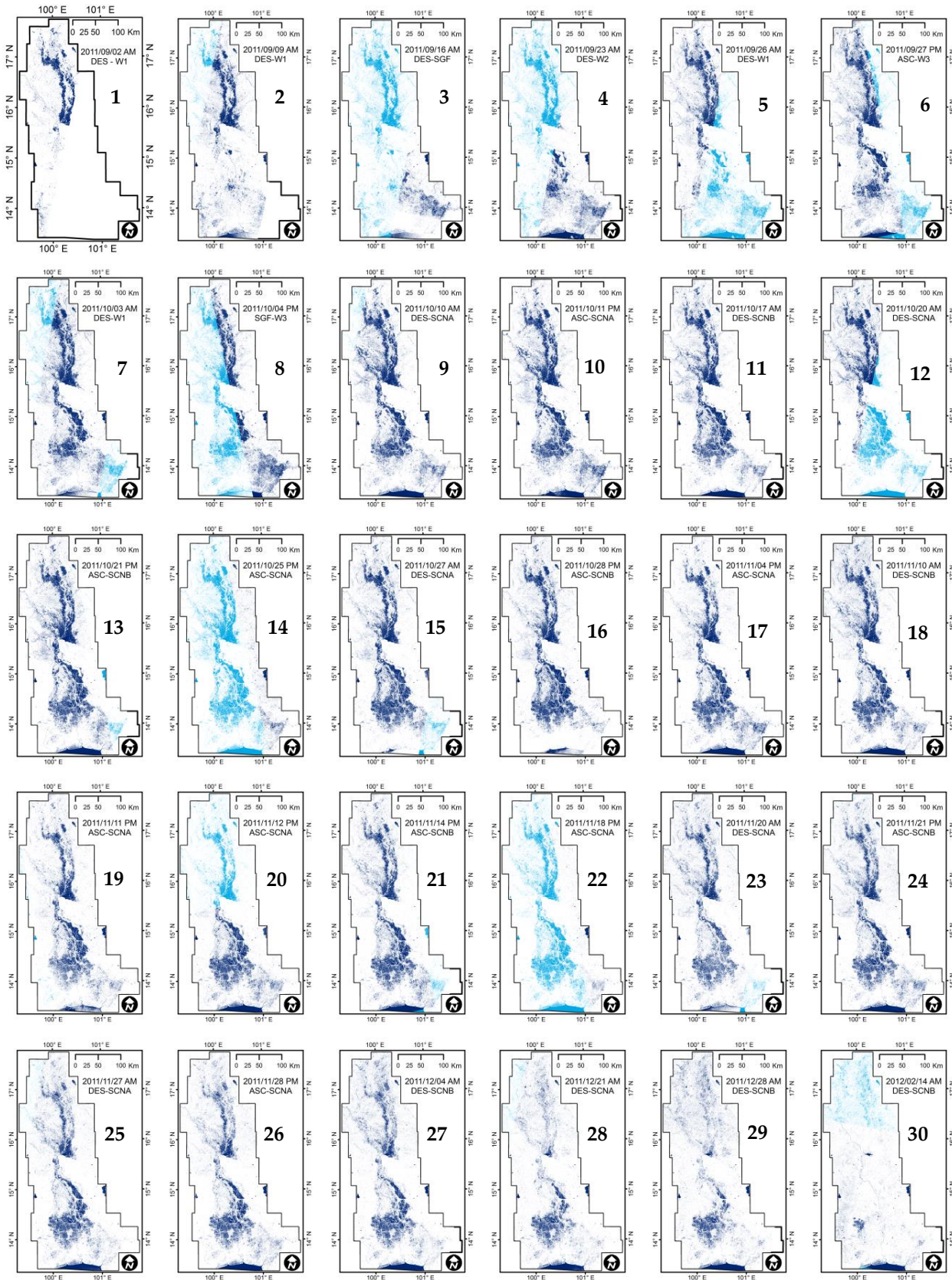
Figure 3-6. Extracted water areas after applying the global threshold value for each Radarsat-2 image. The extracted results from the actual date are shown in deep blue, and the results from the previous date are shown in light blue.

RID Gaging Station ① Ayutthaya Historical Park ② Rojana Industrial Estate ③ Hi-Tech Industrial Estate
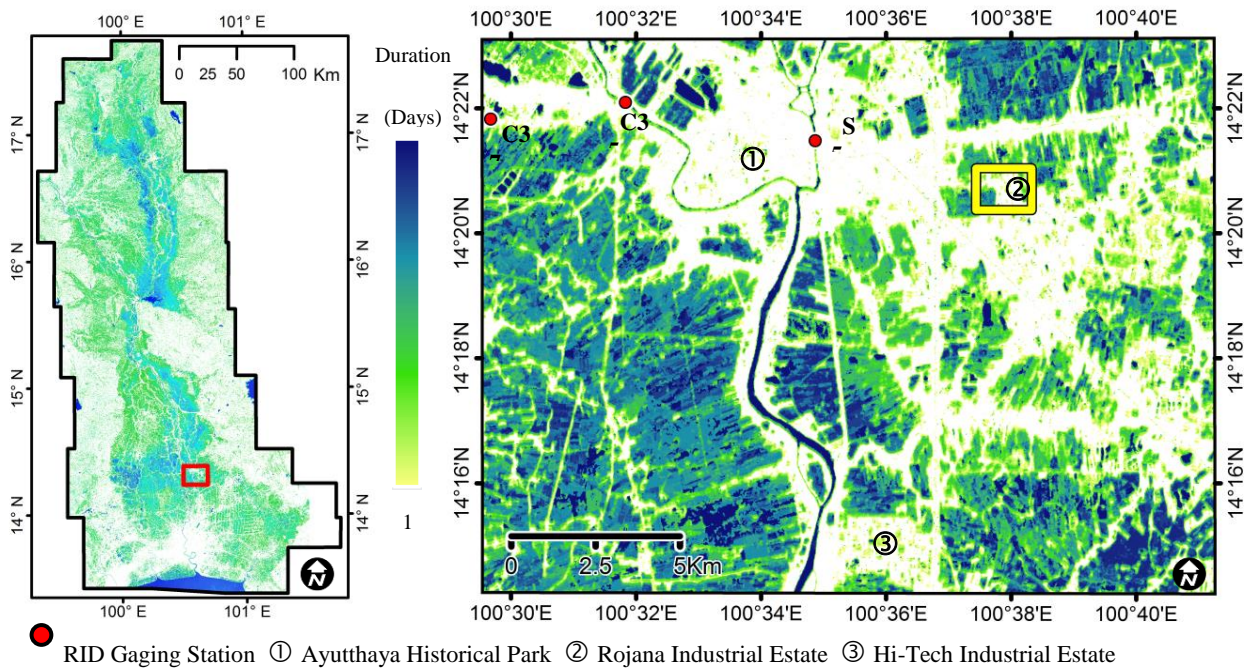
Figure 3-7. Water duration map calculated by stacking the extracted water surfaces. The red border shows Ayutthaya City, an enlargement of which is shown on the right side of the figure. The yellow border shows the Rojana industrial park.

3.3.3. Water Areas Extraction and Flood Duration Map

The water areas were simply extracted by applying a global threshold value to each RS2 image. Close-ups of the extracted result from the image acquired on 28 November 2011 are shown in **Figure 3-5**. The water boundaries obtained using this technique appear to be reasonable in comparison to the visually classified results from the original RS2 and TH1 images acquired in a dry season. All the RS2 images from the 30 dates were processed separately. Because some RS2 images did not cover the entire study area, the missing parts were estimated from the previous image. The results are shown in **Figure 3-6**. The results from the current date are shown in deep blue, and the estimated results from the previous date are shown in light blue. The estimations coincided with the actual flood situation; flooding began in the north region on 2 October 2011 (image 1), the flooded areas spread to the south on 23 October 2011 (image 4), the flood in the north had abated by 21 November 2011 (image 28), and was completely finished on 14 February 2012 (image 30).

Flooding usually occurs over a long duration because the central region of Thailand is nearly flat. Agricultural plants have limited times to tolerate waterlogging or submerging. Buildings and electrical equipment are not designed to work in this situation and are hard to repair. The severity of damage to assets increases with flood duration. Therefore, the period of inundation or a flood duration map is very important

to the Thai government for controlling floods and developing remedial plans. The flood duration map was produced by stacking the interval of the extracted water surfaces. The final flood duration map is shown in **Figure 3-7**.

3.4. Accuracy Assessment

The accuracy of a classification must be assessed by comparing the results with truth data. In this study, optical images that captured ground surface activity and gaging stations that recorded water heights were introduced as truth data sources. During this flood event, almost all the country was covered by clouds, and optical satellite clear-sky images therefore were very rare. GeoEye-1 (GE1) and ThaiChote-1 (TH1) clear-sky images taken on 22 November 2011 over Ayutthaya city were selected as the truth data. Those data covered the Ayutthaya Historical Park and the Rojana and Hi-Tech industrial parks, which are very important economically and for tourism.

To extract the flooded areas from the optical images, using the Normalize Different Water Index (NDWI) calculated from the Green (G) and near-infrared (NIR) band values is the most popular and effective method [36]. McFeeters proposed the NDWI in 1996 to detect surface waters in wetland environments and to allow for the measurement of surface water extent, and asserted that values of NDWI greater than zero are assumed to represent water surfaces, while values less than, or equal to, zero are assumed to be non-water surfaces [37]. In this image interpretation, rivers and ponds were also extracted as flooded areas because nearly the entire study area was covered by water. The GE1 NDWI threshold for the water areas during the flood period was determined by visual interpretation of **Figure 8(4B)** as NDWI $\geqq$ 0.02 or 69.1% of the image area shown in **Figure 3-9(1A‑1C)**. This NDWI threshold value was used as the truth data when obtaining the most accurate threshold values for NDWI from TH1 and HH + HV from RS2.

3.4.1. Finding the Best Accuracy Thresholds for the ThaiChote-1 and RADARSAT-2 Images

The comparison of two (the truth data and estimation) two-class spatial images, water areas (W) or non-water areas (N) results in four combinations: W-W, N-N, W-N, and N-W. When the threshold for a client's image is set to the minimum value, all of the results will be non-water areas (N). Some of them are N-N, which represents the same N values as those from the master image (GE1), whereas the others are W-N, which represents a water extraction omission error (false negative). When the threshold of the client image moves to higher values, some values will be considered to be water (W). Some of these values are W-W, which represent the same W values, whereas the others are N-W, which represent overestimation (commission error, false positive) in the water extraction. The best threshold value is the point where the summation of the W-W and N-N areas becomes largest. This point corresponds to the result most similar to that from the GE1 image. The results of this approach are shown in **Table 3-3**.

Similar to GE1, TH1 has an optical sensor with four bands with quite similar spectral ranges, but its spatial resolution is much lower. Before calculating the NDWI values, a TH1 image in **Figure 3-8(5A)** was up-sampled and co-registered to the GE1 image. We then compared the NDWI in **Figure 3-8(5B)** with that from the GE1 image. The most accurate TH1 NDWI threshold for water was found to be 0.28, which corresponds to 64.6% of the estimated water areas (W-W and N-W) in **Figure 3-9(2A–2C)**. Among those extracted areas, 85.2% were similar to those from the GE1 (W-W and N-N), 9.6% were false negatives (W-N), and 5.1% were false positives (N-W). By applying this NDWI threshold to the TH1 pre-flood image, the water-covered ratio of this area was 11.9%.

For thresholding SAR sensors, the backscattering coefficient (the sigma naught value, $\sigma°$) is used more often than the NDWI for optical sensors. The best threshold for the RS2 HH+HV acquired on November 21, 2011 was determined to be 3.18 dB, which corresponds to 64.9% of the estimated water areas (W-W and N-W). Among those extracted water areas, 79.9% were similar to the results from GE1 (W-W and N-N), 12.2% were false negatives (W-N), and 7.9% were false positives (N-W).

3.4.2. Comparison with the Proposed Method

The threshold value for RS2 from the most accurate thresholding method was greater, covered a larger area and was more accurate than the proposed weight averaged neighborhood valley-emphasis thresholding method. The RS2 threshold value acquired for 21 November 2011, (image 24) from the most accurate thresholding method was 3.18 dB (64.9% area coverage), whereas that by the proposed method was 2.08 dB (44.0% area coverage). For the proposed method, 71.9% of the results were similar to the results of GE1 (W-W and N-N), 26.6% were false negatives (W-N), and 1.5% were false positives (N-W). From **Figure 3-9(3B,3C)**, the blue color shows the water areas extracted by the proposed method, and the green color shows the difference from the best accuracy method.

Although the threshold value of the best accuracy method is apparently more eligible, applying that local threshold value to the entire study area returned an inappropriate result and was difficult to implement as a practical procedure. The extraction of water surfaces using that threshold value for the entire area resulted in overestimation. For example, the water areas in **Figures 3-5** and **3-6** became noisier. Moreover, it was almost impossible to find suitable optical images to be used as references for the SAR images throughout the event.

3.4.3. Comparison with the Gaging Station Data

Because the satellite images were not taken from the same sensors and were not acquired on the same date, it is difficult to explain the cause of the different extracted water extents. The difference in sensor types and spatial resolutions and changes in water height over time may have contributed to the discrepancy. The heights of the flood waters were difficult to project because water flows downward without stopping,

although water flows rather slowly in this area. To understand the flood event, the daily average water heights above the mean sea level (MSL) that were collected from the three nearest telemetry gaging stations (C35, C37, and S5) and recorded by the Royal Irrigation Department (RID) [38] and the water depths from the surface of the road at four checkpoints reported by Rojana Industrial Park Public Co., Ltd. [39] were introduced as truth data, as shown in **Figure 3-10**. The four water checkpoints were located in the Rojana Industrial Park at the power plant (RJ0), Rojana phase-1 gate-A in front of the head office (RJ1), Rojana phase-2 gate-B (RJ2), and Rojana-3 around the flyover (RJ3). Among them, RJ0 was closest to the Honda automobile factory shown in **Figure 3-9**.

The solid lines in the left graph show the water heights at the three telemetry gaging stations over a one-year period (April 2011 to March 2012). The period over which the satellite images were acquired was at the end of the flood event, when the water level had dramatically decreased. Although the water heights were slightly different on 22 November 2011, they had significantly dropped more than 30 cm in three days by 25 November 2011.

Because the satellite images were not taken from the same sensors and were not acquired on the same date, it is difficult to explain the cause of the different extracted water extents. The difference in sensor types and spatial resolutions and changes in water height over time may have contributed to the discrepancy. The heights of the flood waters were difficult to project because water flows downward without stopping, although water flows rather slowly in this area. To understand the flood event, the daily average water height above the mean sea level (MSL) that were collected from the 3 nearest telemetry gaging stations (C35, C37 and S5) and recorded by the Royal Irrigation Department (RID) [38] as shown in **Figure 3-10**. The water depths from the surface of the road at 4 checkpoints reported by Rojana Industrial Park Public Co., Ltd. [39] were also introduced as truth data. The 4 water checkpoints were located in the Rojana Industrial Park at the power plant (RJ0), Rojana phase-1 gate-A in front of the head office (RJ1), Rojana phase-2 gate-B (RJ2), and Rojana-3 around the flyover (RJ3). Among them, RJ0 was closest to the Honda Automobile factory shown in **Figure 3-9**. The pictures of water checkpoints RJ0 and RJ1 taken on November 13 and 23, 2011 illustrated flood situation are shown in **Figure 3-11** and **Figure 3-12**. Water level statistics chart of gaging station and water check points are shown in **Figure 3-13**.

3.5. Discussion and Future Work

The proposed method can improve the speed of automated thresholding because to determine the global threshold value from static local areas is much more efficient than to do from systematic hierarchical local areas. This technique is suitable for multi-temporal images in a specific place, like the Chao Phraya river basin. Although the processing for permanent water references is rapid, the selection of proper water references takes time at the first step. An improper water reference without a bimodal distribution histogram should not be considered because it does not contribute to the estimation of the global thresholding.

RADARSAT-2

GEOEYE-1　　　　**THAICHOTE-1**
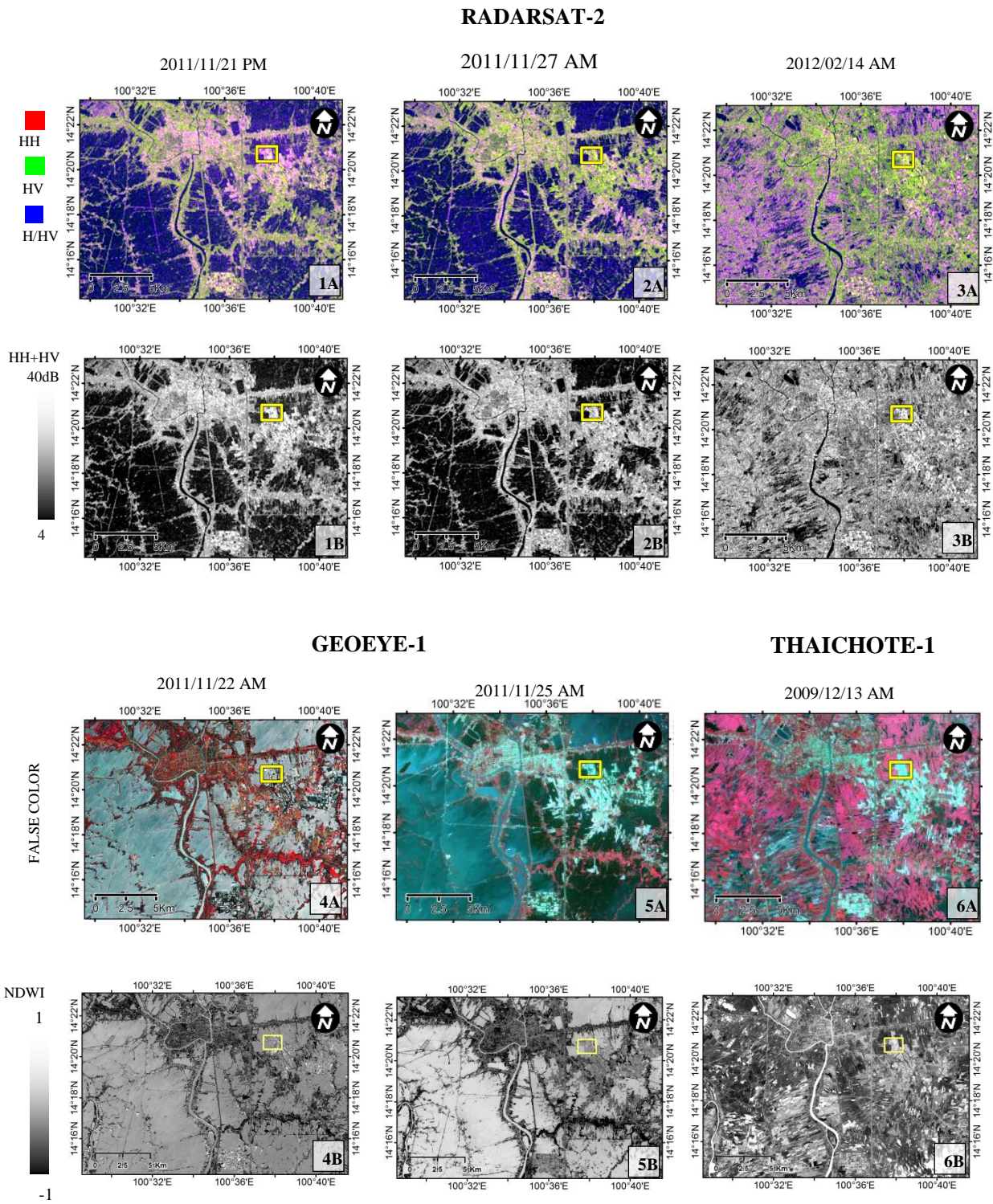
Figure 3-8. Close-up of Ayutthaya city for in-flood and post-flood time. The dual polarization color composite (1A–3A) and HH + HV (1B–3B) from RADARSAT-2. The false color composite and NDWI (4A, 4B) from GeoEye-1, and the false color composite and NDWI for in-flood (5A, 5B) and pre-flood (6A, 6B) times from ThaiChote-1.
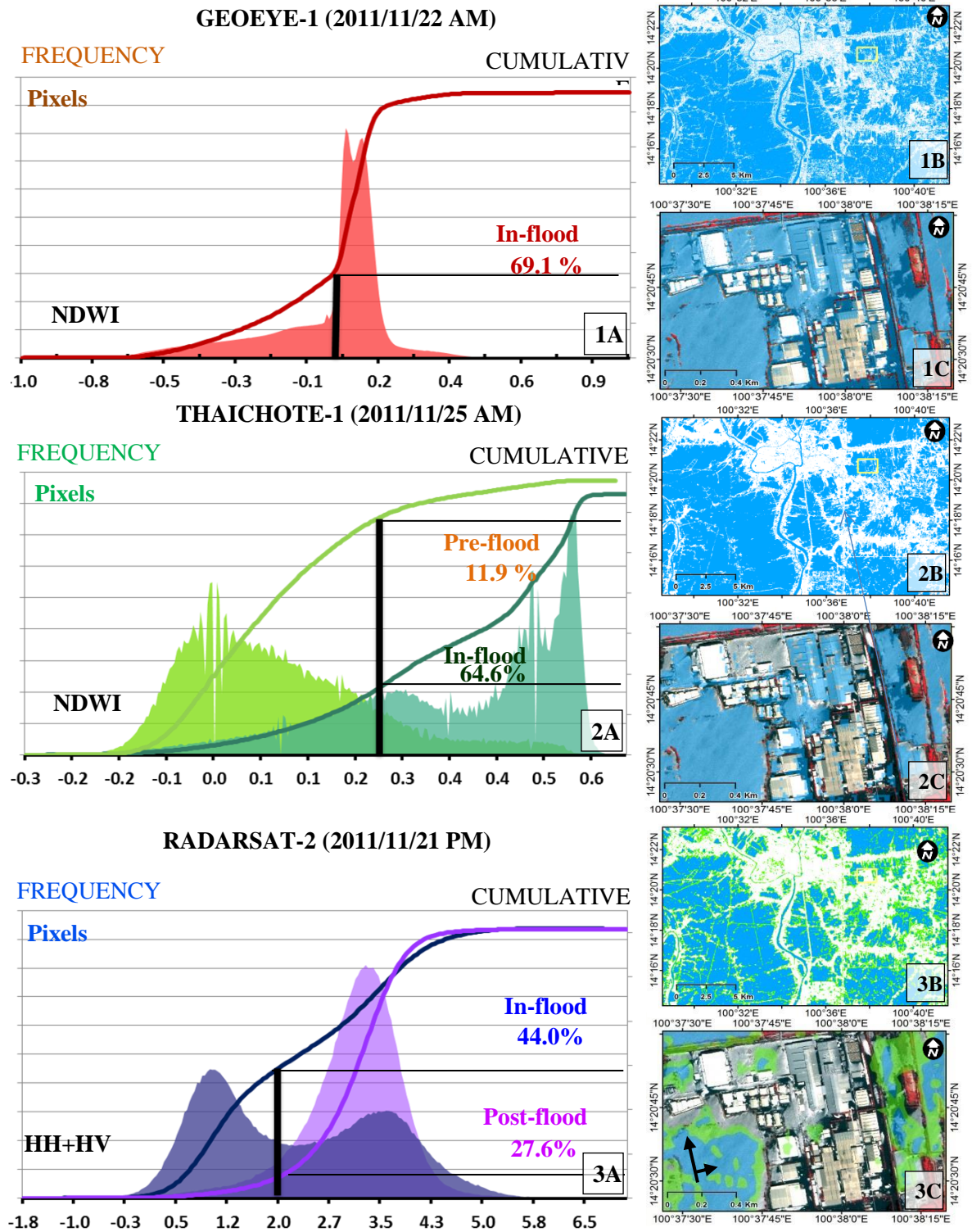
Figure 3-9. Histograms and cumulative probability plots (top) and extracted flooded areas (blue color) in Ayutthaya city (middle) and over part of the Rojana Industrial Park (bottom), from the visualization of the GeoEye-1 image (1A–1C), determining the best accuracy of the ThaiChote-1 image (2A–2C), and the emphasis of the neighborhood valley on the RADARSAT-2 image (3A–3C), plotted on a GeoEye-1 false color composite. The green pixels are the determined best accuracy results from RADARSAT-2, which was larger than that determined using the neighborhood valley-emphasis method.
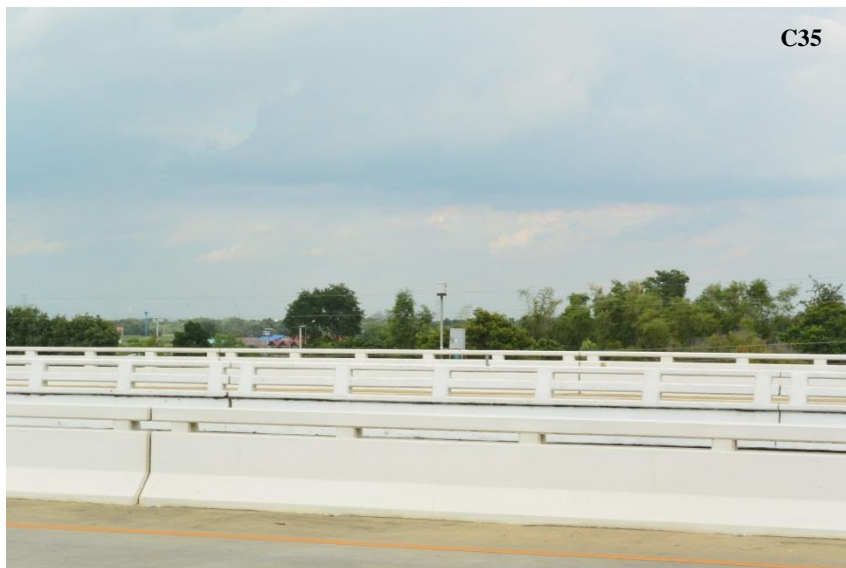
Figure 3-10. Telemetry gaging station pictures at C35, C37, and S5 taken during a field survey on October 5, 2014.

Figure 3-11. Water levels at water checkpoint in front of the power plant (RJ0) of Rojana Industrial Park, taken on November 13 and November 23, 2011

Source: http://rojna-th.listedcompany.com/flood_situation.html

Figure 3-12. Water levels at water checkpoint in front of the head office (RJ1) of Rojana Industrial Park, taken on November 13 and November 23, 2011

Source: http://rojna-th.listedcompany.com/flood_situation.html

Table 3-3. Results of the accuracy assessment of the water extraction for Ayutthaya city.

Satellite/Date	Data	Method	Threshold Value	N-N (%)	W-N (%)	N-W (%)	W-W (%)	Water (N-W + W-W) (%)	Accuracy (N-N + W-W) (%)
GE1 2011/11/22 AM	NDWI	VS[1]	0.02	-	-	-	-	69.1	-
TH1 2011/11/25 AM	NDWI	BA[2]	0.28	25.8	9.6	5.1	59.5	64.6	85.2
RS2 2011/11/21 PM	HH+HV	BA[2]	3.18 dB	23.0	12.2	7.9	56.9	64.9	79.9
		NE[3]	2.08 dB	29.4	26.6	1.5	42.4	44.0	71.9

(1) VS = visualization thresholding

(2) BA = find best accuracy thresholding

(3) NE = weight-average neighborhood valley-emphasis thresholding
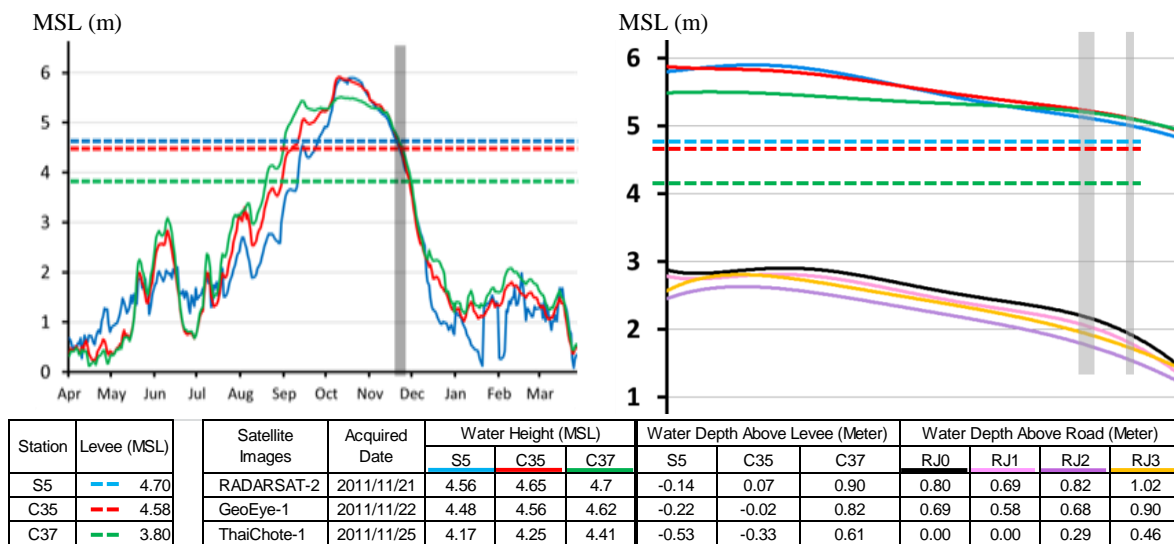
Figure 3-13. Comparison of the water heights recorded at three telemetry gaging stations and the levee heights (**left**); enlargement of the left plot for 14–27 October and the water depths above the road surface observed at four checkpoints in the Rojana Industrial Park (**right**).

Open water from SAR images can be extracted quite well, but it is difficult to extract water in inundated urban areas and under trees [25,27, and 40]. The most important factor that limits the use of satellite data are resolution. When a satellite records data in a high-resolution mode, the imaging swath becomes smaller than that in the normal mode. This fact is caused by limitations of the data recorder and transmitter. Observing an inundation over a wide area with the same sensor or the same satellite is almost impossible. Although RS2 can observe in the spotlight mode at a 1-m resolution, the image on November 22 was acquired in the SCNB mode at a 25-m resolution to cover a larger area. On the other hand, the resolutions of pan-sharpened GE1 and TH1 images are 1 m and 2 m, respectively. Therefore, the GE1 and

RS2 results are quite different (approximately 23–33%), according to the accuracy assessment. For detecting the water surface, a large number of pixels were missing because the overall backscattering of the pixels surrounded by obstacles such as buildings was higher than for open spaces.

Sensor type can also cause differences. Although the NDWI obtained from optical sensors is suitable for the detection of water surfaces, objects having low infrared radiation are also classified as water surfaces. This misclassification can be observed in **Figure 3-9(1C)** and **(2C)**. The roof-tops of buildings were sometimes identified as flood water by GE1, and there were more false-positive classifications from TH1. Water surfaces may also be misclassified by the backscattering coefficient from a SAR sensor. For example, non-water objects with smooth surfaces such as roads and runways are classified as water surfaces. Furthermore, side-looking transmission hinders observational ability. Water surfaces next to buildings produce double bounce backscattering, resulting in a total backscattering coefficient that is higher than usual and misclassifications as non-water. This effect can be observed in **Figure 3-9(3C)**, where the west sides of the buildings were misclassified because the layover was projected onto the water surface. Similarly, the water surfaces between the buildings were misclassified.

Observing inundations using satellites has another drawback; water under roofs or inside buildings cannot be observed. Auxiliary data must be prepared to provide the missing information. The average ground elevation data were prepared from an aerial survey conducted by the Japan International Cooperation Agency (JICA) for the zone along the Chao Phraya River and by ESRI Thailand for the outer area in 2012. The combined data can cover the entire Chao Phraya river basin. Future research needs to focus on improving accuracy through the utilization of LiDAR DEMs as topographic data.

3.6. Conclusions

Multi-temporal RADARSAT-2 images with different acquisition conditions were used to extract water areas from the 2011 central Thailand flood along the Chao Phraya river. Considering the use of satellite SAR data in emergency situations, where validation data are scarce and optical images are hindered by cloud cover, an automated thresholding approach for water extraction was attempted. By introducing the global threshold value of the entire study area for each SAR image, the weight-averaged neighborhood valley-emphasis method was able to extract flooded areas automatically from the backscattering coefficient. The proposed method, which obtains the threshold value from the water references located throughout the Chao Phraya river basin, is more suitable for Thailand. Moreover, this technique is independent of the satellite acquisition condition, and there is no need to normalize the images before combining all the extracted water-areas as a flood duration map. In this case, the HH+HV dual-polarization achieved a higher accuracy than the HH single-polarization for open water extraction, which is affected by winds and floating/submerged plants. The extraction result for Ayutthaya city was similar to the visual inspection result from a GeoEye-1 image (approximately 67%), whereas the result obtained by the best accuracy thresholding

method was approximately 77%. The results based on the ThaiChote-1 image were more similar to that from the GeoEye-1 image (approximately 82%) because they were both obtained by high-resolution optical satellites. On the other hand, the results from RADARSAT-2 had lower accuracies than those from GeoEye-1 and ThaiChote-1 because of its lower spatial-resolution and side-looking observational scheme. SAR images also have limitations for observing water areas covered by trees or adjacent to buildings. Despite these obstacles, the extraction of flooded areas from SAR intensity data can be improved by introducing pre-event topographic data such as LiDAR DEMs and building footprints.

Chapter 4

Implementation of Automated Inundated Areas Extraction System for the Central Thailand Flood from Multi-Temporal, Dual-Polarization RADARSAT-2 Image: A Case Study of Flood in 2016

4.1. Introduction

The Thai government assigned Chao Phraya river basin as a frequently inundated area. According to the flood historical data provided by the Geo-Informatics and Space Technology Development Agency (GISTDA) [1], a flood occurs in this area almost every year as shown in **Figure A-4**. These data obtained by applying a manual threshold value to HH intensity of RADARSAT-1, RADARASAT-2 and COSMO-SkyMed satellites acquired throughout the rainy season from the year 2006 to 2015. Flood monitoring should regularly be performed with unbiased technique. Thus, this study intends to monitor flood situation in this water basin by applying the same technique as chapter 3. The results were validated by Landsat 8 optical images.

The three RADARSAT-2 (RS2) images from several images taken in rainy season 2016 were selected for the processing. Due to the flood situation in the year, 2016 was not heavy as the year 2011, Ayutthaya city was not faced with inundation. In this year, the flood occurred in some part of these provinces, Sukhothai (STI), Phitsanulok (PLK), Nakhon Sawan (NSN), Supha Buri (SPB) and Phra Nakhon Si Ayutthaya (AYA). Thus, the validation area was change to these regions. The optical images were taken by Landsat 8 (LS8).

4.2. Study Area and Imagery Data

This study focuses on the same area as chapter 3, the Chao Phraya river basin in the central part of Thailand. The approximate area is 7400km2.

This section performs automated inundated area extraction of the RS2 imagery data acquiring on 23 October, 11 November, and 5 December 2016. The processing technique mentioned in the previous section was applied to these data. The accuracy assessment has been done by comparing the flood extracted results with Landsat8 images taken on 21 October and 13 November 2016.

The RS2 images used in this study acquired by beam types SCNA (W1 + W2) and SCNB (W2 + S5 + S6). All of them were taken in the HH and HV dual-polarization mode with 25-m resolution. Images taken in October and November were observed from the descending (DES) path, while December was observed from the ascending (ASC) path. Their color composite maps are shown in **Figure 4-1,** and a summary of the images properties is provided in **Table 4-1**. The Landsat8 images were always observed from descending (DES) path due to it is a sun-synchronized orbital satellite. There are eleventh bands with several resolutions are provided. All bands using in this study are 30-m resolution. These images will be shown in the accuracy assessment section.

4.3. Methodology and Results

The RS2 images were preprocessed by using the Sentinel Application Platform (SNAP) software. This process comprised with the radiometric calibration, the Refined Lee speckle filtering, and terrain correction using an SRTM 90-m DEM. Then, the water extraction technique proposed in chapter 3 was applied to the images. This water extraction begins with threshold value calculation, and then applied the threshold value to the backscattering images. This study focuses only on HH + HV since the previous study show that, HH + HV sigma naught as total backscatter can reduce the effect of the wave on the water surface.

The threshold value calculation consists of two steps, local thresholding, and global thresholding. Since the three images should be reprocessed in the same ways as chapter 3, the 28 water references have been declared permanently for the Chao Phraya river basin, were applied to these images to find local threshold value. These elliptical shape water references are located throughout the Chao Phraya river basin. Water reference having unimodal distribution histogram was rejected from the processing before calculate the local threshold. According to the chapter 3, the neighborhood valley-emphasis (NE) method have been proved it is the most suitable for water extraction, just only this method was applied. The global threshold value obtained from weight average by area from all local threshold which having bimodal distribution histogram. The number of bimodal occurrences and the global threshold value for each image was shown in **Table 4-1**. In this table, HH + HV show once again that it can increase bimodal probability rather than use only HH backscattering.

The global threshold value was applied to each HH + HV image to obtain the water area. These extracted water areas results are shown in **Figure 4-2**. These three images reveal flood situation take placed in three regions. First, Sukhothai and Phitsanulok province (STI&PLK) is located in the north part. Second, Nakhon Sawan province (NSN) is located in the middle part. Third, Suphan Buri and Phra Nakhon Si Ayutthaya (SPB&AYA) is located in the lower part.

Illustrating a multi-temporal flood extracted data acquired from several dates is more convenient by repetition as flood detection map in **Figure 4-3**. This map was displayed in seven colors. One time repetition show as yellow shade, the bright tone is 23 October, the mid tone is 11 November, and the dark tone is 5

December 2016. Two times repetition shown as blue shade, the bright tone is 23 October and 11 November, the mid tone is 11 November and 5 December 2016. Three times repetition shown as dark blue. The last one, a gray color, indicates not continuous of two times repetition which is uncertain classifies. The close-ups of the flood detection map for 87 water references are shown in **Figure 4-4**. From these close-ups images, the water body could be detected very well in dark blue which refer to three times repetition of water extracted area.
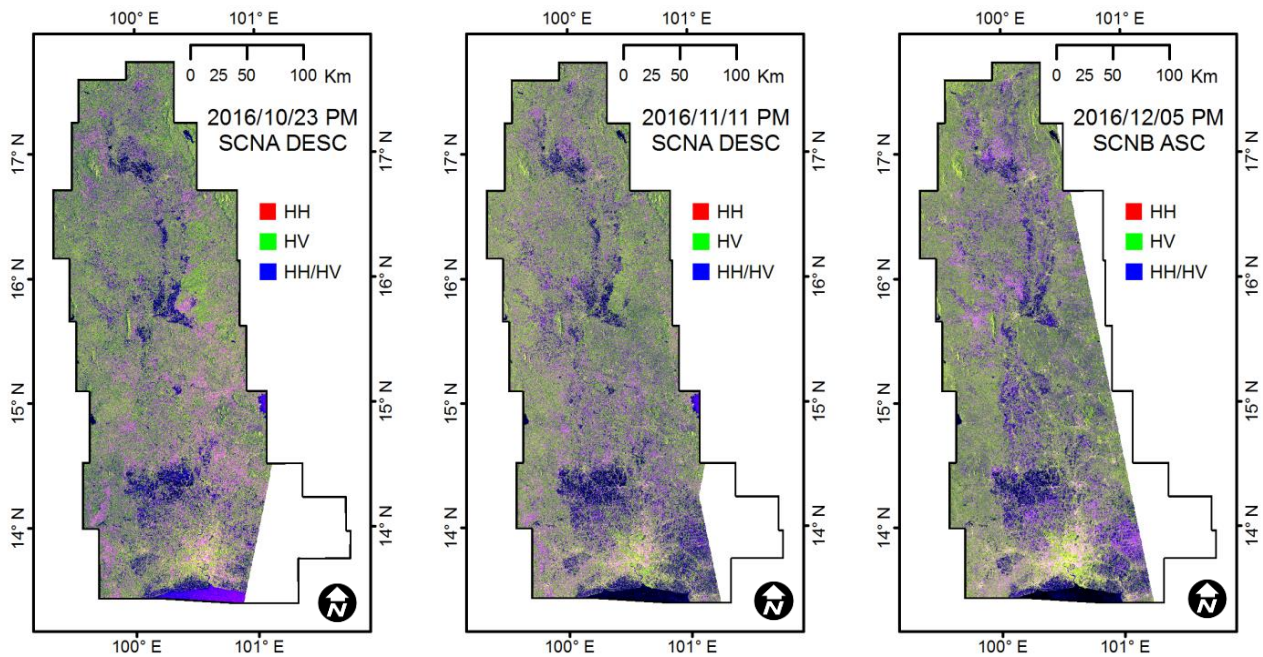
Figure 4-1. The RADARSAT-2 color composite (HH as red, HV as green, and HH/HV as blue) images taken at the beginning, middle, and end of the 2016 Thai flood event.

Table 4-1. List of RADARSAT-2 images and threshold values for water extraction.

No.	Local Time	Interval (days)	Path	Beam	Water References		Bimodal Occurrences		Weighted-Average Threshold (dB)	
					Count	Area (Km2)	HH	HH + HV	HH	HH + HV
1	2016/10/24 AM	-	DES	SCNA	78	8.4	38	44	-13.97	-12.63
2	2016/11/11 PM	18	ASC	SCNB	74	7.7	51	53	-15.51	-14.10
3	2016/12/06 PM	24	ASC	SCNB	71	7.4	39	46	-15.37	-14.06
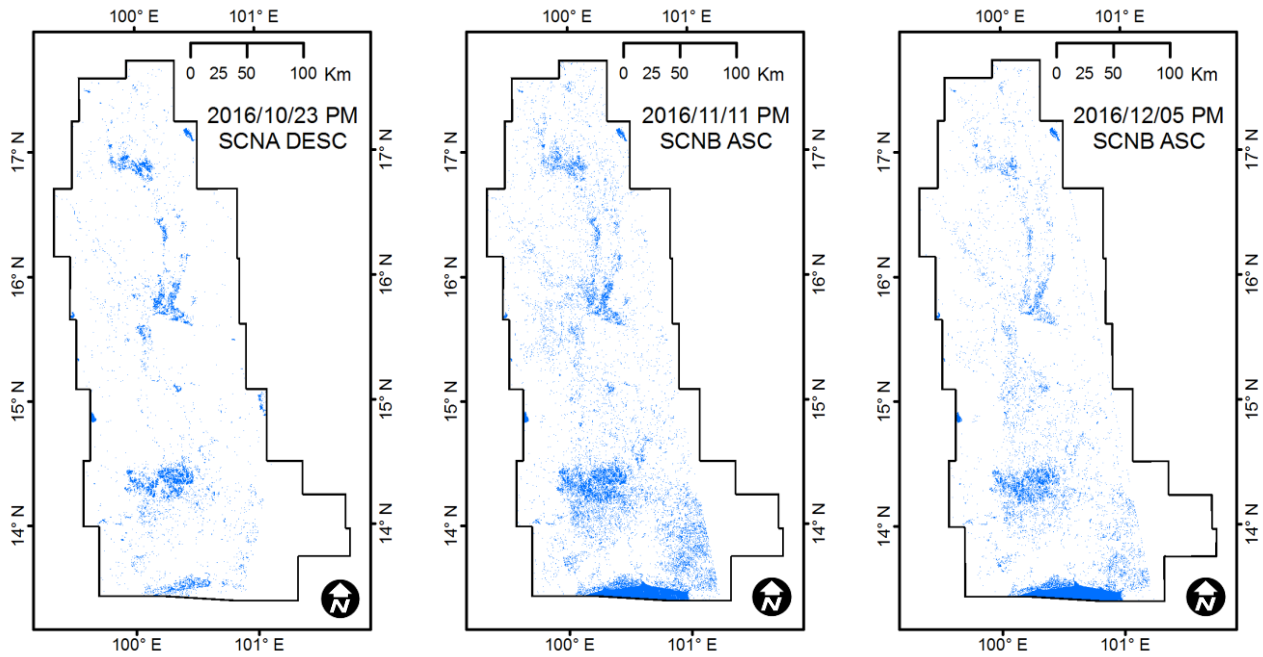
Figure 4-2. Extracted water areas after applying the global threshold value for each Radarsat-2 image. The extracted results show in blue color.
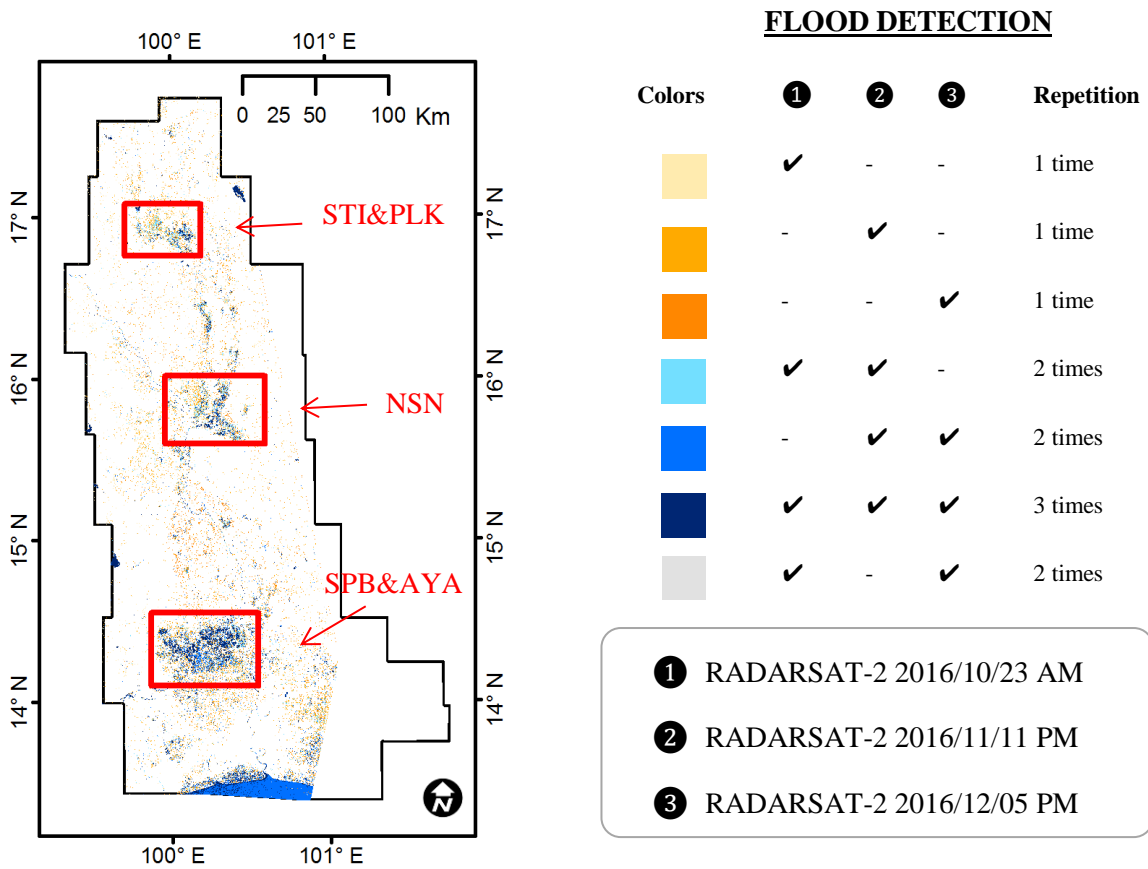
Figure 4-3. The detected flood area from RADARSAT-2 acquired from 3 dates. The color reference was classified by repetition into 7 classes. There was flood occurs in 3 regions.
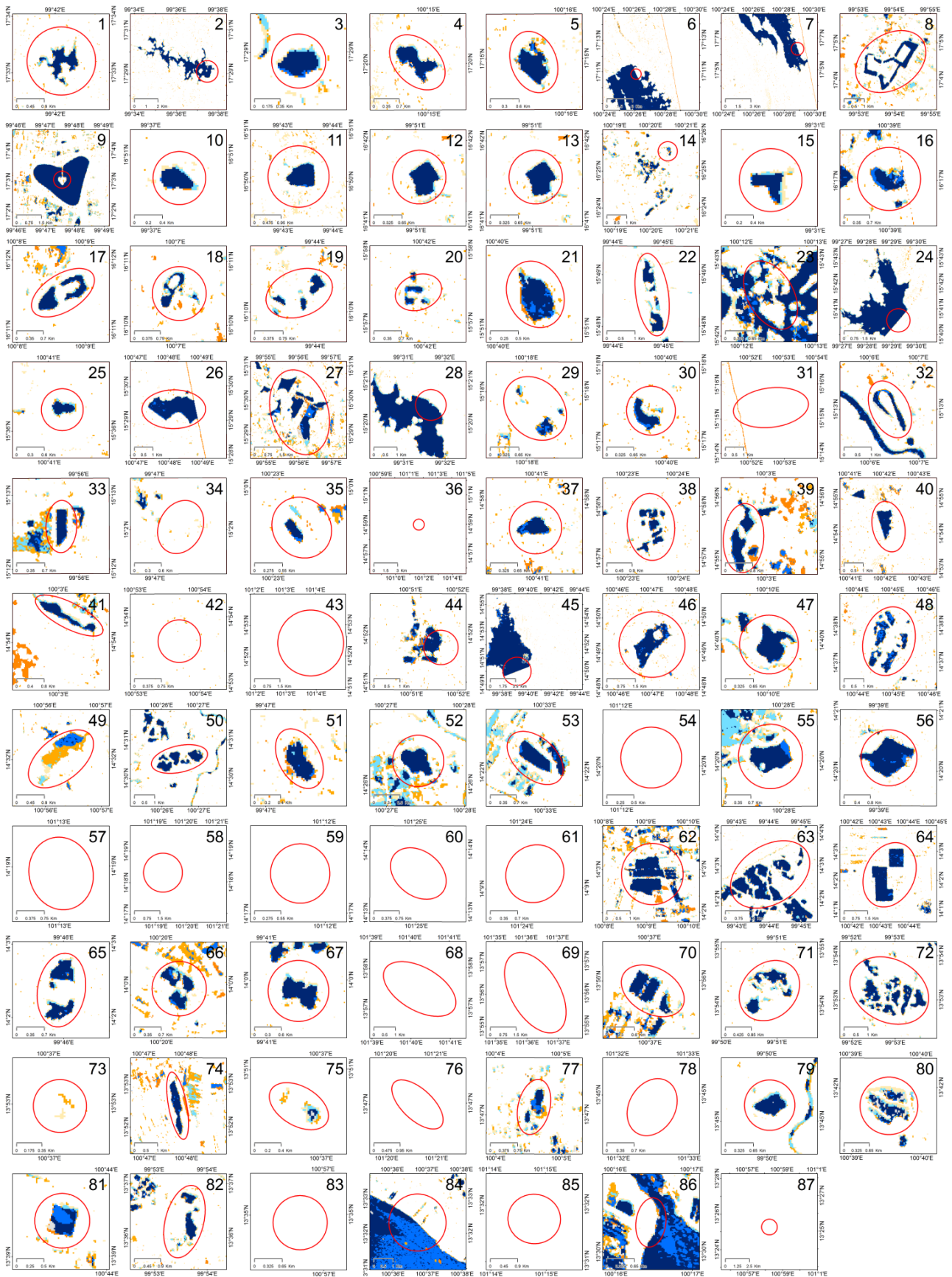
Figure 4-4. Close-ups of the flood detection map from the RADARSAT-2 images for 87 water references. The red ellipses are the water references.

4.4. Accuracy Assessment

Validating the flood extraction from RS images in this study has been done by comparing the results to LS8 images. Although both flood areas were extracted from thresholding technique, they were different sensors. The total backscatter (HH + HV) is the representative of RS2, while Normalized Difference Water Index (NDWI) is representative of LS8.

NDWI is remote sensing derived index related to detecting water on the earth. There are several pairs of spectral band. The first intent was proposed by Bo-Cai Gao, calculated from Near-Infrared (NIR) and Short Wave Infrared (SWIR) [2] as in equation (1):

$$NDWI = \frac{(NIR-SWIR)}{(NIR+SWIR)}. \tag{1}$$

Although this method is suitable for general optical satellite including LS8, some optical satellite has no SWIR sensors. Therefore, the previous section which using GeoEye-1 (GE1) cannot use this index. For GE1, the four sensor satellite, blue, green, red, and NIR must be calculated from green and NIR proposed by S.K. McFeeters [3] as in equation (2):

$$NDWI = \frac{(Green-NIR)}{(Green+NIR)}. \tag{2}$$

Thus, to be able to compare with the previous study in chapter 3, this study evaluated water surface by green and NIR bands. According to the sky usually cover with the cloud in the rainy season, LS8 images were selected by closest acquired date to the RS2 images and least percentage of cloud cover.

The threshold value uses for NDWI to extract water area were determined by finding the best accuracy mentioned in chapter 3. The comparison of water area extracted from RS2 and LS8 results in four combinations: W-W, N-N, W-N, and N-W. The best threshold value for LS8 is the point that summation of the W-W and N-N areas becomes largest. This stage corresponds to the results of LS8 image most similar to that from the RS2 image. The results of this operation and the accuracy for the three regions are shown in **Table 3-2**. The evaluated accuracy values for the three regions were 90.5%, 89.0%, and 93.3% accordingly.

After the best threshold values had been obtained, these values were applied to NDWI images to extracted water area. The results are shown in **Figure 4-5** for the Sukhothai and Phitsanulok province (STI&PLK), **Figure-4-6** for the Nakhon Sawan province (NSN), and **Figure 4-7** for Suphan Buri and Phra Nakhon Si Ayutthaya province (SPB&AYA).
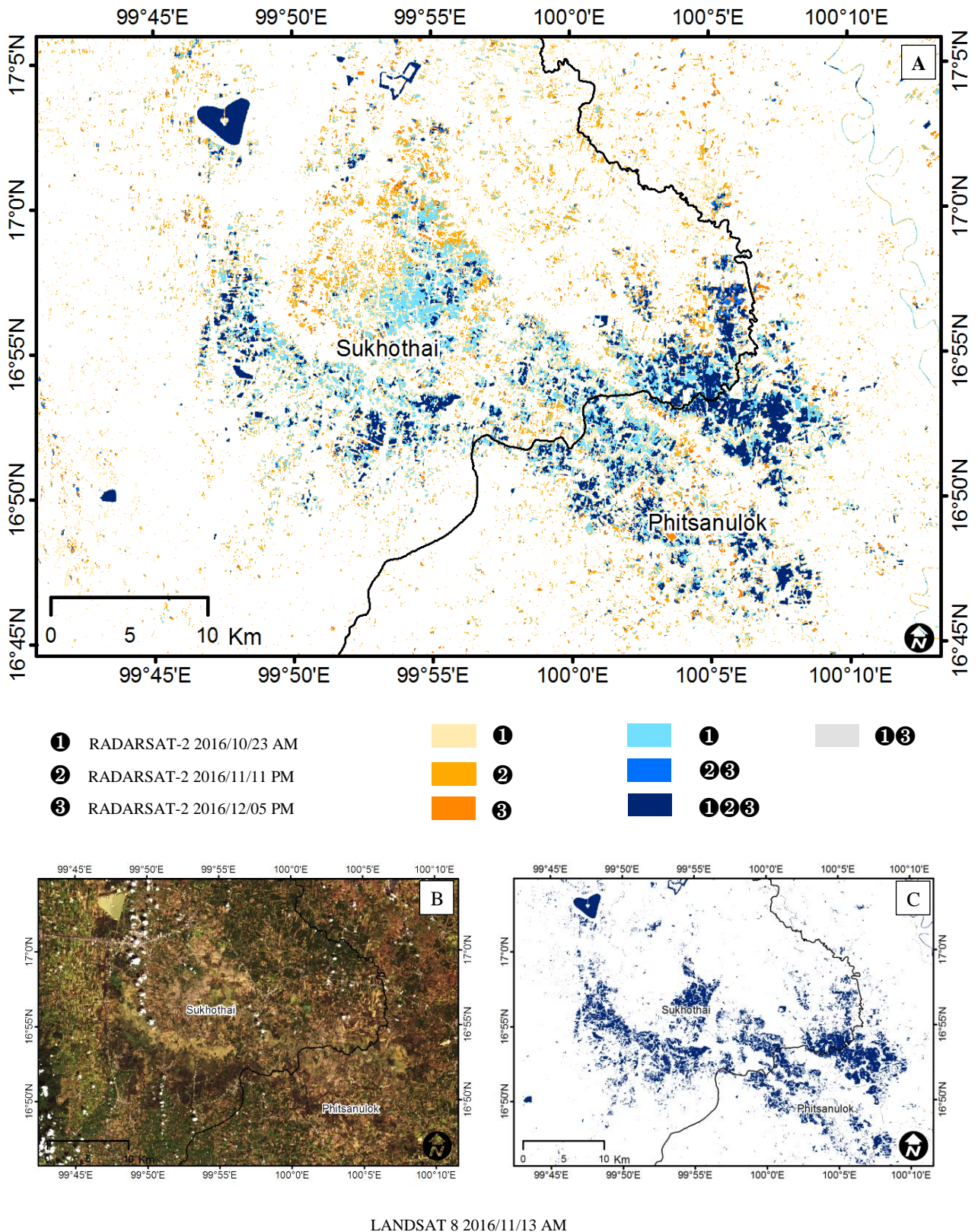
Figure 4-5. A Flood area map from RADARSAT-2 HH+HV automatic thresholding technique for Sukhothai and Phitsanulok province (STI&PLK) (A). The seven combination colors indicate repetition of the flood in three acquiring dates. Landsat8 true color composite map (B), and flood area map from finding the best accuracy of NDWI (C).

❶ RADARSAT-2 2016/10/23 AM
❷ RADARSAT-2 2016/11/11 PM
❸ RADARSAT-2 2016/12/05 PM

❶
❷
❸

❶
❷❸
❶❷❸

❶❸

LANDSAT 8 2016/10/21 AM
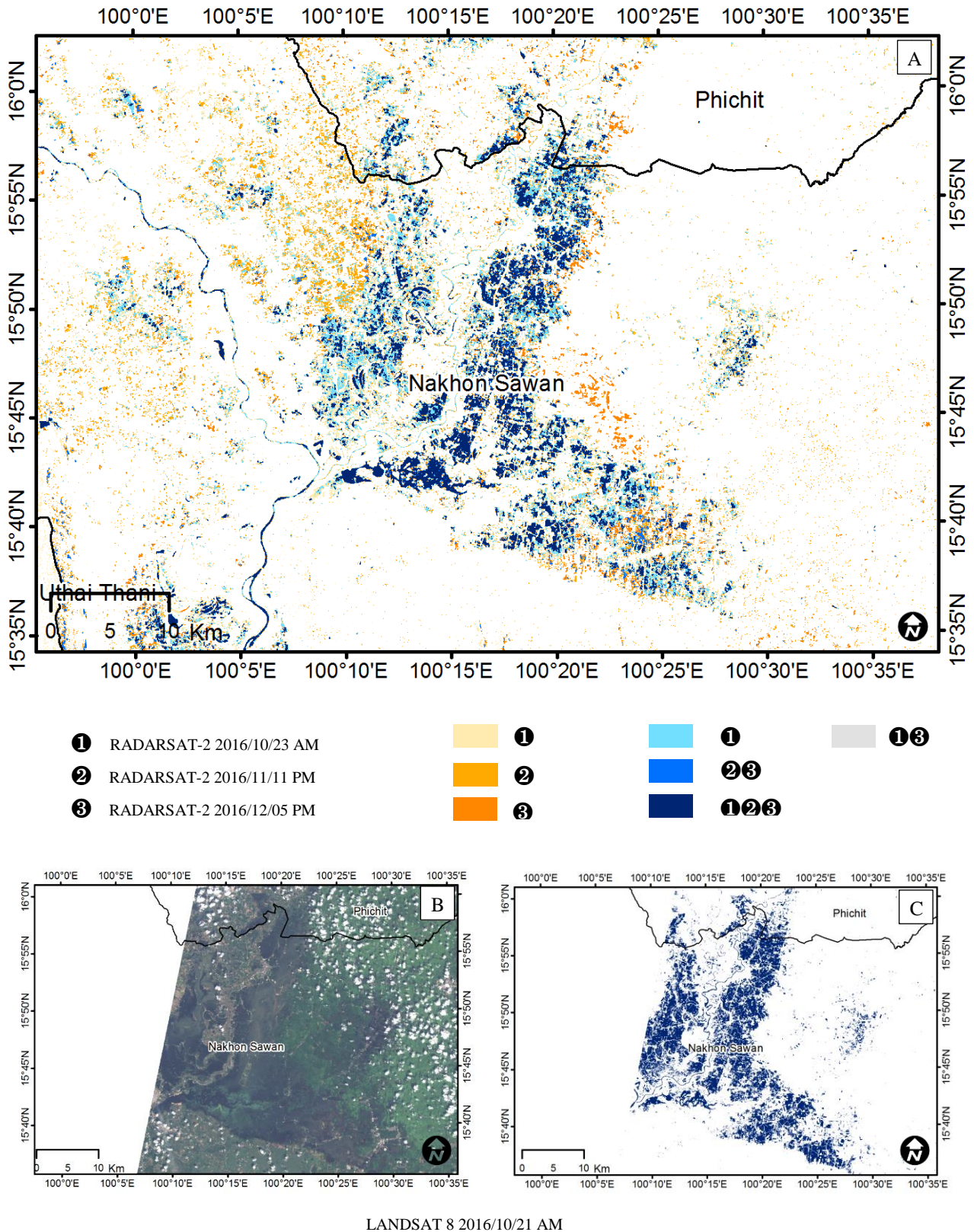
Figure 4-6. A Flood area map from RADARSAT-2 HH+HV automatic thresholding technique for Nakhon Sawan province (NSN) (A). The seven combination colors indicate repetition of the flood in three acquiring dates. Landsat8 true color composite map (B), and flood area map from finding the best accuracy of NDWI (C).
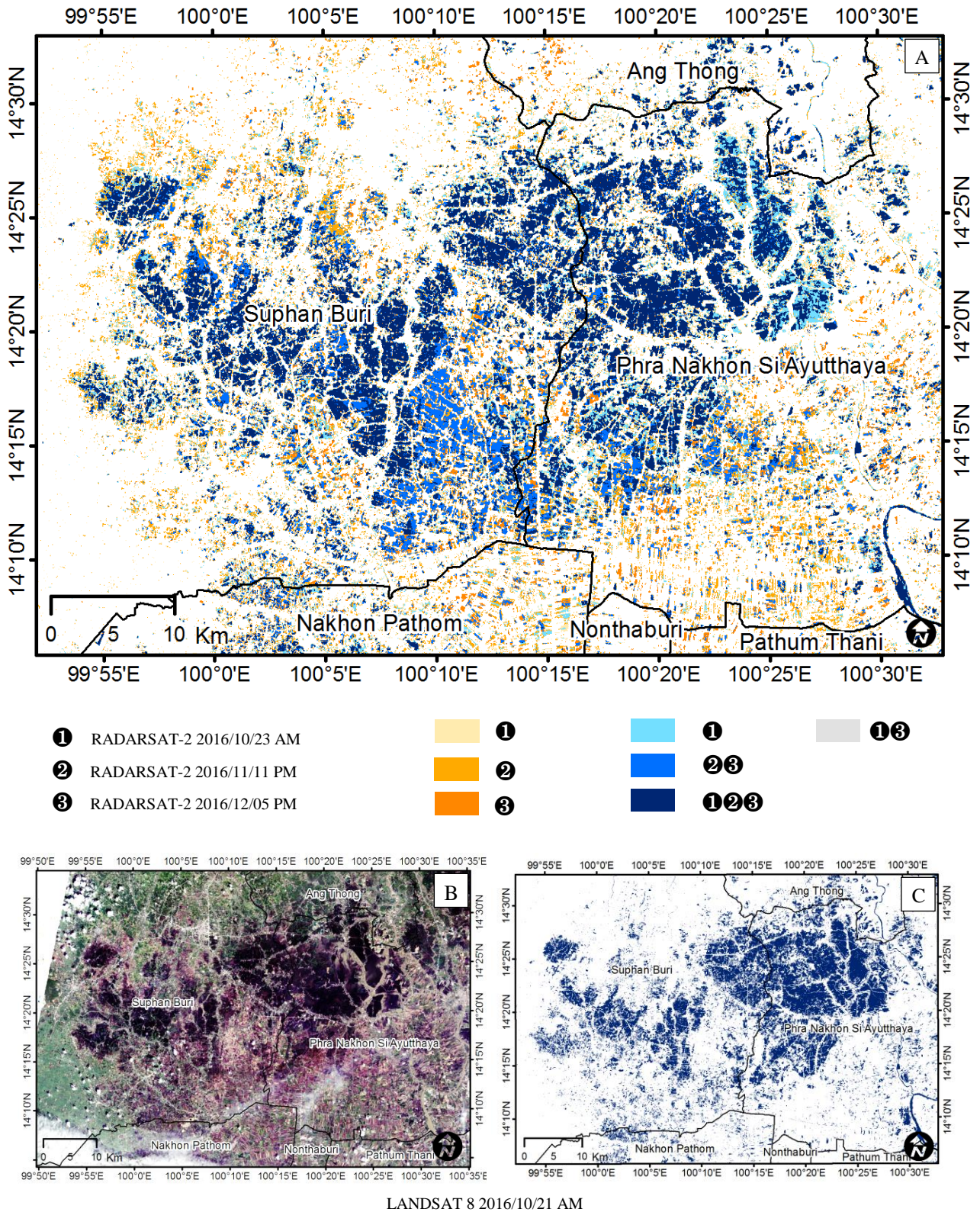
Figure 4-7. A Flood area map from RADARSAT-2 HH+HV automatic thresholding technique for Suphan Buri and Ayutthaya province (SPB&AYA) (A). The seven combination colors indicate repetition of the flood in three acquiring dates. Landsat8 true color composite map (B), and flood area map from finding the best accuracy of NDWI (C).

Table 4-2. Results of the accuracy assessment of the water extraction for the three regions.

Satellite/Date	Data	Method	Threshold Value	N-N (%)	W-N (%)	N-W (%)	W-W (%)	Water (N-W + W-W) (%)	Accuracy (N-N + W-W) (%)
Sukhothai and Phisanulok (STI&PLK)									
RS2 2016/11/11 PM	HH+HV	BA[2]	-14.10 dB	83.5	7.2	2.4	7.0	9.3	90.5
LS8 2016/11/13 AM	NDWI	VS[1]	0.06	-	-	-	-	14.1	-
Nakhon Sawan (NSN)									
RS2 2011/10/24 AM	HH+HV	BA[2]	-12.63 dB	82.2	3.5	3.2	11.1	14.3	89.0
LS8 2016/10/21 AM	NDWI	VS[1]	0.08	-	-	-	-	14.6	-
Suphan Buri and Ayutthaya (SPB&AYA)									
RS2 2016/10/24 AM	HH+HV	BA[2]	-12.63 dB	74.4	6.2	4.8	14.6	19.3	93.3
LS8 2016/10/21 AM	NDWI	VS[1]	0.00	-	-	-	-	20.8	-

(1) BA = find best accuracy thresholding

(2) NE = weight-average neighborhood valley-emphasis thresholding

4.5. Conclusion

The reproduction of proposed method from chapter 3 can be done very quickly due to the water references have been defined. Moreover, the results are very accurate around 90%, especially compare with NDWI of Landsat 8. There are several reasons may cause the accuracy higher than GeoEye-1 in chapter 3. One of the most prominent factors is that the resolution of Landsat 8 (30 m) is quite similar to the RADARSAT-2 SCN mode (25 m). This technique may possibly apply to optical sensor satellites such as Landsat 8 to monitor flood situation with the same water references. However, the optical sensors have limitation to the inclement weather. It is very hard to obtain a good image with clear sky in the rainy season.

Chapter 5

Multi-temporal Correlation Method for Damage Assessment of Buildings from High-Resolution SAR Images of the 2013 Typhoon Haiyan

In this study, damage caused by Typhoon Haiyan in the city of Tacloban, Philippines is extracted from COSMO-SkyMed imagery data. A multitemporal correlation map, i.e., a color composite of the backscattering coefficients obtained on different days and their correlation coefficients, is used to indicate changes. The Hyperboloid Change Index is proposed as a measure of the level of destruction. The method is demonstrated in a three-dimensional Cartesian coordinate system to elaborate the relationships among the aforementioned parameters. Compared to other candidate methods, a hyperboloid equation is found to be the most suitable for change detection, and its resulting positive value indicates that the typhoon had a high level of impact on the area. Potential damage areas are extracted using a thresholding operation, and the results are compared to two WorldView-2 satellite images to specifically assess coastal erosion and damage to buildings and offshore fish traps.

5.1. Introduction

In an SAR interferogram, the coherence (γ), which is derived by processing Single-Look Complex (SLC) co-registered data, is a measure of the correlation in a small neighborhood of geometric conditions. This value also indicates some specific information. A strong coherence implies that two images are homogenous, i.e., that the land surface has not changed and the geometric conditions are very similar. A weak coherence indicates that there has been a change due to one or more conditions, including a significant difference in look angles, constantly moving water surfaces, or land cover changes [1]. Therefore, SLC has been widely applied to land cover classification [2–5]. Furthermore, when used over a short time interval, it can distinguish between processes, such as manmade activities, moving objects, or damage detection [6–11].

Similar to the coherence, the correlation coefficient (R), which is more commonly used in statistics, is a measure of the linear correlation between two variables or pixel values in a local area from two images; the value of the correlation coefficient ranges from -1 and +1. The squared correlation coefficient of the SAR intensity has been proven to be a quick coherence estimator and is implemented in the same manner as coherence [12,13]. Although the coherence and correlation coefficient are very similar in the sense that they provide a value for the correspondence between two-time points, they detect different kinds of change on the ground. The coherence is influenced by the phase difference, which is specific to the spatial arrangement and thus to possible displacements. The intensity correlation is related to changes in the magnitude of the SAR

backscatter, which in turn is related to the roughness permutation [14]. Some studies have shown that the aforementioned methods perform almost identically when identifying the major factor of the decorrelation [15]. However, some studies have determined that the normalized coherence is better suited to and more useful for damage assessment [16,17]. Another study has found that the coherence is more useful for distinguishing slight to moderate damage levels, whereas the correlation coefficient is more sensitive to large surface changes [18]. In contrast, some studies have claimed that the correlation coefficient is slightly more sensitive to ground changes. Furthermore, a combination of both methods has slightly increased the overall accuracy [14].

Recent studies have primarily used the difference and coherence (or the correlation coefficient) to estimate the severity of damage caused by various natural hazards in several ways [19]. In this study, the same parameters are used for damage extraction but with a different concept that overcomes the deficiency of the degree of change not being able to be determined on one scale. A new technique is introduced that utilizes three change parameters instead of the more common one or two.

Because buildings are the most valuable assets of families and businesses, the assessment of the damage to buildings in typhoon events using high-resolution SAR images is a suitable topic of study. Among the types of damage that occur in natural disasters, the damage caused by winds is relatively easy to detect using satellite imagery because winds usually damage roofs. Furthermore, because there is a high probability of cloud cover, optical sensors are often not useful. For this reason, radar sensors are a better choice for rapid damage assessment. Although SARs operate in several frequency bands, the L, C and X bands are most often used. The X-band provides the highest spatial resolution; thus, it was most suitable for use in this study.

Typhoon Haiyan, which is known as Yolanda in the Philippines, was used in a case study. Considered to be the strongest tropical cyclone in recorded history, it struck land in the Philippines with a wind speed of 195 miles (314 km) per hour on November 8, 2013. The typhoon killed more than 6,300 people, displaced 16 million people, and did a total of PhP 89 billion (US$ 2 billion) in damage [20]. In this study, the detection of damage to buildings was carried out using pre- and post-event COSMO-SkyMed (CSK) images and the results were compared to the results of visual inspections of high-resolution optical satellite data. The new change index proposed in this study was designed to be suitable for detecting damage to buildings and determining the degree of change in the general case between two SAR images. The meanings of symbols and acronyms used in this article are listed in **Table 5-1**.

Table 5-1. List of symbols and acronyms used throughout the text.

Acronym	Meaning	Acronym	Meaning
σ^o	backscatter coefficient	D_{SD}	standard deviation D
ϕ	phase	S	summation
γ	coherence	S'	normalized summation
a	hyperboloid constant a	S_{SD}	standard deviation S
b	hyperboloid constant b	R	correlation coefficient
c	hyperboloid semi-major axis	R'	normalized R
d	subtraction	R_{SD}	standard deviation R
d'	normalized subtraction	R_C	combined correlation
s	addition	H'	hyperboloid equation
s'	normalized addition	Δd	absolute difference change index
A	amplitudes	Δw	weight method change index
C	complex number	Δr	cylindrical change index
D	difference	Δh	hyperboloid change index
D'	normalized difference		

5.2. Study Area And Imagery Data

This paper focuses on Tacloban, which is the capital city of Leyte province and its surrounding areas on Leyte Island. Located 580 km southeast of Manila, Tacloban was struck by the eye wall, which was the most powerful part of the storm. The typhoon wrought massive destruction on the city. The widespread devastation was caused by the extreme winds, and lowlands on the eastern side of the city were submerged by storm surges. Because the city had a large population, the number of deaths there accounted for 48% (2,678) of the total deaths in the Philippines in this event [20]. After the super typhoon struck land, the storm surges, and the extreme wind speeds were the major causes of damage. Strong waves and rising water levels, which were assumed to have heights of approximately 4 m, inundated and caused catastrophic damage to the coastal areas [21]. Tacloban's airport was the area most affected due to its location; it was directly hit by the winds and surges. For these reasons, an area approximately 7.0 km wide and 12.3 km long (**Figure 5-1**), an area which includes Tacloban's downtown area, was selected as the study site.

The orbital parameters of CSK were favorable for multi-temporal image analyses. However, the two sets of imagery data were taken from different satellites, and there were rather long time intervals between them. The pre-event image was taken by CSK-1 on August 7, 2013; the post-event image was taken by CSK-3 on November 20, 2013. The temporal baseline (Btemp) was 105 days, and the perpendicular baseline (Bperp) distance between the two satellite orbits was 885.2 m. The images were taken from the descending path with the right-looking HH polarization in the StripMap HIMAGE mode [22]. Both images have incidence angles between 44.99 and 47.19 degrees, and they have a spatial resolution of 0.94 m in the azimuthal direction and 1.57 m in the range direction. The ground resolution was 2.18 m after orthorectification.

Two high-resolution optical satellite images acquired by WorldView-2 (WV-2) were also employed as ground truth data. The pre-event image was acquired on May 18 and the post-event image on November 11, 2013. Both images have 8 multispectral bands (2.0 m resolution) and a panchromatic band (0.5 m). After pan-sharpening using the Brovey technique, 0.5 m resolution multispectral images were prepared.

5.3. Change Detection Workflow

Radiometric calibration provides images in which pixels can be directly related to the radar backscatter of the scene by applying product factor corrections, e.g., the reference slant-range, reference incidence-angle, rescaling factor and the calibration factor. This process results in the backscattering coefficient, which is essential for the comparison of SAR images acquired by different sensors, by the same sensor at different times, or by the same sensor in different modes [23]. To use the backscattering coefficient ($\sigma°$) for detecting surface changes, a calibration must first be applied to a pair of co-registered images. In a

preliminary test, a window size of 5×5 was found to be suitable for the building damage detection. It was therefore adopted for both methods in the coherence and correlation coefficient calculations.

The MTC and MTR mapping methods were applied to evaluate the effects of the typhoon. Subsequently, SARBM3D filtering was applied to reduce the speckle while retaining the backscatter information [24]. An orthorectification using an SRTM 3 sec DEM was applied. This application was intended to compensate for distortions caused by topographical variations in the scene, to compensate for the tilt of the satellite, and to assign real-world coordinates to each pixel.

The change detection process was accomplished by calculating the difference and summation. Then, normalization was carried out on these values, including the correlation coefficient, before the change index was calculated. Finally, thresholding was applied by selecting the appropriate value regarding the pre- and post-event WV-2 images. An assessment of the accuracy was performed by comparing this result to the visualization of the WV-2 images. The two kinds of data were not compared directly but rather by using the final results as the extracted damage percentage. A flowchart of the processes is shown in **Figure 5-2**.
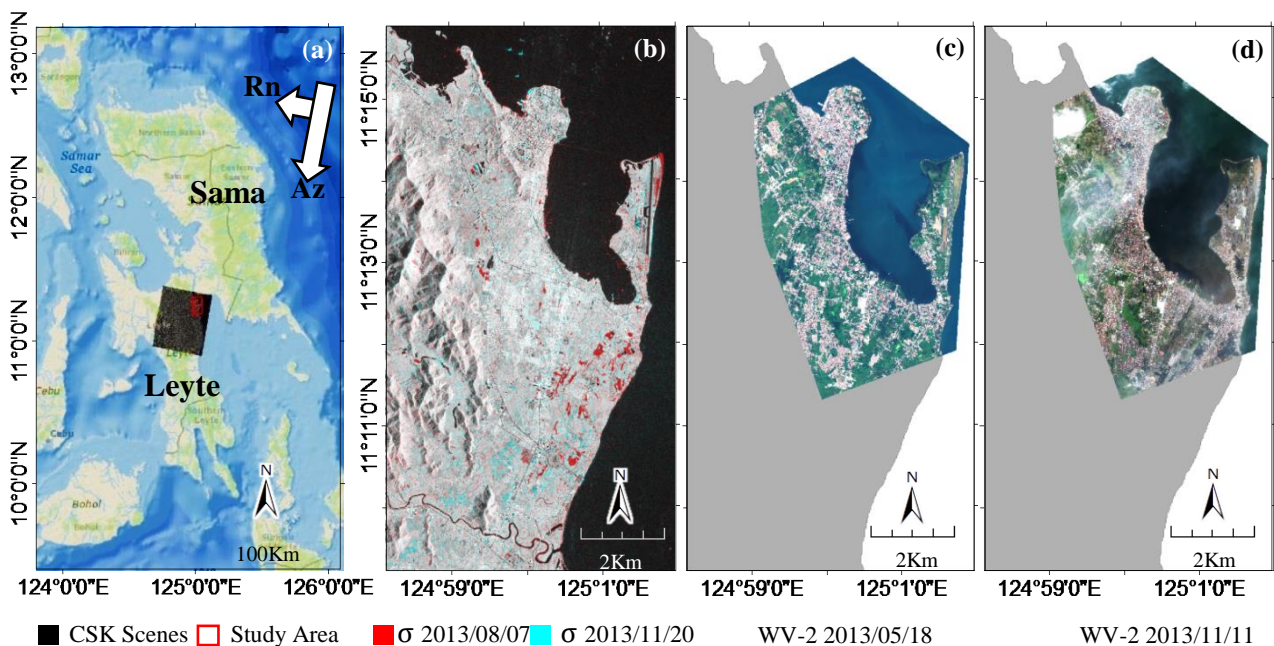
Figure 5-1. (**a**) The footprint of the CSK scenes and Tacloban, Leyte study area. (**b**) Color composite of the pre- and post-event CSK backscattering coefficients. (**c–d**) True color composite of the pre- and post-event WV-2 images.

5.3.1. Coherence (γ) and Correlation (R)

In repeat-pass interferometry, the coherence (γ) is derived from a pair of images in the same local area taken within a certain time-interval. The exact coherence and the relation between the interferometric phase dispersion can be derived using a mathematical operation. Therefore, the coherence is frequently calculated as an estimator [25] using two co-registered single-look complex (SLC) images, as in equation (1):

$$\gamma = \frac{\sum C_1 C_2}{\sqrt{\sum |C_1|^2} \sqrt{\sum |C_1|^2}}, \tag{1}$$

where C is a complex number with phase (ϕ) and amplitude (A) [26].

The Pearson correlation coefficient (R) is a measure of linear dependence and is defined as the covariance of two variables divided by the product of their standard deviations. In this case, it was calculated from the backscattering coefficients (σ°) of the two images using equation (2) with a moving window. Because this statistic determines the linear trend, and the SAR intensity is distributed in an exponentially increasing manner, it was appropriate to use decibel units (dB), which are on a logarithmic scale.

$$R = \frac{\sum (\sigma_1^0 - \overline{\sigma_1^0})(\sigma_2^0 - \overline{\sigma_2^0})}{\sqrt{\sum (\sigma_1^0 - \overline{\sigma_1^0})^2} \sqrt{\sum (\sigma_2^0 - \overline{\sigma_2^0})^2}} \tag{2}$$
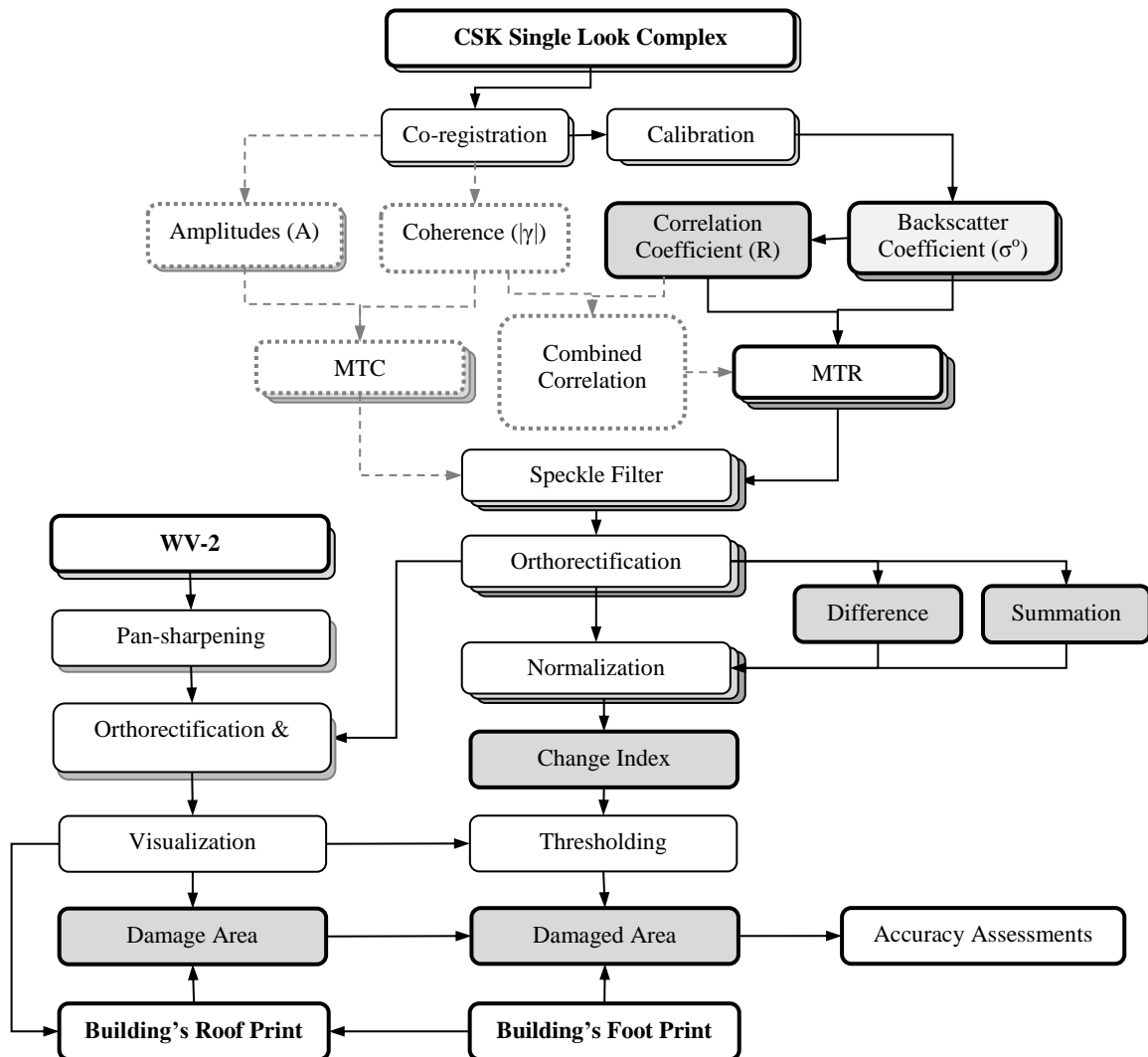
Figure 5-2. Data flow diagram for Multitemporal Coherence (MTC) and Multitemporal Correlation (MTR) processing. Note that that the modules shown with dotted lines were not used to produce the final results.

5.3.2. MTC and MTR Visual Interpretation

For the MTC map shown in **Figure 5-3(a)**, red is used for the amplitude of the pre-event (A1), green for that of the post-event (A2) and blue for their coherence (γ). For the MTR map shown in **Figure 5-3(b)**, red is used for the backscattering coefficient of the pre-event (σ_1), green for that of the post-event (σ_2) and blue for their correlation coefficient (R). The color composite of the SAR images visually provides information on the increase/decrease of the backscattering intensity at different times. The interferometric coherence (γ) and correlation coefficient (R) provide more information on the earth surface conditions, which vary within a small local area. However, using these measured values alone limits the interpretation because they do not indicate the trend of stage changes, which may be increasing or decreasing. Therefore, they are usually used in conjunction with a pair of amplitudes (intensity and backscatter coefficient) or their difference values. In various fields of change detection, RGB color composite mapping is considered to be a useful method

[27,28]. When a color composite is used, the results of the Multi-temporal Coherence (MTC) and Multi-temporal Correlation (MTR) methods can be represented by colors closer to natural ones, which are easier to understand [7,8].

Because the coherence is a complex correlation coefficient, it is generally used as an absolute value or as the amplitude of coherence in real numbers. In a stable stage in which there is no change on the surface, the backscattering in the two images is equal. The coherence was high for the urban area, due to its high reflectivity and phase stability, but it was low for other land cover surfaces, because of the contribution of amplitudes and phase instability. Based on these results, white pixels were used to represent urban areas; yellow pixels were used to represent general land cover. Alternatively, the correlation coefficient had both positive and negative values, depending on the trend of the changes. Thus, in the stable stage, urban areas can have either white or yellow pixels, and the general land cover is represented using light yellow pixels. In both cases, smooth surfaces, e.g., roads and bodies of water may be either blue or black because of the ambiguity of the correlation. Low-correlation surfaces that have decreasing reflectances, e.g., areas that have flooded or that contain objects that have been removed from the scene, are shown in red, whereas those that have increasing reflectances, e.g., areas with destruction and that contain replaced objects in the scene, are shown in green.

To more clearly explain the color composition derived by the MTR method, an RGB color model is shown in **Figure 5-4(a)**, and 3D scatter plots for each pixel are shown in **Figure 5-4(b)** and **(c)** (displaying 1% of the pixels for rendering performance). The color gradient from black to blue represents smooth surfaces, such as bodies of water, roads, and runways, where the backscatter was low. Alternately, flooded areas that are still remaining in the southern part of the city exhibit a reddish-magenta color due to the reduction of the backscatter. Other land cover and vegetation areas with low correlation coefficients can be recognized in yellow. The most important parts are the built-up areas in the city. If a building did not suffer damage, it is shown in white or yellow because its backscatter remained high with only slight changes. In contrast, if the typhoon caused damage to a building, a decrease or increase in the backscatter can be observed. Due to the washing away of buildings/houses or the accumulation of debris, the MTR color composite is red (decreasing backscatter with a high negative correlation), magenta (increasing backscatter with a high positive correlation), green (increasing backscatter with a high negative correlation) or cyan (increasing backscatter with a high positive correlation).

In this study, we attempted to use the correlation coefficient for several reasons. For example, the correlation coefficient can be applied to images that have lost their phase properties, e.g., multilook, calibrated and georeferenced data [29, 30], and the correlation coefficient can be calculated rapidly using real-valued operations. It can also be used in cases of decorrelation due to large perpendicular baselines. Another main reason that we chose the correlation coefficient is that it shows a two-tailed normal distribution. This characteristic is suitable for our proposed method, which classifies the level of change from both sides of their mean. Since the coherence shows a one-tailed distribution, higher values refer to

larger displacements, so it was inapplicable to the normalized value discussed in the next section. It might be used in different ways.

In the recent studies previously mentioned, several techniques have been attempted to combine the two statistics in order to retain the information contained in both and to improve overall accuracy. For example, the correlation coefficient has been used as the primary main statistic with the coherence used as a multiplier. As with the correlation coefficient, their product ranges from -1 to 1. We found that this combination did not greatly improve the results, and there was slightly more noise. Therefore, only the correlation coefficient was used for the processing in this study. Enlarged images of the Tacloban airport terminal and graphs of the corresponding profiles are shown in **Figure 5-5**.

From the graphs of the profiles, the land cover was divided into 6 categories: trees, car parking areas, buildings, aircraft parking areas, grass, and runways. First, the aircraft parking areas and runways had the lowest reflectance. Some noise, the results of normal SAR characteristics and debris spread over the surfaces, was present, In contrast, the aircraft parking area and runway coherence were highest, although it was less than 0.5, and the correlation fluctuated between -0.5 and 0.5. Second, the grass area had a higher reflectance and slightly lower coherence, and the correlation was distributed over a wider range. Third, the tree areas had increased reflectance, and the correlation coefficient was slightly more negative. This area could not be captured by the coherence because all trees were totally destroyed, but median strips still remain. Next, the car parking area, which was a mix of empty space and three rows of trees, had combined characteristics and three peaks. Its reflectance decreased by an equivalent amount. Lastly, the east side of the Tacloban airport terminal building was destroyed, as evidenced by the area with the highest reflectance and reduced peak. The coherence slightly dropped in the damaged area, whereas the correlation coefficient was slightly negative.

5.4. Change Index

In the case of the visual interpretation, color composites produced by the MTC and MTR methods have slightly different representative colors, especially when normalized by the standard deviation. These maps provide more potential change information than two-color composites of the backscattering intensity (or coefficient) and are easier to visually interpret, but the process of using them to estimate the damage is still complicated. Recent studies have used several change indices, including the difference, coherence, and correlation coefficient, to detect and classify damage levels [7,13,31–33]. According to the color composite, red, green, cyan and magenta refer to pixels that have explicitly changed. Classifying them using a 2D model
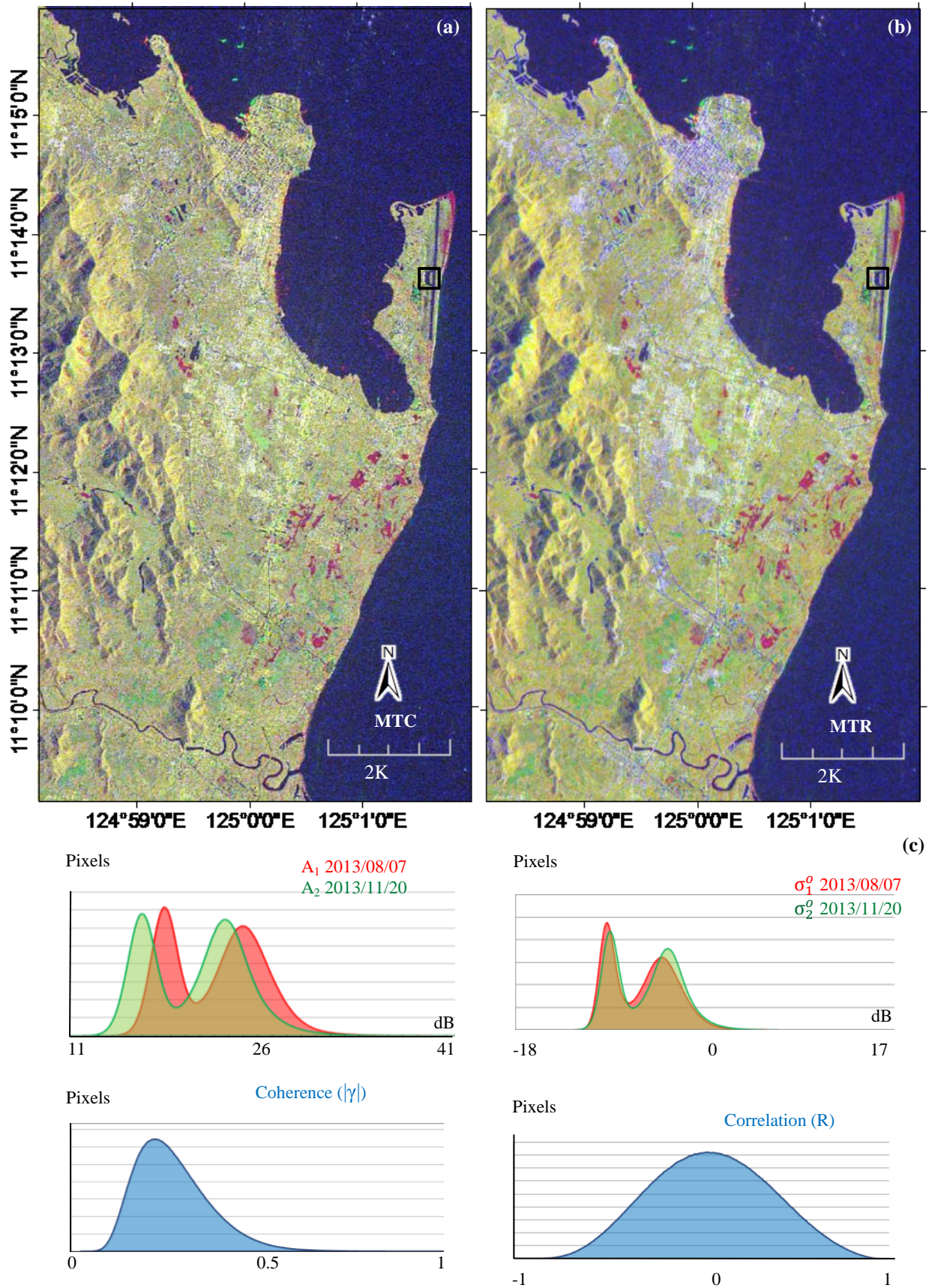
Figure 5-3. **(a)** MTC and **(b)** MTR maps enhanced using the standard deviation technique and **(c)** their histograms.
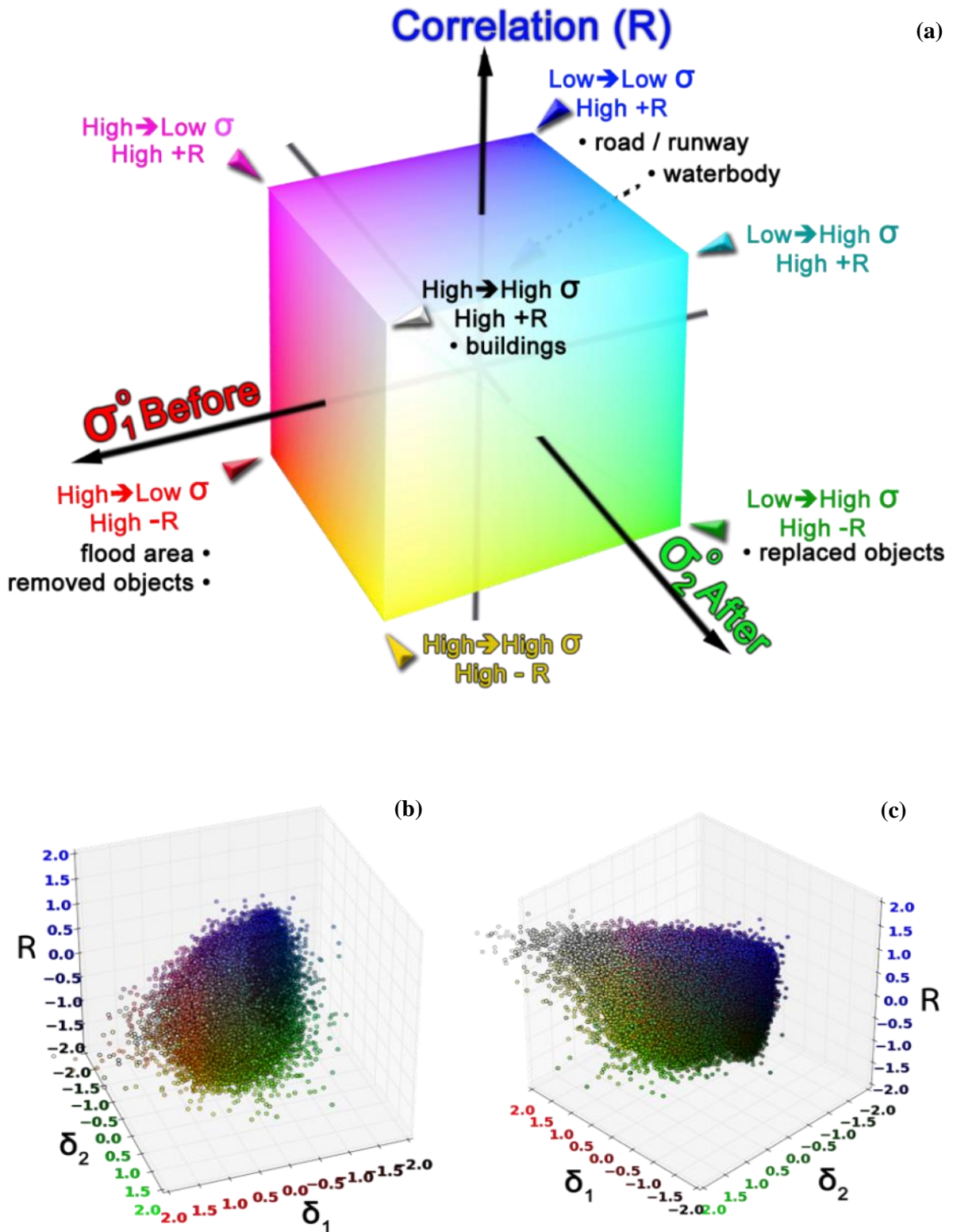
Figure 5-4. (a) MTR demonstrated in the RGB color space. **(b–c)** 3D scatter plots of the MTR scaled by 2 times the standard deviation (2 SDs).
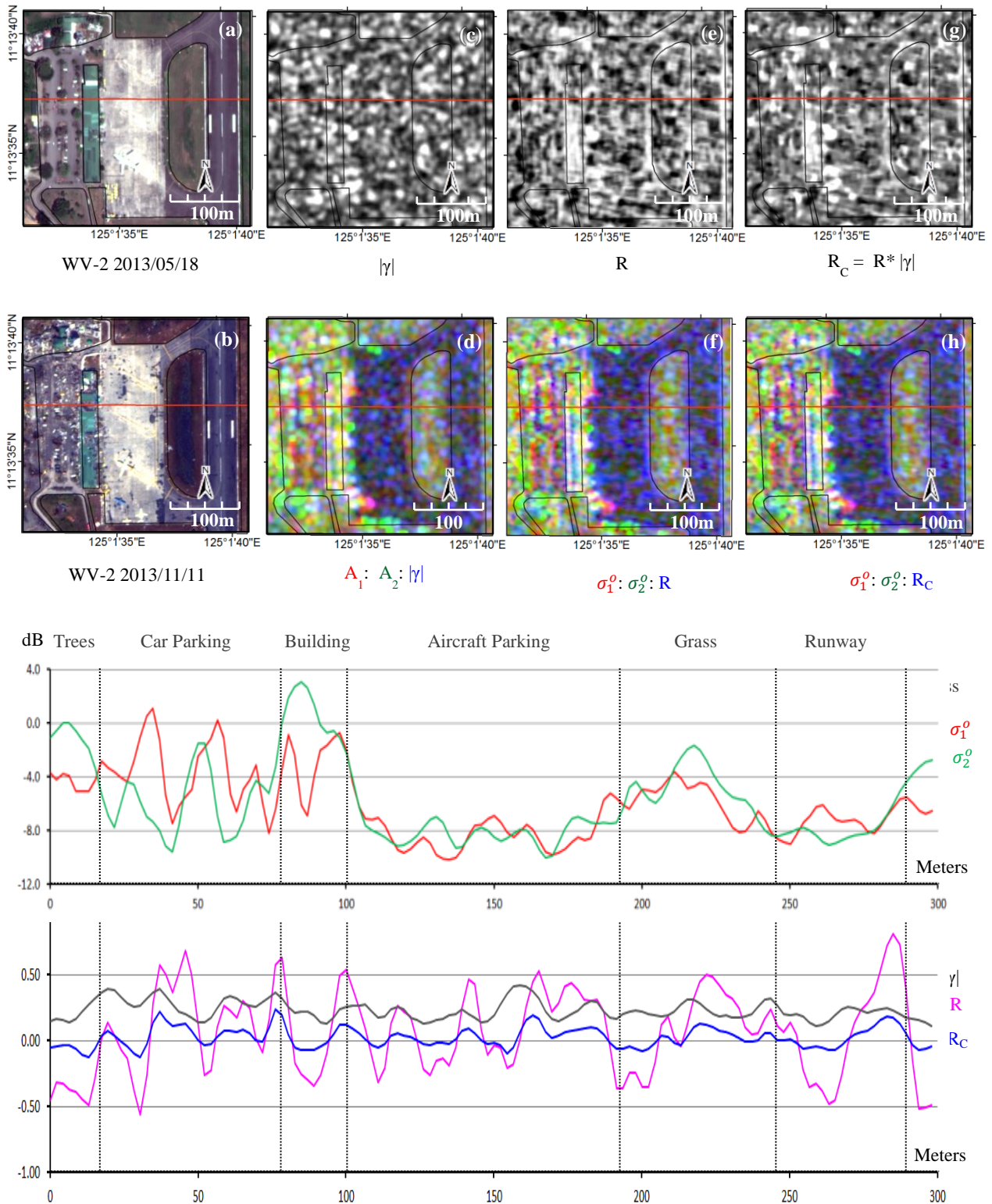
Figure 5-5. Enlarged image of the Tacloban airport terminal: **(a)** WV-2 pre-event, **(b)** WV-2 post-event, **(c)** $|\gamma|$, **(d)** MTC, **(e)** R, **(f)** MTR, **(g)** R_C and **(h)** MTR_C maps, enhanced using the standard deviation technique.

usually has some weaknesses, which will be discussed later. The new method in 3D space, the method proposed in this study, is expected to overcome shortcomings in the use of the change indices.

5.4.1. Difference and Summation

The difference (D) is a very simple index and is commonly used to indicate a difference in spatial analyses, but the summation (S) has rarely been used. Both are calculated using the average value in a moving window. The two indices have a reciprocal relationship when expressed in Euclidean vectors or a Cartesian coordinate system. When simultaneously rotating the pre-event values ($\sigma1o$ to the red axis) and post-event values ($\sigma2o$ to the green axis) 45o counterclockwise, the operation produces the subtraction (d) axis in equation (3) and the addition (s) axis in equation (4). In this case, the difference (D) and summation (S) can be obtained by multiplying d and s by a constant value, $\sqrt{2}$, as shown in equation (5). We can infer that the summation (S) is a value on the yellow axis and that the difference (D) is a value on the axis perpendicular to the S-axis in the red-green plane, as shown in **Figure 5-6**. From this insight, the axis rotation, any equations composed of these parameters can be expressed in a 3D space.

$$d = \overline{\sigma}_2^o \ \cos 45° - \overline{\sigma}_1^o \ \sin 45° = \frac{\overline{\sigma}_2^o - \overline{\sigma}_1^o}{\sqrt{2}} \tag{3}$$

$$s = \overline{\sigma}_2^o \ \sin 45° + \overline{\sigma}_1^o \ \cos 45° = \frac{\overline{\sigma}_2^o + \overline{\sigma}_1^o}{\sqrt{2}} \tag{4}$$

$$D = \overline{\sigma}_2^o - \overline{\sigma}_1^o = \sqrt{2}d \ ; \ S = \overline{\sigma}_2^o + \overline{\sigma}_1^o = \sqrt{2}s \tag{5}$$
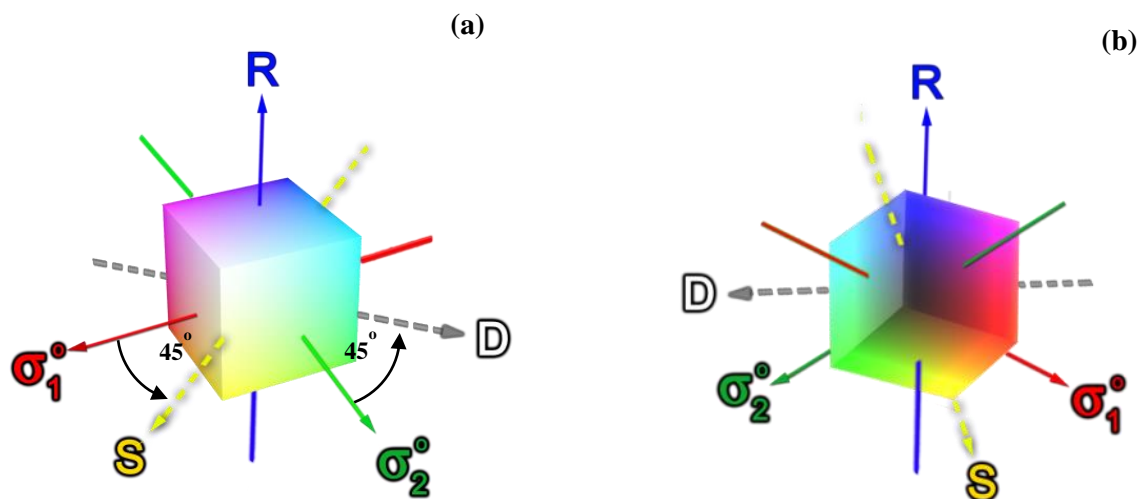
Figure 5-6. (a) The rotation of the σ_1 and σ_2 axes $45°$ counterclockwise results in the Summation (S) and Difference (D) axes. **(b)** The backside view of (a).
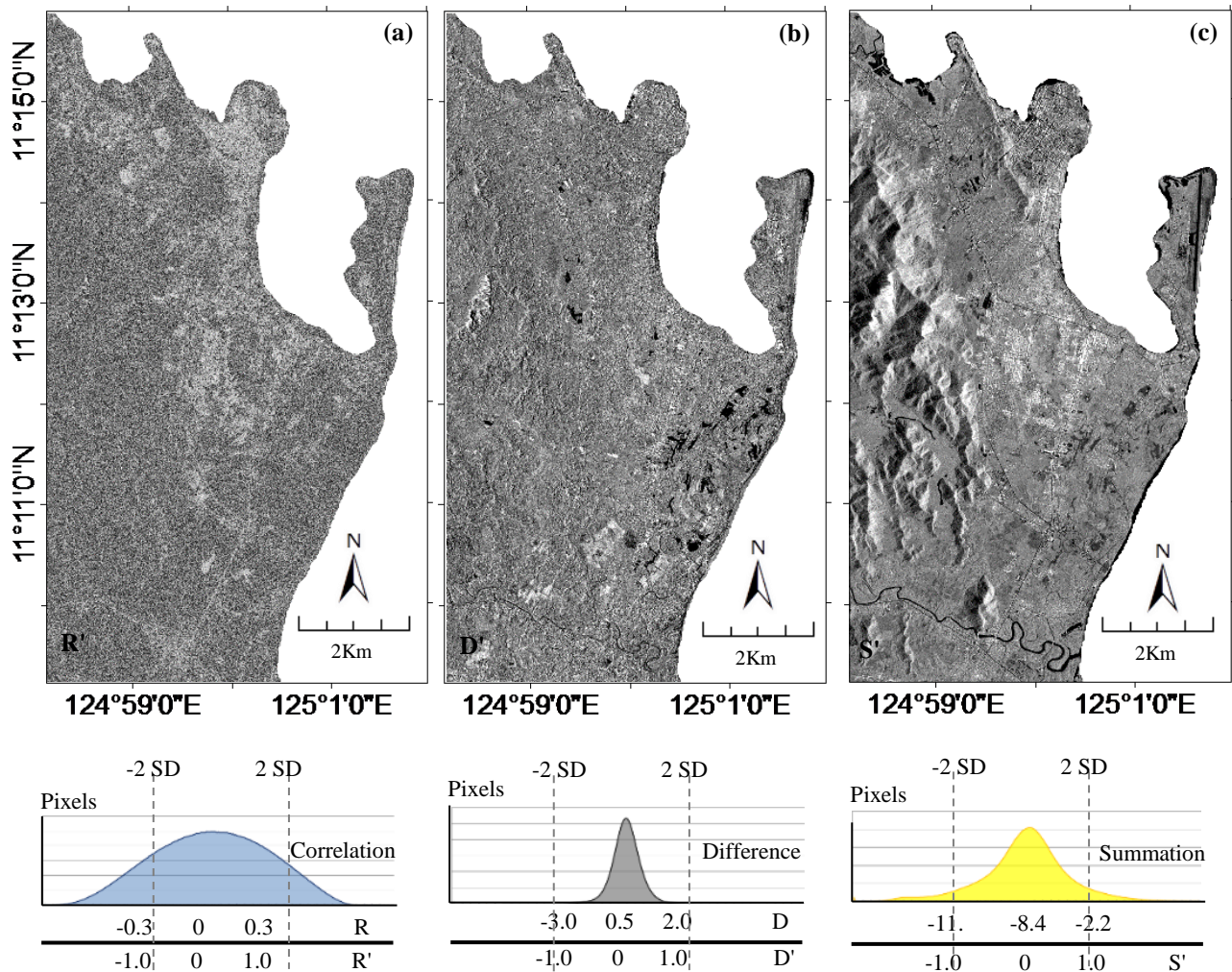
Figure 4-7. **(a)** Normalized Correlation (R'), **(b)** Difference (D') and **(c)** Summation (S') obtained from the backscattering coefficients of the MTR map

5.4.2. Change Index

Because the units and ranges of R, D, and S are not the same, normalization was introduced. All of the factors used to calculate the change indices in this study were normalized by equation (6). Each pixel value was subtracted from the mean value and divided by twice the standard deviation (SD) of the entire image. Thus, a normalized positive value represents a value above the mean; a negative value represents a value below the mean, and 1.0 represents a value twice that of the standard deviation. Each normalized value (Z-score) is denoted using the prime symbol. According to the statistical three-sigma or 68–95–99.7 rule, which separates the normal distribution into three ranges using the standard deviation, normalized values of 1.0, which are located in range number 2, should cover 95% of the total pixels. Using the normalized score, it can be seen that D' is equivalent to d' and S' to s' in equation (6). The normalized results are shown in **Figure 5-7**.

$$R' = \frac{R - \overline{R}}{2R_{SD}}; \ d' = D' = \frac{D - \overline{D}}{2D_{SD}}; \ s' = S' = \frac{S - \overline{S}}{2S_{SD}} \tag{6}$$

In this study, the absolute difference method (Δd) of equation (7) would give an ambiguous result because it could not discriminate between the blue and black pixels representing bodies of water and the white and the white and yellow pixels representing natural vegetation and buildings, according to the transformed RGB model shown in **Figure 5-6**. Employing a combination using the correlation coefficient, as is used in some methods, would not improve the discrimination. For example, the weight method (Δw) [13] and the cylindrical or radius method (Δr) of equation (7) also have the same weaknesses.

$$\Delta d = |D'|; \ \ \Delta w = |D'| - 0.5R'; \ \Delta r = \sqrt{R'^2 + D'^2} \tag{7}$$

This problem can be solved by expressing the MTR in 3D space. A new change index is proposed and calculated using the normalized values of the difference (D'), summation (S'), and correlation (R'). According to the previous discussion, the D'-, S'- and R'-axes are mutually orthogonal. A hyperboloid of revolution can be obtained by rotating a hyperbola around its semi-minor axis (S'). The standard hyperboloid form in equation (8) is reduced to that in equation (9) when the constants a, b, and c are equal to 1. When a, b and c are not equal to 1, a standard deviation weight instead of the 2 in equation (6) can be introduced to simplify the hyperboloid equation.

$$H' = \frac{R'^2}{a^2} + \frac{D'^2}{b^2} - \frac{S'^2}{c^2} \tag{8}$$

$$H' = R'^2 + D'^2 - S'^2; \ \text{when } a = \ b = c = 1 \tag{9}$$

All of the R', D,' and S' values that return the same H' value in the equation are located on the same hyperboloid surface. Negative values representing a hyperboloid of two sheets indicate a greater similarity. Zero values represent a conical surface, the differences, and similarities of which are almost equal. Positive values representing a hyperboloid of one sheet indicate greater differences. By spreading the hyperboloid "spittoon," as shown in **Figure 5-8(d)**, this operation was capable of differentiating among bodies of water, natural vegetation and buildings. Because the H' value is calculated using the quadratic polynomial formula, each range on the scale is squared. The change index value is much easier to recognize in the linear scale if the square root is taken. Because H' can be a positive or negative number, the square root must apply to the absolute value of H', and its sign must be retained, as in the definition of the Hyperboloid Change Index (Δh) in equation (10).

$$\Delta h = \text{sign}(H') \sqrt{|H'|} \tag{10}$$

A comparison of the results obtained using the proposed method and those obtained using other candidate methods is shown in **Figure 5-8**. Among those methods, Δh demonstrated the best classification capability. This is mainly because it was developed from three parameters, which included the summation in the equation in such a way that the magnitude of the intensity from the original data is preserved. This index can indicate the change in conjunction with the reflectance, so its appearance is much clearer than those of the other indices. It is capable of distinguishing changes very clearly. Moreover, the difference between the sea and mainland can easily be identified. Yellow areas with slightly positive values represent slight changes, such as the changes seen in the natural vegetation. Blue areas with high negative values were almost unchanged over the period. These included bodies of the water, roads, runways, and buildings. In this case, a double bounce effect area can be identified as corresponding to a very low value of the index, since the summation of the intensity is very high, as in the case of the deep blue on the eastern side of the Tacloban airport terminal buildings, for instance. Although Δh was able to capture this phenomenon, which could not have been captured by the other indices, the area was not identified as an area of destruction, because the reflection from building walls was hard to see in nadir images acquired from optical satellites. Red areas with highly positive values represent significant changes, such as damaged and flooded areas or the growth of agricultural plants. For large buildings, the index value was high due to the loss of surface. Therefore, the reflectance was increased, with a high correlation. The growth of vegetation over a period of 105 days, as shown on the map, would not be counted as damage caused by the typhoon. To avoid this possibility, the pair of SAR images should be taken over the shortest possible time interval.

5.5. Damage Extraction and Accuracy Evaluation

Thresholding is the simplest method of evaluating damage levels. A suitable threshold value for the Hyperboloid Change Index (Δh) was selected by comparing its results with the high-resolution optical images. Because of limitations in visibility due to cloud cover, two WV-2 images taken 177 days apart were selected and used as the truth data. An enlargement of a sample area at the Tacloban airport is shown in **Figure 5-9**. Because the changed index value was designed to be a function of the standard deviation, a value of 1.0 is equivalent to twice the standard deviation, which covers approximately 95% of the total pixels. Therefore, the threshold value would be close to 1.0. By varying the threshold by trial-and-error to suitably detect damage with the least noise, a value of 1.0 was selected. The extraction result is shown in **Figure 5-10(b)**, wherein the image has been classified into 3 classes. The classes with threshold values lower than 1.0 appear noisy. Enlarged images of the Tacloban airport terminal are shown in **Figure 5-11**.

The coastal erosion of the northeastern cape can be easily distinguished from the WV-2 image and the extracted results from the proposed method. Moreover, destruction offshore, e.g., fish traps and boats, can also observe along the west coast in **Figure 5-9** and **Figure 5-10**.

For the building damage detection, the results obtained using the same threshold value sufficiently revealed the damage. It was difficult to separate the buildings from much of the debris spread throughout the city, and the resolution of the CSK images made accurate assessment difficult. Building damage detection from remote sensing imagery can be carried out by several sensors, e.g. optical, SAR, and LiDAR. In this regard, the optical imagery with spatial resolution finer than one meter is well suited to be a reference data source. Because optical satellite images are acquired with views almost from the nadir, only building information on the roof and the presence/absence of debris around the lateral walls are collected [34]. Although the superimposition of pre- and post-event optical images results in automated change detection, visual interpretation is widely used in practice [35]. Based on a field survey and a visual interpretation of high-resolution optical satellite images, the damage level, focusing on the roofs, was classified into two categories by Tohoku University [36]. The high damage or destruction class was used when the roof of a building had been reduced by more than 50%, or the structure had been washed or blown away. The low damage or survival class was used for buildings with small variations in their geometry or roof shape. Unlike optical sensors, an SAR sensor can capture, due to its oblique observation scheme, more information relevant to lateral wall damage, but its performance in urban areas is limited by shadowing and layover issues [37].

Due to the lateral observations and surface roughness measurements inherent to SAR, the backscatter from a cluster of small buildings, when they were destroyed, would be reduced because of the reduction of the double bounce effect. Furthermore, this effect can strongly reduce backscatter when numerous buildings are washed away [38].

In this study, the extracted results had low accuracy for small buildings in dense areas, but accuracy was good enough to extract the damaged portions of large buildings. The damage assessment was examined using 545 large buildings with footprint areas larger than 500 m2, buildings that were selected from auxiliary vector data. The damage was visually assessed from roofs in the pre- and post-event WV-2 images. The damage was then assigned to three classes using the relative damaged area in the footprint of each building: less than 10% as no damage or minor damage, from 10% to 50% as moderate damage, and more than 50% as major damage or collapse. The statistical results are plotted in **Figure 5-12**, and enlarged images for the 10 largest buildings are shown in **Figure 5-13**.

The classification procedure was carried out in two steps. First, the major damage was classified. The moderate damage was then distinguished from the minor damage. The threshold value was selected by the extracted % of building footprint that returned the best accuracy. Comparison results in Table 2 show that the proposed index Δh was better than that of other candidate methods. Although all methods yielded good accuracy with almost the same value, 89%, the proposed index result was superior in terms of damage extraction for several reasons. First, it had the lowest amount of noise in the extracted area. Second, it captured the damage to buildings with the best performance, as the damage level extracted from the area was highest with the proposed method, close to 50%, which we define as major damage.
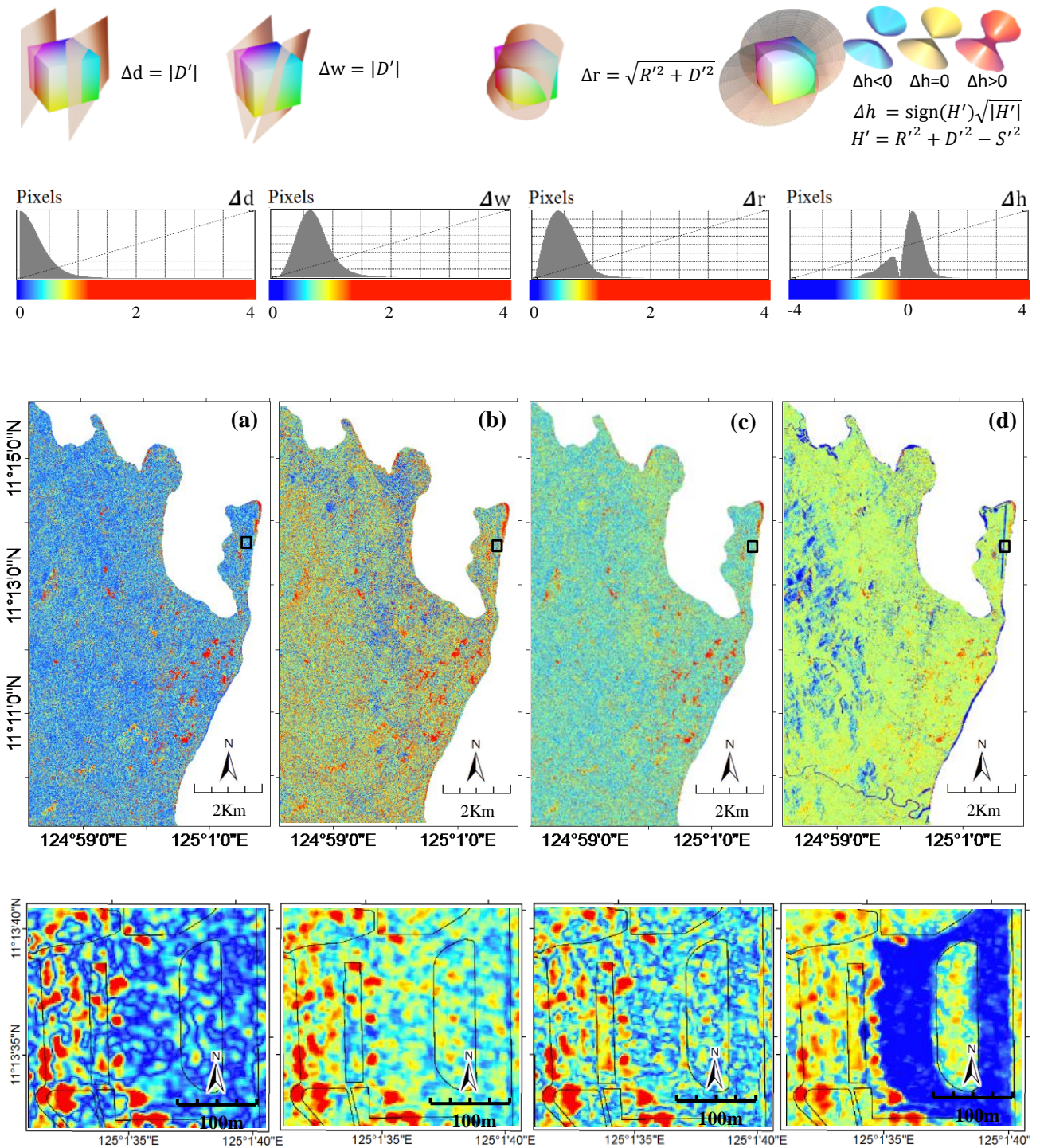
Figure 5-8. Results of the change detection using the candidate methods: **(a)** absolute difference (Δd), **(b)** weight (Δw), **(c)** circular (Δr), **(d)** proposed hyperboloid method (Δh) and enlarged images of the Tacloban airport terminal.

σ 2013/08/07   σ 2013/11/20   R   WV-2 2013/05/18   WV-2 2013/11/11
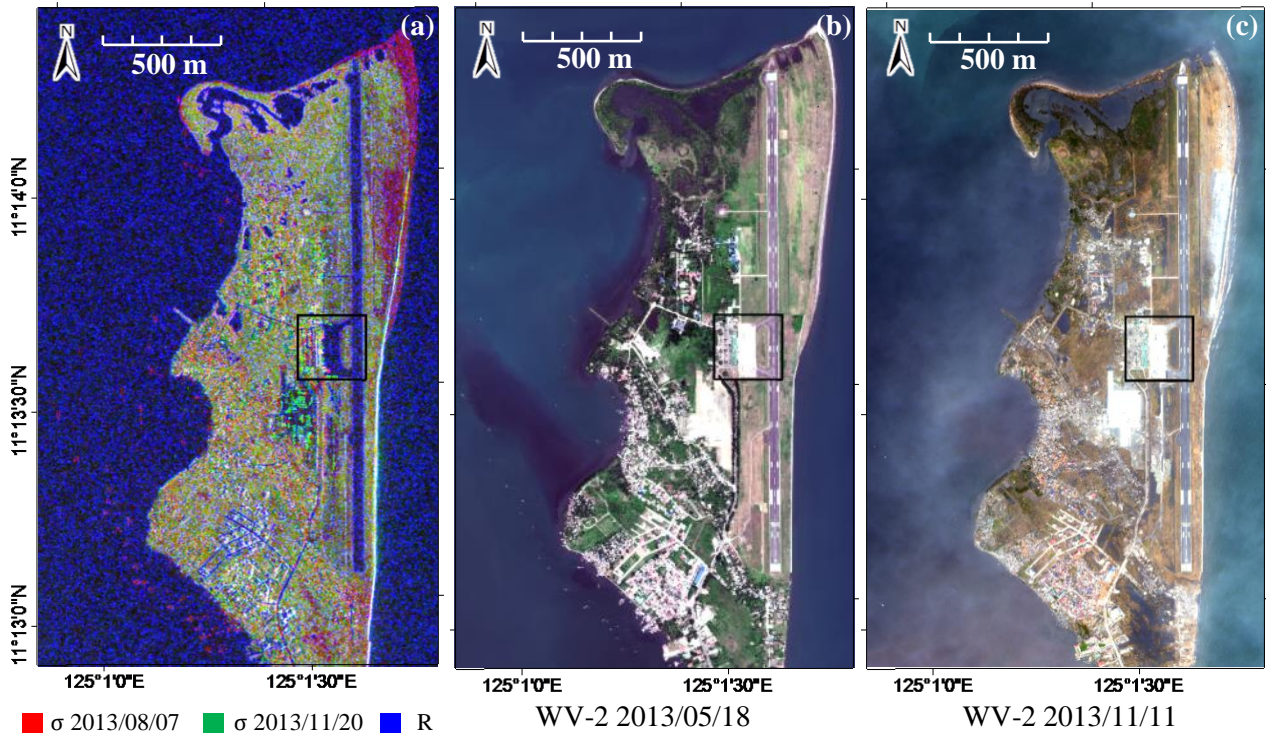
Figure 5-9. Enlarged images of the Tacloban airport: **(a)** MTR map, **(b)** the pre-event WV-2 image and **(c)** the post-event WV-2 image. Black-bordered areas are close-ups of Tacloban airport.

Δh -2.4   -1 0 1   6.2 Δh 0.8-1.0   1.0-1.2   ≥ 1.2   WV-2 2013/11/11 Δh ≥ 1.0   Buildings
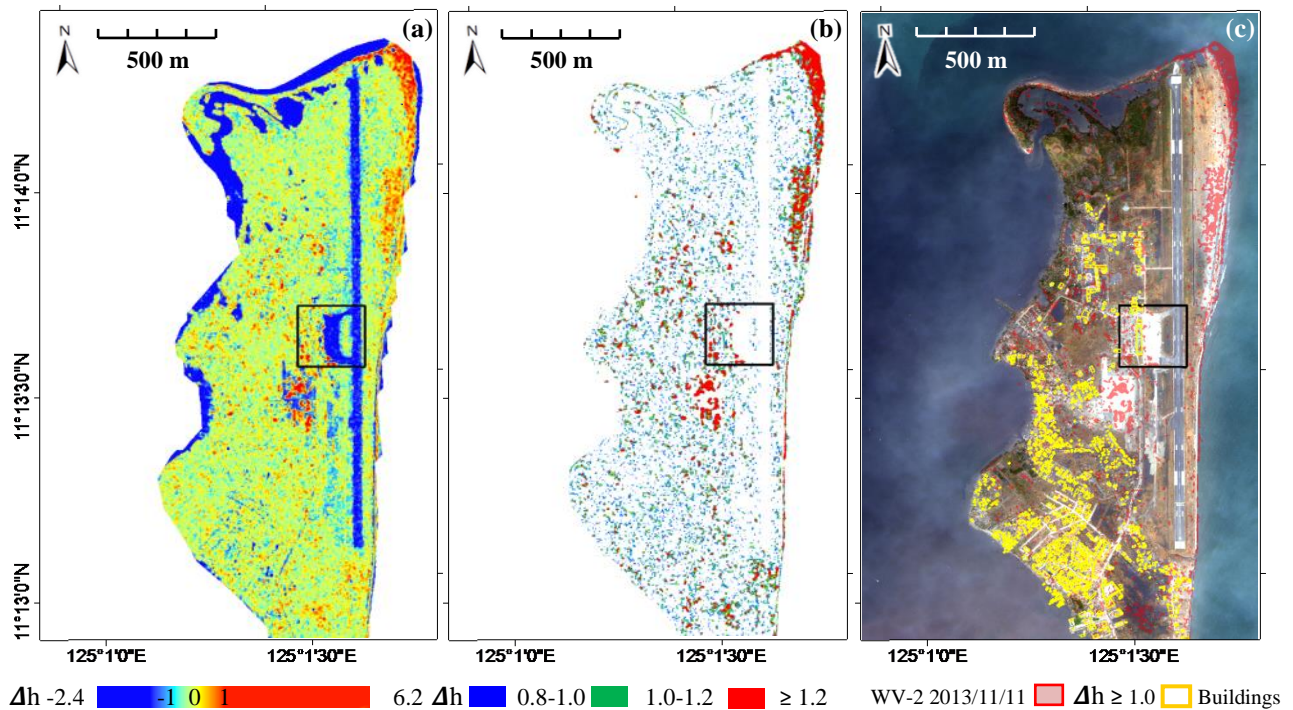
Figure 5-10. Assessment of damage to Tacloban airport: **(a)** Hyperboloid Change Index (Δh), **(b)** thresholding into 3 classes, **(c)** the extracted damage areas overlapping on the post-event WV-2 image. Black-bordered areas are close-ups of Tacloban airport.
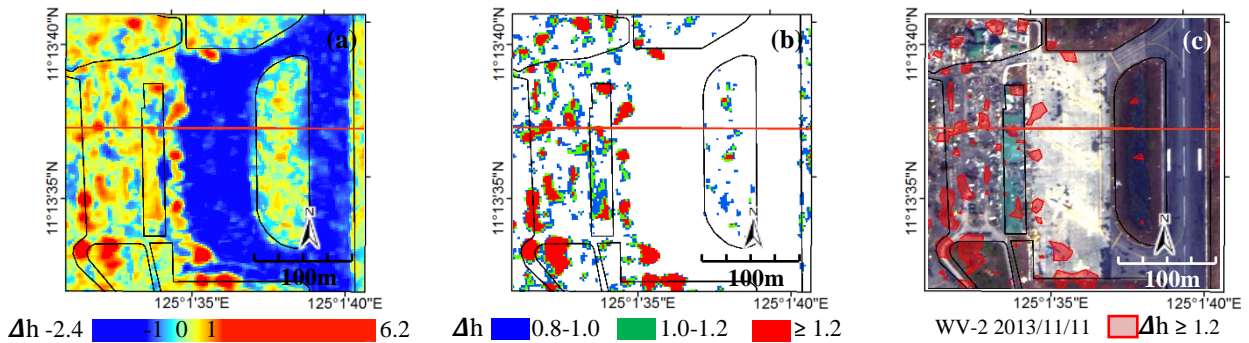
Figure 5-11. Assessment of damage to Tacloban airport: **(a)** Hyperboloid Change Index (*Δ*h), **(b)** thresholding into 3 classes, and **(c)** the extracted damage areas superimposed on the post-event WV-2 image.
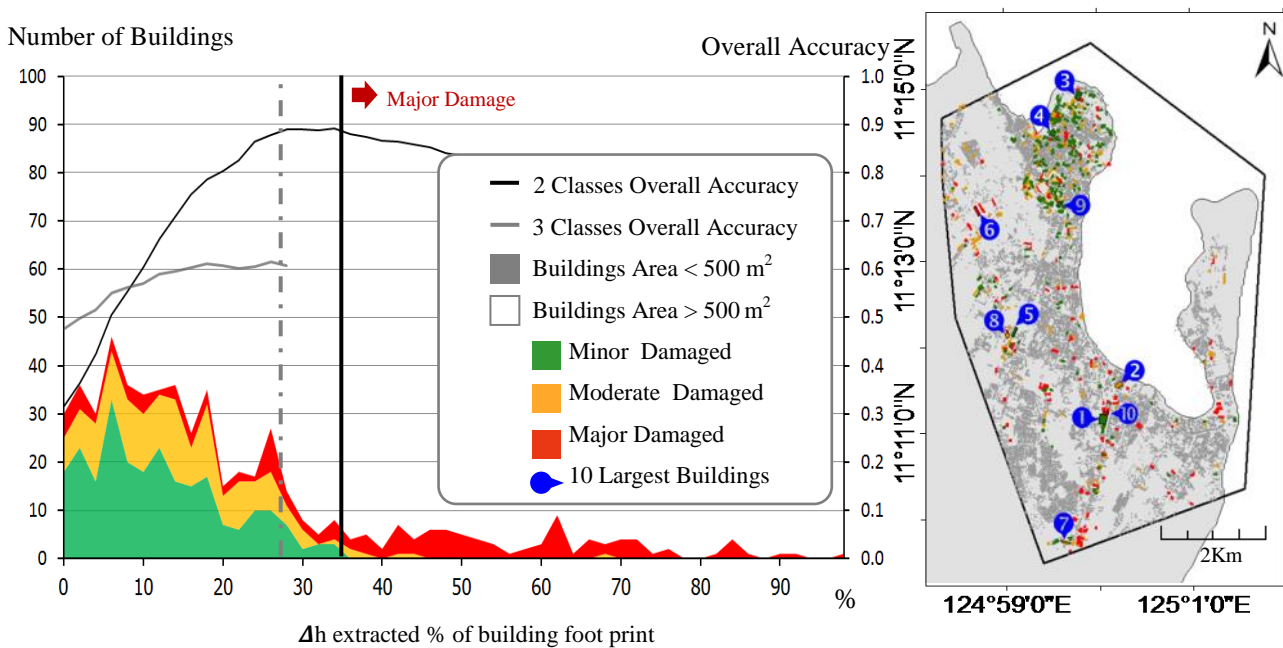
Figure 5-12. Damage extraction diagram when *Δ*h's threshold 1.2 for 545 large buildings with footprint areas is more than $500\,\text{m}^2$, shown in the right-side map. The damage levels were classified to 3 classes by visual inspection of the WV-2 images.

Table 5-2. Comparison of candidate methods to Δh by extracted area, best accuracy, and percent of footprint

Method	Threshold =1.0				Extracted Area = 3.72%			
	Extracted Area	Overlap to Δh	Best Accuracy	At % of footprint	Threshold	Overlap to Δh	Best Accuracy	At % of footprint
Δd	5.19%	80%	89%	24%	1.11	71%	89%	20%
Δw	7.57%	80%	89%	26%	1.23	71%	89%	16%
Δr	12.65%	100%	83%	40%	1.28	83%	89%	22%
Δh	3.72%	100%	89%	32%	1.00	100%	89%	32%
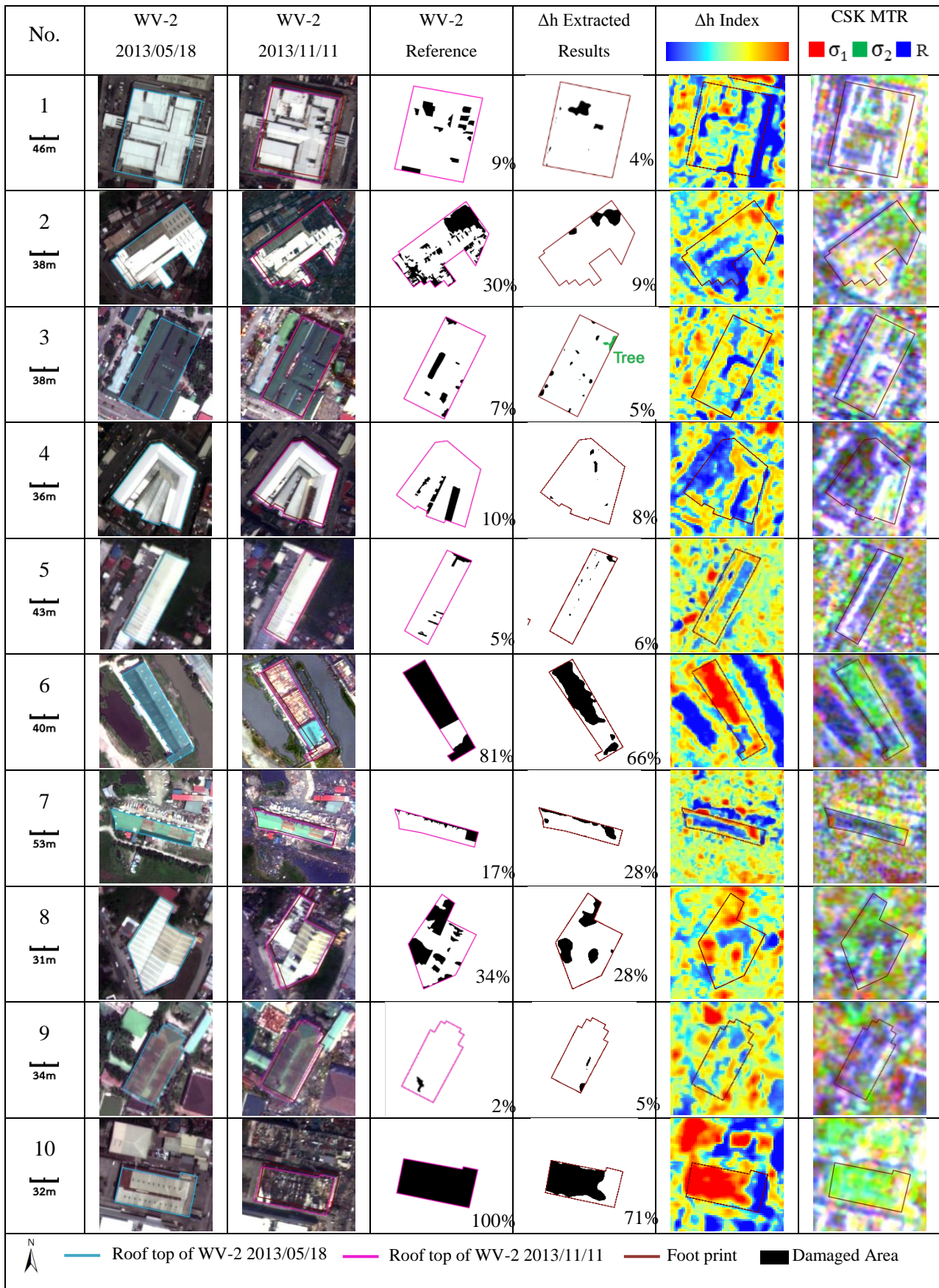
Figure 5-13. Comparison of the results obtained using the proposed damage extraction method and the reference damaged areas from the WV-2 images for the 10 largest buildings.

Table 5-3. Confusion matrix of Δh for the 2-class damage extraction from the CSM images.

		Visual inspection of WV-2 images			
		Minor & Moderate	Major	Total	User Accuracy
Δh from CSM	Minor & Moderate	393	48	441	0.89
	Major	12	92	104	0.88
	Total	405	140	545	
	Procedure Accuracy	0.97	0.66		0.89
Cohen's kappa for 2 Classes = 0.69					

Table 5-4. Confusion matrix of Δh for the 3-class damage extraction from the CSM images.

		Visual inspection of WV-2 images				
		Minor	Moderate	Major	Total	User Accuracy
Δh from CSM	Minor	236	144	41	421	0.56
	Moderate	6	7	7	20	0.35
	Major	5	7	92	104	0.88
	Total	247	158	140	545	
	Procedure Accuracy	0.96	0.04	0.66		0.61
Cohen's kappa for 3 Classes = 0.35						

In the case of Δh, the major damage class (32%) was identified with relatively good accuracy (user accuracy of 0.88, producer accuracy of 0.66) from the extracted results. At this point, a maximum overall accuracy of 0.89 and Cohen's kappa of 0.69 was returned in the confusion matrix shown in **Table 5-3**. It is also notable that the minor damage could not be distinguished from the moderate damage in the extracted results. In the case of separating moderate damage from minor damage with the criterion of 28%, the overall accuracy dropped to 0.61 and the Cohen's kappa to 0.35 in the confusion matrix shown in **Table 5-4**. Because the moderate damage class was proportionally lower than the others, with any percentage of roof damage being classified as moderate, we were unable to correctly extract the moderate damage class from the minor damage class. Therefore, the damage levels were grouped into only two classes by combining the minor and moderate damage classes.

In total, 140 buildings were classified as having sustained major damage. By using the proposed method, 104 buildings were extracted, and from those, the classification of 92 buildings (66%) was correctly estimated. There were 405 buildings in the minor-to-moderate damages class, and a total of 441 buildings were extracted, with 393 buildings (97%) correctly classified. Note that the damaged areas of the buildings detected using this method relied on the SAR and auxiliary vector data and that some pixels around the selected buildings were assigned to the damaged area. Some of those pixels were the damaged areas of other buildings and were not included in this study. However, some of the pixels were affected by changes in the environment, including flooded areas, broken trees, and debris. Those pixels should be classified as false alarms.

5.6. Conclusions

The devastation wrought by the 2013 typhoon Haiyan was investigated using a Multi-temporal Correlation (MTR) technique applied to two CSK images. A new change index was introduced, and of the several candidate methods, the proposed Hyperboloid Change Index (Δh) method, achieved the greatest building damage extraction accuracy (89%) when distinguishing moderate damage from minor damage. The proposed index was able to indicate, with lower noise, changes over a period. Its value was normalized and related to the standard deviation of the difference and the correlation between the pre- and post-event backscattering coefficients. For this event, the index was able to efficiently extract, given a proper threshold value, the severe damage to fish traps and large buildings. However, some limitations were observed, including an inability to handle small buildings and/or dense areas as well as relatively poor accuracy in distinguishing minor to moderate damage levels for large buildings. These limitations of the proposed technique are probably related to the spatial resolution and SAR observation scheme, so they cannot be avoided.

The proposed Hyperboloid Change Index has clear advantages with respect to other candidate methods because it can indicate a change in conjunction with the reflectance. The resulting change maps are clearer and easier to interpret than the maps produced using the other tested indices. The method is not only suitable for detecting damage to buildings, but it can also be used generally to differentiate levels of change. It is possible that further improvements can be made by adjusting the hyperboloid constants or the standard deviation coefficients, according to the specific case. This improvement, in addition to testing the influence of the window size, will be among the main issues considered in future research.

Chapter 6
General conclusions

This research aimed to provide more accurate data for natural disaster management, by developing a novel method which is suitable for the characteristic of disasters and SAR sensors. The general conclusions for the three most relevant chapters can be summarized as follows.

In section 3, by introducing the global threshold value of the entire study area for each RADARSAT-2 image, the weight-averaged neighborhood valley-emphasis method was able to extract flooded areas automatically from the backscattering coefficient. In this case, the HH + HV dual-polarization achieved a higher accuracy than the HH single-polarization for open water extraction, which is affected by winds and floating/submerged plants. SAR images also have limitations for observing water areas covered by trees or adjacent to buildings. The postponed method, using permanent water references to obtain threshold value for classifying water body, could improve speed for automatic flood detection in a specific area such as Chao Phraya river basin. The accuracy of flood area detection from RADARSAT-2 acquired in 2011 is around 70% when compare to the results obtained from GeoEye-1 and ThaiChote-1.

In chapter 4, the proposed method from chapter 3 had been reprocessing by RADARSAT-2 acquired in 2016. In this year, flood situation covered less area than 2011. The accuracy of flood area detection from RADARSAT-2 is around 90% when compare to the results obtained from Landsat 8. The higher accurate value may cause by the resolution of RADARSAT-2 SAR Scan Narrow beam mode is more similar to Landsat 8 than GeoEye-1.

In chapter 5, a new change index was introduced, and of the several candidate methods, the proposed Hyperboloid Change Index (Δh) method, achieved the greatest building damage extraction accuracy (89%) when distinguishing moderate damage from minor damage. However, some limitations were observed, including an inability to handle small buildings and/or dense areas as well as relatively poor accuracy in distinguishing minor to moderate damage levels for large buildings.

REFERENCES

CHAPTER 1

[1] Henderson, F. M.; Lewis, A. J. Introduction. In *Principles and applications of imaging radar. Manual of remote sensing*, 3rd ed., Volume 2, Henderson, F. M., Lewis, A. J., Eds.; Publisher: John Wiley & Sons, Inc. New York, USA, **1998**; Volume 2, pp. 1-6.

[2] Richards, J. A. In *Remote Sensing with Imaging Radar*, Publisher: Springer, New York, USA, **2009**, pp 11-49.

[3] Inoue, Y.; Sakaiya, E.; Wang, C. Potential of X-Band Images from High-Resolution Satellite SAR Sensors to Assess Growth and Yield in Paddy Rice Remote Sens. **2014**, 6, 5995-6019; DOI:10.3390/rs6075995.

[4] ESA earthnet online, RADAR and SAR Glossary. Available online: https://earth.esa.int/handbooks /asar/CNTR5-2.html (accessed on 7 December 5, 2016)

[5] Huang, S.Q.; You, H.; Wang, Y.T. Environmental monitoring of natural disasters using synthetic aperture radar image multidirectional characteristics. *Int J Remote Sens*. **2015**, 36, 2, 3460-3183, DOI: 10.1080/01431161.2015.1041171.

[6] Sharif, A. A. A.; Pradhan, B.; Hadi, S. J.; Mola, N. Revisiting Methods and Potentials of SAR Change Detection. Proceedings of the World Congress on Engineering 2013, Vol III, London, U.K., July 3-5, **2003**, ISBN: 978-988-19252-9-9.

CHAPTER 2

[1] Smith, A. B.; Katz, R. W. US billion-dollar weather and climate disasters: data sources, trends, accuracy and biases. *Nat Hazards*. **2013**, 67, 387-410, DOI: 10.1007/s11069-013-0566-5.

[2] CRED: Centre for Research on the Epidemiology of Disasters, EM-DAT the International Disaster Database. General Classification, Available online: http://www.emdat.be/classification (accessed on 3 January 2016)

[3] Shultz, J. M.; Shepherd, M.; Bagrodia, R.; Espinel, Z. Tropical cyclones in a year of rising global temperatures and a strengthening El Niño. *Disaster Health.* **2014**, 2:3-4, 151-162, DOI: 10.1080/21665044.2014.1111722.

[4] Elsner, J. B.; Liu, K. Examining the ENSO–typhoon hypothesis. *Clim Res*. **2003**, 25, 43-54.

[5] Mas, E.; Bricker, J.; Kure, S.; Adriano, B.; Yi, C.; Suppasri, A.; Koshimura, S. Field survey report and satellite image interpretation of the 2013 Super Typhoon Haiyan in the Philippines. Nat. Hazards Earth Syst. Sci., **2015**, 15, 805–816, DOI: 10.5194/nhess-15-805-2015.

[6] Oxford Advanced Learner's Dictionary, 8th edition (Oxford Advanced Learner's Dictionary).

[7] Revilla-Romero, B.; Hirpa, F.; Pozo, J. T.; Salamon, P.; Brakenridge, R.; Pappenberger, F.; Groeve, T. D. On the Use of Global Flood Forecasts and Satellite-Derived Inundation Maps for Flood Monitoring in Data-Sparse Regions. *Remote Sens.* **2015**, 7, 15702-15728; doi:10.3390/rs71115702.

[8] The Risk of Hazard, Three common types of flood explained, Intermap, Available online: http://www.intermap.com/risks-of-hazard-blog/three-common-types-of-flood-explained (accessed on 3 January 2017)

[9] Brakenridge, G.R. Global Active Archive of Large Flood Events, Dartmouth Flood Observatory, University of Colorado Available online: http://floodobservatory.colorado.edu/ Archives/index.html (accessed on 3 January 2017)

[10] RADARSAT Constellation, Canadian Space Agency Available online: http://www.asc-csa.gc.ca/eng/satellites/radarsat/ (accessed on 3 January 2017)

[11] Satellite Characteristics, Canadian Space Agency (CSA). Available online: http://www.asc-csa.gc.ca/eng/satellites/radarsat/radarsat-tableau.asp (accessed on 3 January 2017).

[12] MacDonald, Dettwiler and Associates Ltd. (MDA). RADARSAT-2 Product Description. Publisher: MDA, Richmond, B.C., Canada, 2016, Issue 1/13, 91 pages. http://mdacorporation.com/docs/default-source/technical-documents/geospatial-services/52-1238_rs2_product_description.pdf?sfvrsn=10 (accessed on 3 January 2017).

[13] MDA's Geospatial Services (MDA) RADARSAT-1 Data Products Specifications, Publisher: MDA, Canada, **2004**. Available online : http://mdacorporation.com/docs/default-source/product-spec-sheets/ geospatial-services/r1_prod_spec.pdf?sfvrsn=6 (accessed on 3 January 2017).

[14] The Earth Observation and Geo-Spatial Information (e-GEOS). Cosmo-Skymed Image Calibration. Available online: http://www.e-geos.it/products/pdf/COSMO-SkyMed-Image_ Calibration.pdf (accessed on 29 June 2015).

[15] Nezry, E. Adaptive Speckle Filtering in Radar Imagery, In *Land Applications of Radar Remote Sensing*; Holecz, F.; Pasquali, Paolo, P.; Milisavljevic, N.; Closson, D.; Eds.; Publisher: InTech, Croatia, 2014; pp.1-55.

[16] Yommy, A. S.; Liu, R.; Wu, S. SAR Image Despeckling using Refined Lee Filter, International Conference on Intelligent Human-Machine Systems and Cybernetics. Hangzhou, China, 2015, 6 pages, DOI 10.1109/IHMSC.2015.236.

[17] Orthorectification Tutorial, Terrain Correction, Next ESA SAR Toolbox (NEST). Available online: http://corp.array.ca/nest-web/help/tutorials/terrain_correction.html (accessed on 3 January 2017).

[18] SRTM 90m Digital Elevation Database v4.1, CGIAR CSI. Available online: http://www.cgiar-csi.org/data/srtm-90m-digital-elevation-database-v4-1 (accessed on 3 January 2017).

[19] Li Z.; Bethel, J. Image Coregistration in Sar Interferometry. The International Archives of the Photogrammetry, Remote Sensing and Spatial Information Sciences. Vol. XXXVII. Part B1. Beijing 2008, 6 pages.

CHAPTER 3

[1]   AON Benfield. 2011 *Thailand Floods Event Recap Report, Impact Forecasting;* Impact Forecasting LLC: Chicago, IL, USA, 2012; p. 40. Available online: http://thoughtleadership.aonbenfield. com/Documents/20120314_impact_forecasting_thailand_flood_event_recap.pdf (accessed on 31 October 2016).

[2]   The World Bank. *Thai Flood 2011 Rapid Assessment for Resilient Recovery and Reconstruction Planning;* The World Bank: Nonthaburi, Thailand, 2012; Volume 2, p. 377. Available online: http://documents.worldbank.org/curated/en/262141468118140200/pdf/698220WP0v20P10se0Only060 Box370022B.pdf (accessed on 31 October 2016).

[3]   Japan International Cooperation Agency (JICA). *Project for the Comprehensive Flood Management Plan for the Chao Phraya River Basin, Final Report: Main Report;* JICA: Tokyo, Japan, 2012; Volume 2, p. 219. Available online: http://open_jicareport.jica.go.jp/pdf/12127213_01.pdf (accessed on 31 October 2016).

[4]   Henderson, F.M.; Lewis, A.J. Introduction. In *Principles and Applications of Imaging Radar. Manual of Remote Sensing,* 3rd ed.; Henderson, F.M., Lewis, A.J., Eds.; John Wiley & Sons, Inc.: New York, NY, USA, 1998; Volume 2, pp. 1-6.

[5]   Rakwatin, P.; Sansena T.; Marjang N.; Rungsipanich, A. Using multi-temporal remote-sensing data to estimate 2011 flood area and volume over Chao Phraya River Basin, Thailand. *Remote Sens. Lett.* **2013**, 4, 243-250, doi:10.1080/2150704X.2012.723833.

[6]   Auynirundronkool, K.; Chen, N.; Peng, C.; Yang, C.; Gong, J.; Silapathong, C. Flood detection and mapping of the Thailand Central Plain using RADARSAT and MODIS under a sensor web environment. *Int. J. Appl. Earth Obs. Geoinf.* **2012**, 14, 245-255, doi:10.1016/j.jag.2011.09.017.

[7]   Pierdicca, N.; Chini, M.; Pulvirenti, L.; Macina, F. Integrating physical and topographic information into a fuzzy scheme to map flooded area by SAR. *Sensors.* **2008**, 8, 4151-4164, doi:10.3390/s8074151.

[8]   Pierdicca, N.; Pulvirenti, L.; Chini, M.; Guerriero, L.; Candela, L. Observing floods from space: Experience gained from COSMO-SkyMed observations. *Acta Astronaut.* **2013**, 84, 122-133, doi:10.1016/j.actaastro.2012.10.034.

[9]   Brisco, B.; Short, N.; van der Sanden, J.; Landry, R.; Raymond, D. A semi-automated tool for surface water mapping with RADARSAT-1. Can. J. *Remote Sens.* **2009**, 35, 336-344.

[10] Bolanos, S.; Stiff, D.; Brisco, B.; Pietroniro, A. Operational surface water detection and monitoring using Radarsat 2. *Remote Sens.* **2016**, 8, 285, doi:10.3390/rs8040285.

[11] Lee, J.; Grunes, M.R.; Pottier, E. Quantitative comparison of classification capability: Fully polarimetric versus dual and single-polarization SAR. *IEEE Trans. Geosci. Remote Sens.* **2001**, 39, 2343-2351.

[12] Kim, S.-B.; Ouelette, J.D.; Zyl, J.; Johnson, J.T. Detection of inland open water surfaces using dual polarization L-band radar for the soil moisture active passive mission. *IEEE Trans. Geosci. Remote Sens.* **2016**, 54, 3388-3399, doi:10.1109/TGRS.2016.2517010.

[13] Martinis, S.; Rieke, C. Backscatter analysis using multi-temporal and multi-frequency SAR data in the context of flood mapping at River Saale, Germany. *Remote Sens.* **2015**, 7, 7732-7752, doi:10.3390/rs70607732.

[14] Sang, H.; Zhang, J.; Lin, H.; Zhai, L. Multi-polarization ASAR backscattering from Herbaceous Wetlands in Poyang Lake Region, China. *Remote Sens.* **2014**, 6, 4621-4646, doi:10.3390/rs6054621.

[15] White, L.; Brisco, B.; Pregitzer, M.; Tedford, B.; Boychuk, L. RADARSAT-2 beam mode selection for surface water and flooded vegetation mapping. Can. J. *Remote Sens.* **2014**, 40, 135-151, doi:10.1080/07038992.2014.943393.

[16] Zakhvatkina, N.; Korosov, A.; Muckenhuber, S.; Sandven, S.; Babiker, M. Operational algorithm for ice/water classification on dual-polarized RADARSAT-2 images. *The Cryosphere Discuss.* **2017**, 11, 33-46, doi: 10.5194/tc-11-33-2017.

[17] Fan, J.; Lei, B. A modified valley-emphasis method for automatic thresholding. *Pattern Recogn. Lett.* **2012**, 33, 703-708, doi:10.1016/j.patrec.2011.12.009.

[18] Al-Bayanti, M.; El-Zaart, A. Automatic thresholding techniques for SAR images. In Proceedings of the International Conference of Soft Computing, Dubai, United Arab Emirates, 2-3 November 2013; doi:10.5121/csit.2013.3308.

[19] Martinis, S.; Twele, A.; Voigt, S. Towards operational near-real time flood detection using a split-based automatic thresholding procedure on high resolution TerraSAR-X data. *Nat. Hazards Earth Syst. Sci.* **2009**, 9, 303-314.

[20] Martinis, S.; Kersten, J.; Twele, A. A fully automated TerraSAR-X based flood service. *ISPRS Int. J. Photogramm. Remote Sens.* **2015**, 104, 203-212, doi:10.1016/j.isprsjprs.2014.07.014.

[21] Martinis, S.; Twele, A.; Strobl, C.; Kersten, J.; Stein, E. A Multi-scale flood monitoring system based on fully automatic MODIS and TerraSAR-X processing chains. *Remote Sens.* **2013**, 104, 203-212, doi:10.3390/rs5115598.

[22] Hostanche, R.; Matgen, P.; Schumann, G.; Puech, C.; Hoffmann, L.; Pfister, L. Water level estimation and reduction of hydraulic model calibration uncertainties using satellite SAR images of floods. *IEEE Trans. Geosci. Remote Sens.* **2009**, 47, 882-894, doi:10.1109/TGRS.2008.2008718.

[23] Manjusree, P.; Kumar, L.P.; Bhatt, C.M.; Rao, G.S.; Bhanumurthy, V. Optimization of threshold ranges for rapid flood inundation mapping by evaluating backscatter profiles of high incidence angle SAR Images. *Int. J. Disaster Risk Sci.* **2012**, 3, 113-122, doi:10.1007/s13753-012-0011-5.

[24] Long, S.; Fatoyinbo, T.E.; Policelli, F. Flood extent mapping for Namibia using change detection and thresholding with SAR. *Int. J. Environ. Res. Lett.* **2012**, doi:10.1088/1748-9326/9/3/035002.

[25] Mason, D.C.; Speck, R.; Devereux, B.; Schumann, G. J.-P.; Neal, J.C.; Bates, P.D. Flood detection in urban areas using TerraSAR-X. *IEEE Trans. Geosci. Remote Sens.* **2010**, 48, 882-894, doi:10.1109/TGRS.2011.2178030.

[26] Pulvirenti, L.; Chini, M.; Pierdicca, N.; Guerriero, L.; Ferrazzoli, P. Flood monitoring using multi-temporal COSMO-SkyMed data: Image segmentation and signature interpretation. *Remote Sens. Environ.* **2011**, 115, 990-1002, doi:10.1016/j.rse.2010.12.002.

[27] Mason, D.C.; Davenport, I.J.; Neal, C.N.; Schumann, J.-P.; Bates, P.D. Near real-time flood detection in urban and rural areas using high-resolution synthetic aperture radar images. *IEEE Trans. Geosci. Remote Sens.* **2012**, 50, 3041-3052, doi:10.1109/TGRS.2011.2178030.

[28] Evans, T.L.; Costa, M.; Telmer, K.; Silva, T.S.F. Using ALOS/PALSAR and RADARSAT-2 to map land cover and seasonal inundation in the Brazilian Pantanal. IEEE J. Sel. Topics Appl. *Earth Obs. Remote Sens.* **2010**, 3, 560-575, doi:10.1109/JSTARS.2010.2089042.

[29] Matgen, P.; Hostache, R.; Schumann, G.; Pfister, L.; Hoffmann, L.; Savenije, H.H.G. Towards an automated SAR-based flood monitoring system: Lessons learned from two case studies. *Phys. Chem. Earth.* **2011**, 36, 241-252, doi:10.1016/j.pce.2010.12.009.

[30] Pulvirenti, L.; Pierdicca, N.; Boni, G.; Fiorini, M.; Rudari, R. Flood damage assessment through multitemporal COSMO-SkyMed data and hydrodynamic models: The Albania 2010 case study. IEEE J. Sel. Topics Appl. Earth Observ. *Remote Sens.* **2014**, 7, 2848-2855.

[31] Sezgin, M.; Sankur, B. Survey over image thresholding techniques and quantitative performance evaluation. J. Electron. Imaging **2004**, 13, 146-165, doi:10.1117/1.1631315.

[32] MDA's Geospatial Services (MDA). RADARSAT-1 Data Products Specifications; MDA: British Columbia, Canada, 2004. Available online: http://mdacorporation.com/docs/default-source/product-spec-sheets/geospatial-services/r1_prod_spec.pdf?sfvrsn=6 (accessed on 31 October 2016).

[33] Vala, H.; Baxi, A. A Review on Otsu image segmentation algorithm. *Int. J. Adv. Res. Comput. Eng. Tech.* **2013**, 2, 387-389.

[34] Lee, J.S. Digital image enhancement and noise filtering by use of local statistics. *IEEE Trans. Pattern Anal. Mach. Intell.* **1980**, 2, 165-168.

[35] Lee, J.S. Refined filtering of image noise using local statistics. *Comput. Graph. Image Process.* **1981**, 15, 380-389.

[36] McFeeters, S.K. Using the Normalized Difference Water Index (NDWI) within a geographic information system to detect swimming pools for mosquito abatement: A practical approach. *Remote Sens.* **2013**, 5, 3544-3561, doi:10.3390/rs5073544.

[37] McFeeters, S.K. The use of the Normalized Difference Water Index (NDWI) in the delineation of open water features. *Int. J. Remote Sens.* **1996**, 17, 1425-1432.

[38] Runoff Data, Hydrology and Water Management Center for Central Region, Royal Irrigation Department (RID). Available online: http://hydro-5.com/index_.php?id=4 (accessed on 31 October 2016).

[39] Flood Situation Update: Water Level Report 2011; Rojana Industrial Park Public Co., Ltd.: Bangkok, Thailand, 2011. Available online: http://rojna.listedcompany.com/flood_situation.html (accessed on 31 October 2016).

[40] Pulvirenti, L.; Chini, M.; Pierdicca, N.; Boni, G. Use of SAR Data for detecting floodwater in urban and agricultural areas: The role of the interferometric coherence. *IEEE Trans. Geosci. Remote Sens.* **2016**, 54, 1532-1544, doi:10.1109/TGRS.2015.2482001.

CHAPTER 4

[1] Thailand Flood Monitoring System, Geo-Informatics and Space Technology Development Agency, Bangkok, Thailand. Available online: http://flood.gistda.or.th (accessed on 31 January 2017).

[2] Gao, B. NDWI—A Normalized Difference Water Index for Remote Sensing of Vegetation Liquid Water From Space. Remote Sens. Environ. **1996**, 58, 257-266, PII: S0034-4257(96)00067-3.

[3] McFeeters, S.K. The use of the Normalized Difference Water Index (NDWI) in the delineation of open water features. *Int. J. Remote Sens.* **1996**, 17, 1425-1432.

CHAPTER 5

[1] Adragna, F.; Nicolas, J. Interferometry. In *Processing of Synthetic Aperture Radar Images*; Maitre, H., Ed.; John Wiley & Sons: ISTE Ltd : London, UK, 2008; pp. 279-300.

[2] Engdahl, M.E.; Hyyppa, J.M. Land-Cover Classification Using Multitemporal ERS-1/2 InSAR Data. *IEEE Trans. Geosci. Remote Sens.* **2003**, 41,

[3] Bruzzone, L.; Wiesmann, A. An Advanced System for the Automatic Classification of Multitemporal SAR Images. *IEEE Trans. Geosci. Remote Sens.* **2004**, 42, 1321-1333.

[4] Xu, L.; Li, S.; Deng, Y.; Wang, R. Unsupervised classification of polarimetric synthetic aperture radar interferometry using polarimetric interferometric similarity parameters and SPAN. *IET Radar Sonar Navig.* **2014**, 8, pp 1135-1144.

[5] Mishra, P.; Singh, D. A Statistical-Measure-Based Adaptive Land Cover Classification Algorithm by Efficient Utilization of Polarimetric SAR Observables. *IEEE Trans. Geosci. Remote Sens.* **2014**, 52, 2889-2900.

[6] Liu, J.G.; Black, A.; Lee, H.; Hanaizumi, H.; Moore, J. Land surface change detection in a desert area in Algeria using multi-temporal ERS SAR coherence images. *International Journal of Remote Sensing* **2001**, 22, 2463-2477.

[7] Refice, A.; Capolongo, D.; Pasquariello, G.; D'Addabbo, A.; Bovenga, F.; Nutricato, R.; Lovergine, F.P.; Pietranera, L. SAR and InSAR for Flood Monitoring: Examples With COSMO-SkyMed Data. *IEEE J. Sel. Top. Appl. Earth Obs. Remote Sens.* **2014**. 6, 2711-2722.

[8] Amitrano, D.; Di Martino, G.; Iodice, A.; Riccio D.; Ruello G. A New Framework for SAR Multitemporal Data RGB Representation: Rationale and Products. *IEEE Trans. Geosci. Remote Sens.* **2015**, 1, 117-133.

[9] Preiss, M.; Gray, D. A.; Stacy, N. J.S. Detecting Scene Changes Using Synthetic Aperture Radar Interferometry. *IEEE Trans. Geosci. Remote Sens.* **2006**, 44, 2041-2054.

[10] Xiong, B,; Chen, J.M.; Kuang, G. A change detection measure based on a likelihood ratio and statistical properties of SAR intensity images. *Remote Sensing Letters* **2012**, 3, 267-275.

[11] Bouaraba, A.; Younsi, A.; Belhadj-Aissa, A.; Acheroy, M.; Milisavljevic, N.; Closson, D. Robust Techniques For Coherent Change Detection Using Cosmo-Skymed Sar Images. *Progress In Electromagnetics Research M* **2012**, 22, 219-232.

[12] Rignot, E.J. M.; van Zyl, J. Change Detection Techniques for ERS-1 SAR Data. *IEEE Trans. Geosci. Remote Sens.* 1993, 31, 896-906.

[13] Liu, W.; Yamazaki, F.; Gokon, H.; Koshimura, S. Extraction of Tsunami-Flooded Areas and Damaged Buildings in the 2011 Tohoku-Oki Earthquake from TerraSAR-X Intensity Images. *Earthquake Spectra* **2013**, 29, S1, S183-S200.

[14] Stramondo, S.; Bignami, C.; Chini, M.; Pierdicca, N.; Tertulliani, A. Satellite radar and optical remote sensing for earthquake damage detection: Results from different case studies. *Int. J. Remote Sens.* **2006**, 27, 4433–4447.

[15] Yonezawa, C.; Takeuchi, S. Decorrelation of SAR data by urban damages caused by the 1995 Hyogoken-nanbu earthquake. *Int. J. Remote Sens.* 2001, 22, 1585–1600.

[16] Takeuchi, S.; Suga, Y.; Yonezawa, C.; Chen, A.J. Detection of Urban Disaster Using InSAR—A Case Study for the 1999 Great Taiwan Earthquake. In Proceedings of the IEEE IGARSS, Honolulu, HI, USA, 24–28 July 2000; pp. 339–341.

[17] Suga, Y.; Takeuchi, S.; Oguro, Y.; Chen, A.J.; Ogawa, M.; Konishi, T.; Yonezawa, C. Application of ERS-2/SAR data for the 1999 Taiwan earthquake. Adv. Space Res. 2001, 28, 155–163.

[18] Matsuoka, M.; Yamazaki, F. Characteristics of Satellite SAR Images in the Areas Damaged by Earthquakes. In Proceedings of the IEEE IGARSS, Honolulu, HI, USA, 24–28 July 2000; pp. 2693–2696.

[19] Brunner, D.; Lemoine, G.; Bruzzone, L. Earthquake Damage Assessment of Buildings Using VHR Optical and *SAR* Imagery. *IEEE Trans. Geosci. Remote Sens* **2010**, 48, 2403-2419.

[20] National Disaster Risk Reduction and Management Council, Republic of the Philippines. NDRRMC Update: Updates re Effects of Typhoon Yolanda (Haiyan), 17 April 2014. Available online: http://www.ndrrmc.gov.ph/attachments/article/1329/Update_on_Effects_Typhoon_YOLANDA_ (Haiyan)_17APR2014.pdf (access on 29 June 2015)

[21] Lagmay, A.M.F.; Agaton, R.P.; Bahala, M.A. C.; Briones J.B.L.T.; Cabacaba K.M.C.; Caro C.V. C.; Dasallas L.L.; Gonzalo, L.A.L.; Ladiero, C.N.; Lapidez, J.P.; et al. Devastating storm surges of Typhoon Haiyan. *International Journal of Disaster Risk Reduction* **2015**, 11, 1-12.

[22] Covello, F.; Battaza, F.; Coletta, A.; Lopinto E.; Fiorentino, C.; Pietranera, L.; Valentini, G.; Zoffoli, S. COSMO-SkyMed an existing opportunity for observing the Earth. *Journal of Geodynamics* **2010**, 49, 171-180.

[23] The Earth Observation and Geo-Spatial Information (e-GEOS). Cosmo-Skymed Image Calibration. http://www.e-geos.it/products/pdf/COSMO-SkyMed-Image_Calibration.pdf (access on 29 June 2015)

[24] Parrilli, S.; Poderico, M.; Angelino, C. V.; Verdoliva, L. A Nonlocal SAR Image Denoising Algorithm Based on LLMMSE Wavelet Shrinkage. *IEEE Trans. Geosci. Remote Sens*. **2012**, 50(2), 606–616.

[25] Born, M.; Wolf, E. *Principles of Optics: Electromagnetic Theory of Propagation, Interference and Diffraction of Ligh*, 4th ed.; Pergamon Press: London, England, 1970; pp. 191-554.

[26] Ferretti, A.; Monti-Guarnieri, A.; Prati, C.; Rocca; F. Part C InSAR processing: a mathematical approach. In *InSAR Principles: Guidelines for SAR Interferometry Processing and Interpretation*; Fletcher K., Ed.; ESA Publications: Noordwijk, Netherlands, 2007; pp. 3-13.

[27] Cigna, F.; Tapete, D.; Lasaponara, R.; Masini, N. Amplitude change detection with Envisat ASAR to image the cultural landscape of the Nasca region, Peru. Archaeol. Prospect. 2013, 20, 117–131.

[28] Tapete, D., Cigna, F., Masini, N. and Lasaponara, R. (2013), Prospection and Monitoring of the Archaeological Heritage of Nasca, Peru, with ENVISAT ASAR. Archaeol. Prospect., 20: 133–147. doi: 10.1002/arp. 1449.

[29] Aiazzi, B.; Alparone, L.; Baronti, S.; Garzelli, A. Coherence Estimation From Multilook Incoherent SAR Imagery. *IEEE Trans. Geosci. Remote Sens*. **2003**, 41, 2531-2539.

[30] Chang, Z.; Gong, H.; Zhang, J.; Chen, M. Correlation Analysis on Interferometric Coherence Degree and Probability of Residue Occurrence in Interferogram. *IEEE Sensors J.* **2014**, 14, 2369-2375.

[31] Onana, V.; Trouvé, E.; Mauris, G.; Rudant, J.; Tonyé, E. Linear Features Extraction in Rain Forest Context From Interferometric SAR Images by Fusion of Coherence and Amplitude Information.

[32] Arciniegas, G. A.; Bijker, W.; Kerle, N.; Tolpekin, V. A. Coherence- and Amplitude-Based Analysis of Seismogenic Damage in Bam, Iran, Using ENVISAT ASAR Data. *IEEE Trans. Geosci. Remote Sens*. **2007**, 45, 1571-1581.

[33] Conesa, F. C.; Devanthéry, N.; Balbo, A. L.; Madella, Marco.; Monserrat, O. Use of Satellite SAR for Understanding Long-Term Human Occupation Dynamics in the Monsoonal Semi-Arid Plains of North Gujarat, India. Remote Sens. **2014**, 6(11), 11420-11443.

[34] Kerle, N.; Hoffman, R.R. Collaborative damage mapping for emergency response: the role of Cognitive Systems Engineering. *Nat. Hazards Earth Syst. Sci*. **2013**, 13 (1), 97-113.

[35] Dong, L. G.; Shan, J. A comprehensive review of earthquake-induced building damage detection with remote sensing techniques. *ISPRS J. Photogramm. Remote Sens.* **2013**, 84, 85-99.

[36] Mas, E.; Bricker, J.; Kure, S.; Adriano, B.; Yi, C.; Suppasri, A.; Koshimura S. Field survey report and satellite image interpretation of the 2013 Super Typhoon Haiyan in the Philippines. *Nat. Hazards Earth Syst. Sci.* **2015**, 15, 805–816.

[37] Dell'Acqua, F.; Gamba, P. Remote sensing and earthquake damage assessment: Experiences, limits, and perspectives. Proceedings of the IEEE. **2012**, 100 (10), 2876-2890.

[38] Chini, M.; Piscini, A.; Cinti, F.R.; Amici, S.; Nappi, R.; de Martini, P.M. The 2011 Tohoku (Japan) Tsunami inundation and liquefaction investigated through optical, thermal, and SAR data. *IEEE Geosci. Remote Sens. Lett*. 2013, 10, 347–351.

APPENDICES

APPENDIX A

The Beaufort scale	1-minute sustained winds	10-minute sustained winds	NE Pacific & N Atlantic NHC/CPHC[1]	NW Pacific JTWC[2]	NW Pacific JMA[3]	N Indian Ocean IMD[4]	SW Indian Ocean MF[5]	Australia & S Pacific BOM/FMS[6]
0–7	<32 knots (37 mph; 59 km/h)	<28 knots (32 mph; 52 km/h)	Tropical Depression	Tropical Depression	Tropical Depression	Depression	Zone of Disturbed Weather	Tropical Disturbance Tropical Depression Tropical Low
7	33 knots (38 mph; 61 km/h)	28–29 knots (32–33 mph; 52–54 km/h)	Tropical Depression	Tropical Depression	Tropical Depression	Deep Depression	Tropical Disturbance	Tropical Disturbance Tropical Depression Tropical Low
8	34–37 knots (39–43 mph; 63–69 km/h)	30–33 knots (35–38 mph; 56–61 km/h)	Tropical Storm	Tropical Storm	Tropical Depression	Deep Depression	Tropical Depression	Tropical Disturbance Tropical Depression Tropical Low
9–10	38–54 knots (44–62 mph; 70–100 km/h)	34–47 knots (39–54 mph; 63–87 km/h)	Tropical Storm	Tropical Storm	Tropical Storm	Cyclonic Storm	Moderate Tropical Storm	Category 1 tropical cyclone
11	55–63 knots (63–72 mph; 102–117 km/h)	48–55 knots (55–63 mph; 89–102 km/h)	Tropical Storm	Tropical Storm	Severe Tropical Storm	Severe Cyclonic Storm	Severe Tropical Storm	Category 2 tropical cyclone
12+	64–71 knots (74–82 mph; 119–131 km/h)	56–63 knots (64–72 mph; 104–117 km/h)	Category 1 hurricane	Typhoon	Typhoon	Very Severe Cyclonic Storm	Tropical Cyclone	Category 3 severe tropical cyclone
	72–82 knots (83–94 mph; 133–152 km/h)	64–72 knots (74–83 mph; 119–133 km/h)	Category 1 hurricane	Typhoon	Typhoon	Very Severe Cyclonic Storm	Tropical Cyclone	Category 3 severe tropical cyclone
	83–95 knots (96–109 mph; 154–176 km/h)	73–83 knots (84–96 mph; 135–154 km/h)	Category 2 hurricane	Typhoon	Typhoon	Very Severe Cyclonic Storm	Tropical Cyclone	Category 3 severe tropical cyclone
	96–97 knots (110–112 mph; 178–180 km/h)	84–85 knots (97–98 mph; 156–157 km/h)	Category 3 major hurricane	Typhoon	Typhoon	Very Severe Cyclonic Storm	Tropical Cyclone	Category 3 severe tropical cyclone
	98–112 knots (113–129 mph; 181–207 km/h)	86–98 knots (99–113 mph; 159–181 km/h)	Category 3 major hurricane	Typhoon	Typhoon	Very Severe Cyclonic Storm	Tropical Cyclone	Category 3 severe tropical cyclone
	113–122 knots (130–140 mph; 209–226 km/h)	99–107 knots (114–123 mph; 183–198 km/h)	Category 4 major hurricane	Typhoon	Typhoon	Extremely Severe Cyclonic Storm	Intense Tropical Cyclone	Category 4 severe tropical cyclone
	123–129 knots (142–148 mph; 228–239 km/h)	108–113 knots (124–130 mph; 200–209 km/h)	Category 4 major hurricane	Typhoon	Typhoon	Extremely Severe Cyclonic Storm	Intense Tropical Cyclone	Category 4 severe tropical cyclone
	130–136 knots (150–157 mph; 241–252 km/h)	114–119 knots (131–137 mph; 211–220 km/h)	Category 4 major hurricane	Super Typhoon	Typhoon	Super Cyclonic Storm	Very Intense Tropical Cyclone	Category 5 severe tropical cyclone
	>137 knots (158 mph; 254 km/h)	>120 knots (140 mph; 220 km/h)	Category 5 major hurricane	Super Typhoon	Typhoon	Super Cyclonic Storm	Very Intense Tropical Cyclone	Category 5 severe tropical cyclone

(1) The United States National Hurricane Center (NHC/RSMC Miami)/The United States Central Pacific Hurricane Center (CPHC/RSMC Honolulu)

(2) The Joint Typhoon Warning Center (JTWC)

(3) The Japan Meteorological Agency (JMA/RSMC Tokyo)

(4) The India Meteorological Department (IMD/RSMC New Delhi)

(5) Météo-France La Reunion (MFR/RSMC La Reunion)

(6) The Bureau of Meteorology (BOM)/The Fiji Meteorological Service (FMS)

Figure A-1. Tropical cyclone classifications

Source: http://www.wmo.int/pages/prog/www/tcp/Advisories-RSMCs.html

BEAM MODE	PRODUCT [1,2]	Nominal Pixel Spacing [3,4] [Rng × Az] (m)	Nominal Resolution [5] [Rng x Az] (m)	Nominal Scene Size [6] [Rng x Az] (km)	Nominal Incidence Angle Range [deg]	No. Looks [Rng x Az]	Polarization Options	BAQ Level (bits)
Spotlight	SLC	1.3 x 0.4	1.6 x 0.8	18 x 8	20 to 54 [7]	1 x 1	Single Co or Cross (HH or VV or HV or VH)	3
	SGX	1 or 0.8 x 1/3	4.6 – 2.0 x 0.8					
	SGF	0.5 x 0.5						
	SSG, SPG	0.5 x 0.5						
Ultra-Fine	SLC	1.3 x 2.1	1.6 x 2.8	20 x 20	20 to 54 [7]	1 x 1	Single Co or Cross (HH or VV or HV or VH)	3
	SGX	1 x 1 or 0.8 x 0.8	4.6 – 2.0 x 2.8					
	SGF	1.56 x 1.56						
	SSG, SPG	1.56 x 1.56						
Wide Ultra-Fine	SLC	1.3 x 2.1	1.6 x 2.8	50 x 50	29 to 50	1 x 1	Single Co or Cross (HH or VV or HV or VH)	2
	SGX	1 x 1	3.3 – 2.1 x 2.8					
	SGF	1.56 x 1.56						
	SSG, SPG	1.56 x 1.56						
Multi-Look Fine	SLC	2.7 x 2.9	3.1 x 4.6	50 x 50	30 to 50	1 x 1	Single Co or Cross (HH or VV or HV or VH)	3
	SGX	3.13 x 3.13	10.4 – 6.8 x 7.6			2 x 2		
	SGF	6.25 x 6.25						
	SSG, SPG	6.25 x 6.25						
Wide Multi-Look Fine	SLC	2.7 x 2.9	3.1 x 4.6	90 x 50	29 to 50	1 x 1	Single Co or Cross (HH or VV or HV or VH)	2
	SGX	3.13 x 3.13	10.8 – 6.8 x 7.6			2 x 2		
	SGF	6.25 x 6.25						
	SSG, SPG	6.25 x 6.25						
Extra-Fine	SLC (Full Res)	2.7 x 2.9	3.1 x 4.6	125 x 125	22 to 49	1 x 1	Single Co or Cross (HH or VV or HV or VH)	2
	SLC (Fine Res)	4.3 x 5.8	5.2 x 7.6					
	SLC (Std Res)	7.1 x 5.8	8.9 x 7.6					
	SLC (Wide Res)	10.6 x 5.8	13.3 x 7.6					
	SGX (1 look)	2.0 x 2.0	8.4 – 4.1 x 4.6			1 x 1		
	SGX (4 looks)	3.13 x 3.13	14 – 6.9 x 7.6			2 x 2		
	SGX (28 looks)	5.0 x 5.0	24 – 12 x 23.5			4 x 7		
	SGF (1 look)	3.13 x 3.13	8.4 – 4.1 x 4.6			1 x 1		
	SGF (4 looks)	6.25 x 6.25	14 – 6.9 x 7.6			2 x 2		
	SGF (28 looks)	8.0 x 8.0	24 – 12 x 23.5			4 x 7		
	SSG, SPG	3.13 x 3.13	8.4 – 4.1 x 4.6			1 x 1		
Fine	SLC	4.7 x 5.1	5.2 x 7.7	50 x 50	30 to 50	1 x 1	Single Co or Cross (HH or VV or HV or VH) or Dual (HH+HV or VV+VH)	3
	SGX	3.13 x 3.13	10.4 – 6.8 x 7.7					
	SGF	6.25 x 6.25						
	SSG, SPG	6.25 x 6.25						
Wide Fine	SLC	4.7 x 5.1	5.2 x 7.7	150 x 150	20 to 45	1 x 1	Single Co or Cross (HH or VV or HV or VH) or Dual (HH+HV or VV+VH)	3
	SGX	3.13 x 3.13	14.9 – 7.3 x 7.7					
	SGF	6.25 x 6.25						
	SSG, SPG	6.25 x 6.25						
Standard	SLC	8 or 11.8 x 5.1	9.0 or 13.5 x 7.7	100 x 100	20 to 52	1 x 1	Single Co or Cross (HH or VV or HV or VH) or Dual (HH+HV or VV+VH)	3
	SGX	8 x 8	26.8 – 17.3 x 24.7			1 x 4		
	SGF	12.5 x 12.5						
	SSG, SPG	12.5 x 12.5						
Wide	SLC	11.8 x 5.1	13.5 x 7.7	150 x 150	20 to 45	1 x 1	Single Co or Cross (HH or VV or HV or VH) or Dual (HH+HV or VV+VH)	3
	SGX	10 x 10	40.0 – 19.2 x 24.7			1 x 4		
	SGF	12.5 x 12.5						
	SSG, SPG	12.5 x 12.5						

Figure A-2. Summary of RADARSAT-2 beam mode and product characteristics
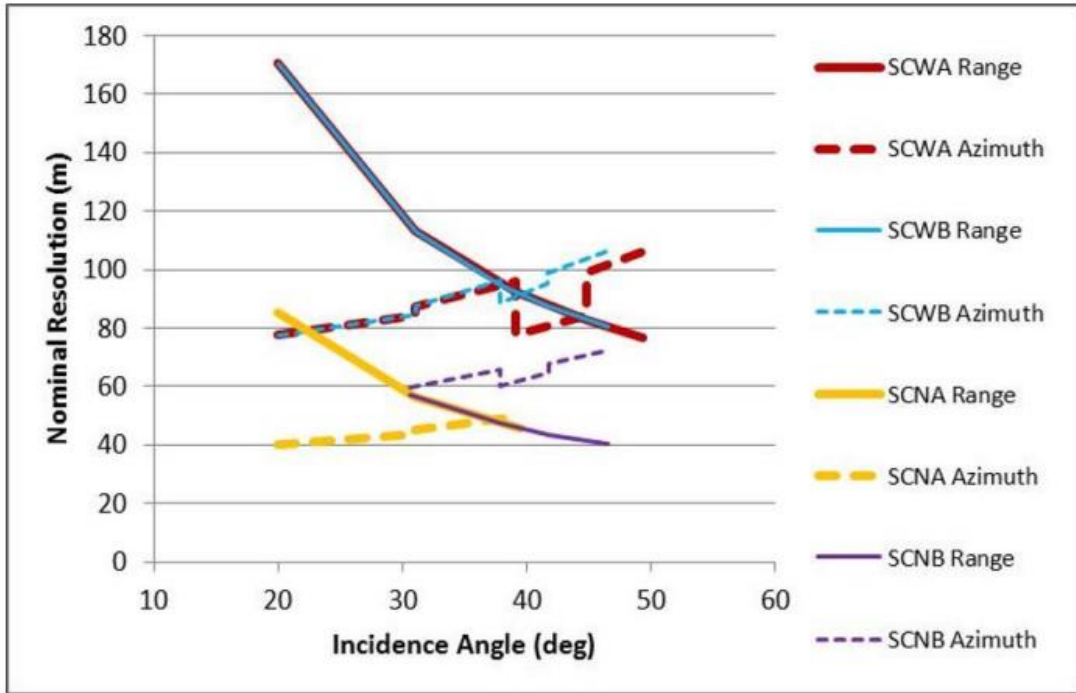
Source: RADARSAT-2 Product Description, 2016

BEAM MODE	PRODUCT [1,2]	Nominal Pixel Spacing [3,4] [Rng × Az] (m)	Nominal Resolution [5] [Rng x Az] (m)	Nominal Scene Size [6] [Rng x Az] (km)	Nominal Incidence Angle Range [deg]	No. Looks [Rng x Az]	Polarization Options	BAQ Level (bits)
Extended High	SLC	11.8 x 5.1	13.5 x 7.7	75 x 75	49 to 60	1 x 1	Single (HH only)	3
	SGX	8 x 8	18.2 – 15.9 x 24.7			1 x 4		
	SGF	12.5 x 12.5						
	SSG, SPG	12.5 x 12.5						
Extended Low	SLC	8.0 x 5.1	9.0 x 7.7	170 x 170	10 to 23	1 x 1	Single (HH only)	3
	SGX	10 x 10	52.7 – 23.3 x 24.7			1 x 4		
	SGF	12.5 x 12.5						
	SSG, SPG	12.5 x 12.5						
Fine Quad-Pol	SLC	4.7 x 5.1	5.2 x 7.6	25 x 25	18 to 49	1 x 1	Quad (HH+VV+HV+VH)	3
	SGX	3.13 x 3.13	16.5 – 6.8 x 7.6					
	SSG, SPG	3.13 x 3.13						
Wide Fine Quad-Pol	SLC	4.7 x 5.1	5.2 x 7.6	50 x 25	18 to 42	1 x 1	Quad (HH+VV+HV+VH)	3
	SGX	3.13 x 3.13	17.3–7.8 x 7.6					
	SSG, SPG	3.13 x 3.13						
Standard Quad-Pol	SLC	8 or 11.8 x 5.1	9.0 or 13.5 x 7.6	25 x 25	18 to 49	1 x 1	Quad (HH+VV+HV+VH)	3
	SGX	8 x 3.13	28.6 – 17.7 x 7.6					
	SSG, SPG	8 x 3.13						
Wide Standard Quad-Pol	SLC	8 or 11.8 x 5.1	9.0 or 13.5 x 7.6	50 x 25	18 to 42	1 x 1	Quad (HH+VV+HV+VH)	3
	SGX	8 x 3.13	30.0 –16.7 x 7.6					
	SSG, SPG	8 x 3.13						
ScanSAR Narrow	SCN, SCF, SCS	25 x 25	81–38 x 40-70	300 x 300	20 to 46	2 x 2	Single Co or Cross (HH or VV or HV or VH) or Dual (HH+HV or VV+VH)	SCNA:4 SCNB:3
ScanSAR Wide	SCW, SCF, SCS	50 x 50	163–73 x 78-106	500 x 500	20 to 49	4 x 2	Single Co or Cross (HH or VV or HV or VH) or Dual (HH+HV or VV+VH)	4
Ship Detection (Detection of Vessels)	SCF	40 x 40	103-71 x 40-81	450 x 500	35 to 56	16 x 2 [8]	Single (HH only)	1
	SCS	20 x 20	33-23 x 19-77			5 x 1		
Ocean Surveillance	SCF	50 x 50	118-53 x 53-104	500 x 500	20 to 50	6 x 2 [8]	Single Co or Cross (HH or VV or HV or VH) or Dual (HH+HV or VV+VH)	2
	SCS	35 x 25	80-36 x 27-99			4 x 1		

NOTES:

1. Products available: Single Look Complex (SLC); Path Image Plus (SGX); Path Image (SGF); ScanSAR Narrow (SCN); ScanSAR Wide (SCW); ScanSAR Fine (SCF); ScanSAR Sampled (SCS); Map Image (SSG); Precision Map Image (SPG).
2. SLC, SGX, SGF, SCN, SCW, SCF and SCS are georeferenced and aligned with the satellite track. SSG and SPG are geocorrected on a map projection (SPG requires ground control points).
3. For SLC products the range pixel spacing is in radar slant range. For other georeferenced products (i.e. for ground range products) the range pixel spacing is in ground range. For geocorrected products the pixel spacings are in map projected coordinates (horizontal x vertical).
4. For SLC products the azimuth pixel spacing depends on the pulse repetition frequency.
5. Range resolution is in radar slant range for SLC products and ground range for all other products. Ground range resolution varies with incidence angle.
6. Actual scene size may vary with incidence angle.
7. Incidence angles above 50 degrees in the Spotlight and Ultra-Fine beam modes are not yet available commercially.
8. For Ship Detection and Ocean Surveillance modes, azimuth multi-looking of SCF products is done by spatial averaging and decimation by a factor of 2.
9. All modes and product characteristics are subject to change. Some restrictions may apply.
10. The RADARSAT-2 SAR sensor is extremely flexible and programmable post-launch; nominal resolution and swath width are examples of programmable characteristics. Custom and new beam modes will be introduced in response to client needs and market conditions.

Figure A-2. Summary of RADARSAT-2 beam mode and product characteristics (continue)

Source: RADARSAT-2 Product Description, 2016

Figure A-3. Nominal Resolutions in ScanSAR Narrow and ScanSAR Wide Beam Modes.

Source: RADARSAT-2 Product Description, 2016
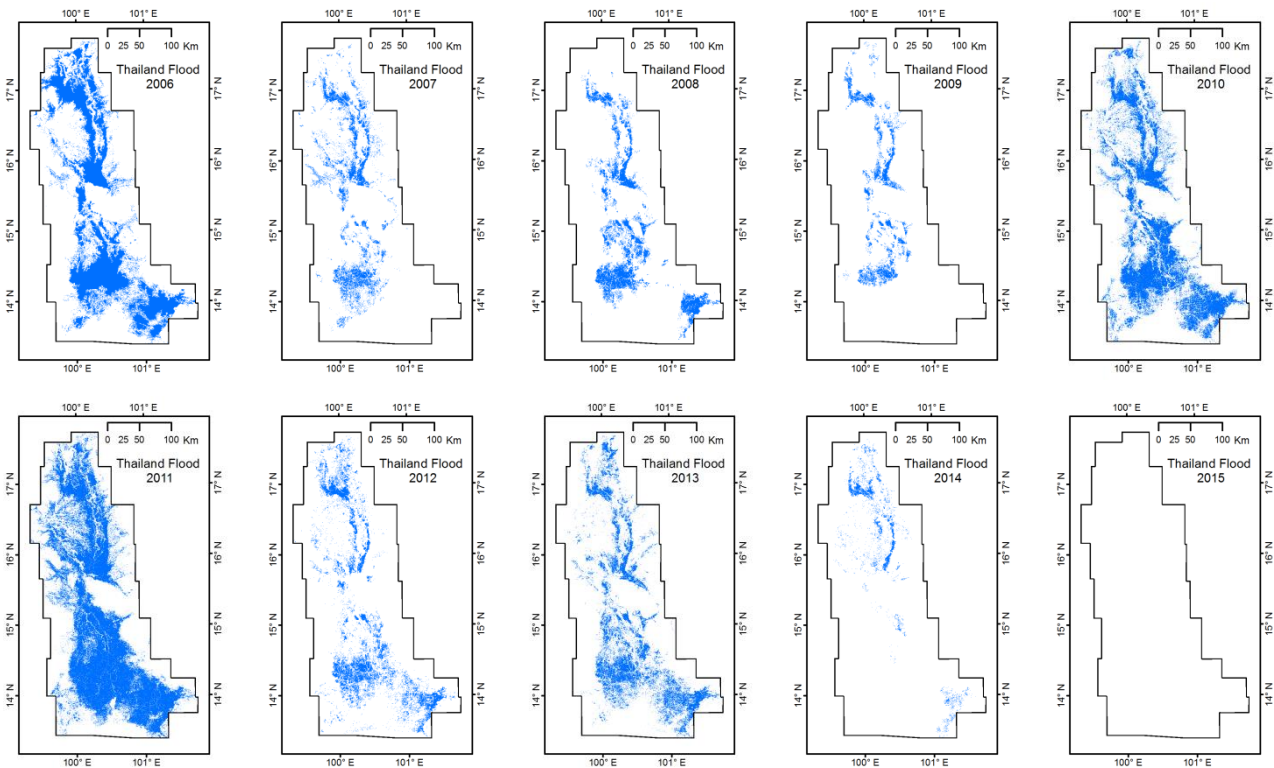
Figure A-4. The historical flood map of study area, Chao Phraya river basin in central Thailand provided by GISTDA, Thailand. These flood area were determined by manual thresholding of RADARSAT-1, RADARSAT-2, and COSMO-SkyMed.

APPENDIX B

This section shows the python codes used to process in this dissertation.

B.1 Python code for geometry transformation in general case

```python
import os
import numpy as np
import gdal, ogr, math

class JSON(dict):
    pass

class ogcPoint(np.ndarray):
    def __new__(cls, a):
        obj = np.asarray(a).view(cls)
        return obj

    def updateNumPyArrayWithValues(self):
        self[1] = 1
        return self
    @property
    def X(self):
        return self[0]
    @property
    def Y(self):
        return self[1]

class ogcEnvelope(np.ndarray):
    def __new__(cls, a):
        obj = np.asarray(a).view(cls)
        return obj

    def updateNumPyArrayWithValues(self):
        self[1] = 1
        return self
    @property
    def MinX(self):
        return self[0]
    @property
    def MaxX(self):
        return self[1]
    @property
    def MinY(self):
        return self[2]
    @property
    def MaxY(self):
        return self[3]
    #-----------
    @property
    def Size(self):
        return ogcPoint((self.MaxX-self.MinX,self.MaxY-self.MinY))
    @property
    def LowerLeft(self):
        return ogcPoint((self.MinX,self.MinY))
    @property
    def LowerRight(self):
        return ogcPoint((self.MaxX,self.MinY))
    @property
    def UpperLeft(self):
        return ogcPoint((self.MinX,self.MaxY))
    @property
    def UpperRight(self):
        return ogcPoint((self.MaxX,self.MaxY))


class ogcTransform(np.ndarray):
    _size = ogcPoint((0,0)) #image size
    def __new__(cls, a, size=(0,0)):
        obj = np.asarray(a).view(cls)
        obj._size = ogcPoint(size)
```

```python
        return obj

    def updateNumPyArrayWithValues(self):
        self[1] = 1
        return self

    @property
    def Size(self):
        return self._size
    @property
    def MinX(self):
        return self[0]
    @property
    def ResolutionX(self):
        return self[1]
    @property
    def OrientationX(self):
        return self[2]
    @property
    def MaxY(self):
        return self[3]
    @property
    def OrientationY(self):
        return self[4]
    @property
    def ResolutionY(self):
        return self[5]

    @property
    def Rows(self):
        return self.Size.Y
    @property
    def Columns(self):
        return self.Size.X
    @property
    def Pixels(self):
        return self.Size.X * self.Size.Y

    @property
    def MaxX(self):
        return self.MinX + (self.ResolutionX*self.Size.X)
    @property
    def MinY(self):
        return self.MaxY + (self.ResolutionY*self.Size.Y)
    @property
    def Width(self):
        return self.MaxX-self.MinX
    @property
    def Height(self):
        return self.MaxY-self.MinY
    @property
    def Envelope(self):
        return ogcEnvelope((self.MinX,self.MaxX,self.MinY,self.MaxY))
    #--------
    def PositionAt(self, RC):
        return ogcPoint((self.MinX + (self.ResolutionX * RC.X) + (self.OrientationX*RC.Y),
                         self.MaxY + (self.ResolutionY * RC.Y) + (self.OrientationY*RC.X)))
```

B.2 Python code for clipping raster by each polygon in vector files

```python
def CreateROI(Vector, Raster, Path, MustComplete=True):


    iRaster = gdal.Open(Raster)
    iVector = ogr.OpenShared(Vector)

    iLayer = iVector.GetLayer(0)
    iBand = iRaster.GetRasterBand(1)
    iTransf = ogcTransform(iRaster.GetGeoTransform(),(iRaster.RasterXSize,iRaster.RasterYSize))

    #iSchema = iLayer.GetLayerDefn()

    for i in range(iLayer.GetFeatureCount()):
        iFeature = iLayer.GetFeature(i)
```

```python
iID = iFeature.GetFieldAsInteger(iLayer.FindFieldIndex("ID",False))

iGeometry = iFeature.geometry()

#-------------------------------

iEnvelope = iTransf.Envelope
oEnvelope = ogcEnvelope((iGeometry.GetEnvelope()))

sEnvelope = ogcEnvelope((oEnvelope.MinX - iEnvelope.MinX,
                         oEnvelope.MaxX - iEnvelope.MinX,
                         -(oEnvelope.MaxY - iEnvelope.MaxY),
                         -(oEnvelope.MinY - iEnvelope.MaxY)))

pEnvelope = ogcEnvelope((sEnvelope / iTransf.ResolutionX).round().astype(np.int))


oEnvelope = ogcEnvelope((iEnvelope.MinX+(pEnvelope.MinX*iTransf.ResolutionX),
                         iEnvelope.MinX+(pEnvelope.MaxX*iTransf.ResolutionX),
                         iEnvelope.MaxY+(pEnvelope.MaxY*iTransf.ResolutionY),
                         iEnvelope.MaxY+(pEnvelope.MinY*iTransf.ResolutionY)))

oTransf = ogcTransform([oEnvelope.MinX,iTransf.ResolutionX, 0.0,
                        oEnvelope.MaxY,0.0, iTransf.ResolutionY])

#-------------------------------------------
iArray = iBand.ReadAsArray(int(pEnvelope.MinX),int(pEnvelope.MinY),
                           int(pEnvelope.Size.X),int(pEnvelope.Size.Y))

if type(iArray).__module__ != np.__name__:
    print ("#### Clip outside dataset")
    print (iArray)
    print (iEnvelope)
    print (iRaster.RasterXSize,iRaster.RasterYSize)
    print (int(pEnvelope.MinX),int(pEnvelope.MinY),
                        int(pEnvelope.Size.X),int(pEnvelope.Size.Y))
    continue #skip this aoi

#-------------------------------------------
oTarget = os.path.join(Path,"Water%03d"%(iID))

if not os.path.exists(oTarget):
    os.makedirs(oTarget)
oTarget = os.path.join(oTarget,os.path.split(Raster)[1].replace("Outer","Water%03d"%(iID)))
#"""
print (oTarget)
print (iArray.shape[1], iArray.shape[0],
       iRaster.RasterCount, iBand.DataType)

#-------------------------------------------
oRaster = iRaster.GetDriver().Create(oTarget,
     iArray.shape[1], iArray.shape[0],
     iRaster.RasterCount, iBand.DataType)

oRaster.SetProjection(iRaster.GetProjectionRef())
oRaster.SetGeoTransform(oTransf)
#oRaster.SetGCPs(iRaster.GetGCPCount(),iRaster.GetGCPs())
oRaster.SetMetadata(iRaster.GetMetadata())
#-------------------------------------------

print ("*"*30)
NotComplete = False
oMask = iArray!=iBand.GetNoDataValue() #Mask true for not nodata
print ("Masked pixels count : ",np.sum(oMask))

if np.sum(oMask) > 0:   #Not All Masked
    for pR in range(oMask.shape[0]):
        if NotComplete : break
        for pC in range(oMask.shape[1]):
            if NotComplete : break
            if not MustComplete and not oMask[pR][pC] :   continue

            iPoint = ogr.Geometry(ogr.wkbPoint)
            iLocate = iTransf.PositionAt(ogcPoint((pEnvelope.MinX+pC,pEnvelope.MinY+pR)))
            iPoint.AddPoint(*iLocate)
            iWithin = iPoint.Within(iGeometry)

            if MustComplete and iWithin and not oMask[pR][pC] :
                if not oMask[pR][pC] and oMask[pR-1:pR+2,pC-1:pC+2].sum()>=8:
```

```
                        oMask[pR,pC] = iWithin
                        print ("Fixed missing pixel as average pixels")
                        continue
                    else:
                        oMask.fill(False)
                        NotComplete = True
                        print ("Some nodata pixel is in clip polygon")
                        break

                oMask[pR][pC] = iWithin

                continue
                print (pR, pC, iArray[pR][pC])
                print (iPoint, oEnvelope)
                print ("-"*20)
                print (iPoint.Intersect(iGeometry))
        #-------------------------------------------

    for b in range(1,iRaster.RasterCount+1):
        #skip first band read from above doesn't work. Data from somewhere else
        #if b>1: #skip b1 by using read from above to improve speed

        iBand = iRaster.GetRasterBand(b)

        if b<=3:
            iArray = iBand.ReadAsArray(int(pEnvelope.MinX),int(pEnvelope.MinY),
                                    int(pEnvelope.Size.X),int(pEnvelope.Size.Y))
        else:
            iArrayA = iRaster.GetRasterBand(1).ReadAsArray(int(pEnvelope.MinX),
                        int(pEnvelope.MinY),int(pEnvelope.Size.X),int(pEnvelope.Size.Y))
            iArrayB = iRaster.GetRasterBand(2).ReadAsArray(int(pEnvelope.MinX),
                        int(pEnvelope.MinY),int(pEnvelope.Size.X),int(pEnvelope.Size.Y))
            iArray = 10*np.log10(np.power(10,iArrayA/10)+np.power(10,iArrayB/10))

        for pR in range(oMask.shape[0]):
            for pC in range(oMask.shape[1]):
                Marked = iArray[pR-1:pR+2,pC-1:pC+2]!=iBand.GetNoDataValue()
                if iArray[pR][pC]==iBand.GetNoDataValue() and Marked.sum()>=8:
                    iArray[pR,pC]=np.ma.masked array(iArray[pR-1:pR+2,pC-1:pC+2],~Marked).mean()
                    print ("Band",b,", Row",pR, ", Col", pC, ", Fixed", iArray[pR,pC])

        oBand = oRaster.GetRasterBand(b)
        oBand.SetNoDataValue(iBand.GetNoDataValue())
        iArray[~oMask] = oBand.GetNoDataValue()
        oBand.WriteArray(iArray)
    del oRaster
```

B.3 Python code for histogram peak detection

```
def peakdet(v, delta, x = None):
    """
    Source https://gist.github.com/endolith/250860
    Converted from MATLAB script at http://billauer.co.il/peakdet.html

    Returns two arrays

    function [maxtab, mintab]=peakdet(v, delta, x)
    %PEAKDET Detect peaks in a vector
    %        [MAXTAB, MINTAB] = PEAKDET(V, DELTA) finds the local
    %        maxima and minima ("peaks") in the vector V.
    %        MAXTAB and MINTAB consists of two columns. Column 1
    %        contains indices in V, and column 2 the found values.
    %
    %        With [MAXTAB, MINTAB] = PEAKDET(V, DELTA, X) the indices
    %        in MAXTAB and MINTAB are replaced with the corresponding
    %        X-values.
    %
    %        A point is considered a maximum peak if it has the maximal
    %        value, and was preceded (to the left) by a value lower by
    %        DELTA.

    % Eli Billauer, 3.4.05 (Explicitly not copyrighted).
    % This function is released to the public domain; Any use is allowed.

    """
```

```python
    maxtab = []
    mintab = []

    if x is None:
        x = np.arange(len(v))

    v = np.asarray(v)

    if len(v) != len(x):
        sys.exit('Input vectors v and x must have same length')

    if not np.isscalar(delta):
        sys.exit('Input argument delta must be a scalar')

    if delta <= 0:
        sys.exit('Input argument delta must be positive')

    mn, mx = np.Inf, -np.Inf
    mnpos, mxpos = np.NaN, np.NaN

    lookformax = True

    for i in np.arange(len(v)):
        this = v[i]
        if this > mx:
            mx = this
            mxpos = x[i]
        if this < mn:
            mn = this
            mnpos = x[i]

        if lookformax:
            if this < mx-delta:
                maxtab.append((mxpos, mx))
                mn = this
                mnpos = x[i]
                lookformax = False
        else:
            if this > mn+delta:
                mintab.append((mnpos, mn))
                mx = this
                mxpos = x[i]
                lookformax = True

    return np.array(maxtab), np.array(mintab)
```

B.4 Python code for automatic thresholding

```python
import os
import sys
import cv2

import math
import numpy as np
from osgeo import gdal
from datetime import datetime
from matplotlib import pyplot as plt
import collections as col

import warnings
warnings.simplefilter('ignore',np.RankWarning)

def FindBest(source):
    data_bin = 256
    stripSize = 500
    neighb_count = 7

    stripCount = math.ceil(source.YSize/stripSize)

    data_min = np.inf
    data_max = -np.inf

    for stripNo in range(stripCount):
        rowNo = stripNo*stripSize
        rowSize = stripSize
```

```python
        if rowNo+stripSize > source.YSize:
            rowSize = source.YSize - rowNo
        data_arr = source.ReadAsArray(0,rowNo,source.XSize,rowSize)
        data_arr = np.ma.masked_array(data_arr, data_arr==source.GetNoDataValue())

        #---------
        temp_arr = data_arr[~data_arr.mask].data.flatten()
        if len(temp_arr)==0: continue
        data_min = min(temp_arr.min(),data_min)
        data_max = max(temp_arr.max(),data_max)
        del data_arr
        del temp_arr

    print("min : ",data_min,"  max : ",data_max)
    if np.isinf(data_min) or np.isinf(data_max):
        results = col.OrderedDict()
        results["Threshold"] = {}  #at lower bound
        results["Bins"] = None
        results["Min"] = None
        results["Max" ] = None
        results["Range"] = None
        results["Interval"] = None
        results["Series"] = []
        results["Counts"] = []
        results["PolyFit"] = []
        results["PeakDet"] = {}
        return results


    data_8bit = np.zeros((source.YSize,source.XSize),dtype=np.uint8)
    data_8bit = np.ma.masked_array(data_8bit, data_8bit!=0)

    hist_count, hist_series = np.histogram(np.zeros(data_bin),data_bin,[data_min,data_max])
    hist_series = hist_series[:-1]
    hist_count = np.zeros(data_bin)


    for stripNo in range(stripCount):
        rowNo = stripNo*stripSize
        rowSize = stripSize
        if rowNo+stripSize > source.YSize:
            rowSize = source.YSize - rowNo
        data_arr = source.ReadAsArray(0,rowNo,source.XSize,rowSize)
        data_arr = np.ma.masked_array(data_arr, data_arr==source.GetNoDataValue())

        temp_arr = data_arr[~data_arr.mask].data.flatten()
        temp_count, hist_series = np.histogram(temp_arr,data_bin,[data_min,data_max])
        hist_count+= temp_count
        hist_series = hist_series[:-1]
        #---------
        temp_arr = (((data_arr-data_min)/(data_max-data_min))*(data_bin-1)).round()
        #print(rowNo) #,"\n",temp_arr)
        data_8bit[rowNo:rowNo+rowSize,0:source.XSize] = temp_arr
        data_8bit.mask[rowNo:rowNo+rowSize,0:source.XSize] = temp_arr.mask
        del data_arr
        del temp_arr

    flat_8bit = data_8bit[~data_8bit.mask].data.flatten()
    otsu_cv2, otsu_img = cv2.threshold(flat_8bit,0,data_bin-1,cv2.THRESH_BINARY+cv2.THRESH_OTSU)

    del flat_8bit
    del data_8bit
    """
    This code work well but no need
    http://docs.opencv.org/3.1.0/d7/d4d/tutorial_py_thresholding.html#gsc.tab=0

    Try to calculate by manual
    //http://www.labbookpages.co.uk/software/imgProc/otsuThreshold.html
    This following code not correct

    """
    """-------------------------------------------
    #*** Recheck with 8 bit ---- Remove when ok -----
    hist_count, hist_series = np.histogram(flat_8bit,256,[0,256])
    hist_series = hist_series[:-1]
    print("*******",len(flat_8bit),flat_8bit.min(), flat_8bit.max())
    print("*******",len(hist_count),hist_count.min(), hist_count.max())
    print("*******",len(hist_series),hist_series.min(), hist_series.max())
```

```python
print(hist_series)
#---------------------------------------------"""

""" Test Version with Between-Class"""
#http://www.labbookpages.co.uk/software/imgProc/otsuThreshold.html
hist_cumu = hist_count.ravel().cumsum()
hist_total = hist_cumu[-1]
#print("total",hist_total)

hist_valley = hist_count.ravel()/hist_total

otsu_min = np.inf
otsu_key = -1

otsu_max = -np.inf
otsu_key2 = -1

valley_max = -np.inf
valley_key = -1

neighb_shift = int(math.ceil(neighb_count-1/2))
neighb_max = -np.inf
neighb_key = -1

for i in range(data_bin):
    nL,nR = np.hsplit(hist_count,[i+1])   #number of items
    sL,sR = np.hsplit(hist_series,[i+1])  #value of items
    wL,wR = nL.sum()/hist_total, nR.sum()/hist_total #weight of side
    mL,mR = (nL*sL).sum()/nL.sum(), (nR*sR).sum()/nR.sum() #mean of side
    vL,vR = (((sL-mL)**2)*nL).sum()/nL.sum(), (((sR-mR)**2)*nR).sum()/nR.sum() #variance of side

    otsu_wic = (wL*vL)+(wR*vR) #within-class

    if otsu_wic < otsu_min:
        otsu_min = otsu_wic
        otsu_key = i

    otsu_btc = wL*wR*((mL-mR)**2)
    if otsu_btc > otsu_max:
        otsu_max = otsu_btc
        otsu_key2 = i
    """
    print("-"*30)
    print("M", mL, mR)
    print("V", vL, vR)
    print("WIC",i, otsu_key,  otsu_wic, otsu_min)
    print("BTC",i, otsu_key2, otsu_btc, otsu_max)
    """
     #-------------
    # calculate valley within-class
    valley_val = otsu_btc*(1-hist_valley[i])
    if valley_val > valley_max:
        valley_max = valley_val
        valley_key = i
    #print("Valley", valley_key, valley_val, valley_max)

    #-------------
    # calculate neighborhood within-class
    neighb_left = i - neighb_shift
    neighb_right = i + neighb_shift + 1
    neighb_val = otsu_btc* (1-hist_valley[neighb_left:neighb_right].sum())
    if neighb_val > neighb_max:
        neighb_max = neighb_val
        neighb_key = i
    #print("Neighbor",neighb_key, neighb_val, neighb_max)

hist_delta = int(round((polyfit_peakdet/100)*hist_count.sum()))
hist_coef = np.polyfit(hist_series, hist_count,50)
hist_poly = np.polyval(hist_coef, hist_series)
peaks, valls= peakdet(hist_poly, hist_delta ,hist_series)

results = col.OrderedDict()
results["Threshold"] = col.OrderedDict()
results["Threshold"]["OTSU-CV2"] = hist_series[int(otsu_cv2)]  #at lower bound
results["Threshold"]["OTSU-WIC"] = hist_series[int(otsu_key)]
results["Threshold"]["OTSU-BTC"] = hist_series[int(otsu_key2)]
results["Threshold"]["Valley-Emphasis"] = hist_series[int(valley_key)]
results["Threshold"]["Neighbor-Emphasis"] = hist_series[int(neighb_key)]
results["Bins"] = 256
```

```
results["Min"] = data min
results["Max" ] = data max
results["Range"] = data_max-data_min
results["Interval"] = hist_series[1]-hist_series[0]
results["Series"] = hist_series.tolist()
results["Counts"] = hist_count.astype(np.int).tolist()
results["PolyFit"] = hist_poly.tolist()
results["PeakDet"] = {"Delta":5,"Peaks": peaks.tolist(), "Valleys": valls.tolist() }

    return results
```

B.5 Python code for calculate MTR and Hyperboloid Change Index

```python
import os, sys
import traceback
import numpy as np
import numpy.ma as ma
import math, pickle
import matplotlib.pyplot as plt
from mpl_toolkits.mplot3d import Axes3D
from osgeo import gdal

def CorrDiff(Source,Target,bandBefore,bandAfter,WinSize,bandCorr=None):#,Progress):
        bandB     = Source.GetRasterBand(bandBefore) #Before
        bandA     = Source.GetRasterBand(bandAfter) #After
        bandC     = None
        if bandCorr: bandC = Source.GetRasterBand(bandCorr)

        bandSBefo = Target.GetRasterBand(1)
        bandSAfte = Target.GetRasterBand(2)
        bandTCorr = Target.GetRasterBand(3)
        bandTDiff = Target.GetRasterBand(4)
        bandTSumm = Target.GetRasterBand(5)
        bandNCorr = Target.GetRasterBand(6)
        bandNDiff = Target.GetRasterBand(7)
        bandNSumm = Target.GetRasterBand(8)
        bandHZscr = Target.GetRasterBand(9)

        """
        bandSBefo.SetCategoryNames("Source Before")
        bandSAfte.SetCategoryNames("Source After")
        bandTCorr.SetCategoryNames("R Correlation")
        bandTDiff.SetCategoryNames("Different")
        bandTSumm.SetCategoryNames("Summation")
        bandNCorr.SetCategoryNames("Norm R Correlation")
        bandNDiff.SetCategoryNames("Norm Different")
        bandNSumm.SetCategoryNames("Norm Summation")
        bandHZscr.SetCategoryNames("+/-Root(Hyperboloid)")
        """

        bandSBefo.WriteArray(bandB.ReadAsArray())
        bandSAfte.WriteArray(bandA.ReadAsArray())

        centerX = int(WinSize[0]/2.)
        centerY = int(WinSize[1]/2.)
        extendX = int(WinSize[0]/2.)
        extendY = int(WinSize[1]/2.)

        stepCount = 0.
        stepPrint = 0.
        stepTotal = float(bandB.XSize*bandB.YSize)

        for j in range(centerY,bandB.YSize-centerY-1):
            for i in range(centerX,bandB.XSize-centerX-1):
                    #print bandB.XSize,bandB.YSize, i-extendX,j-extendY,i+extendX,j+extendY
                    winsBData = bandB.ReadAsArray(i-extendX,j-
                            extendY,WinSize[0],WinSize[1]).flatten()
                    winsAData = bandA.ReadAsArray(i-extendX,j-
                            extendY,WinSize[0],WinSize[1]).flatten()

                    if bandC:
                        winsTCorr = bandC.ReadAsArray(i,j,1,1)[0][0]
                        #print "Coherence",winsTCorr
                    else:
```

```python
                winsTCorr = np.corrcoef(winsBData,winsAData)
                winsTCorr = winsTCorr[0,1]
                #print "Correlation",winsTCorr

            #After - Before
            winsBMean = np.average(winsBData)
            winsAMean = np.average(winsAData)

            ###if Rsquare: winsTCorr**=2
            winsTDiff = winsAMean - winsBMean
            winsTSumm = winsAMean + winsBMean

            bandTCorr.WriteArray(np.array([[winsTCorr]]),i,j)
            bandTDiff.WriteArray(np.array([[winsTDiff]]),i,j)
            bandTSumm.WriteArray(np.array([[winsTSumm]]),i,j)

            if (i==centerX and j==centerY):
                print i-extendX,j-extendY, WinSize
                print "Data1 : ",winsBData
                print "Data2 : ",winsAData
                print "AverageB : ",winsBMean
                print "AverageA :",winsAMean
                print "CorrCoef : ",winsTCorr
                print "Different:",winsTDiff
                print "Summation:",winsTSumm

            stepCount = stepCount+1.
            sys.stdout.write("\r"+
            " %02d"%WinSize[0]+"x"+"%02d"%WinSize[1]+
            " Progress %s ... %0.2f"%(j,((stepCount/stepTotal)*100.))+"%")
            sys.stdout.flush()
print
print "Moving Window Complete !!!"
print

print "Compute Statistics for Raw Corr,Diff,Summ"
bandSBefo.ComputeStatistics(False)
bandSAfte.ComputeStatistics(False)
bandTCorr.ComputeStatistics(False)
bandTDiff.ComputeStatistics(False)
bandTSumm.ComputeStatistics(False)

statSBefo = bandSBefo.GetStatistics(False,True)
statSAfte = bandSAfte.GetStatistics(False,True)
statTCorr = bandTCorr.GetStatistics(False,True)
statTDiff = bandTDiff.GetStatistics(False,True)
statTSumm = bandTSumm.GetStatistics(False,True)

statMin = 0; statMax = 1; statAvg = 2; statStd = 3

print "Corr Stat Raw Befo", statSBefo
print "Corr Stat Raw Afte", statSAfte
print
print "Corr Stat Raw Corr", statTCorr
print "Corr Stat Raw Diff", statTDiff
print "Corr Stat Raw Summ", statTSumm

numpTCorr = bandTCorr.ReadAsArray()
numpTDiff = bandTDiff.ReadAsArray()
numpTSumm = bandTSumm.ReadAsArray()

numpTCorr = ma.masked_array(numpTCorr,numpTCorr==-9999)
numpTDiff = ma.masked_array(numpTDiff,numpTDiff==-9999)
numpTSumm = ma.masked_array(numpTSumm,numpTSumm==-9999)

#Compute each row to reduce using of memory
for row in range(numpTCorr.shape[0]):
    numpTCorr[row]-=statTCorr[statAvg]
    numpTCorr[row]/=(statTCorr[statStd]*2.)
    numpTDiff[row]-=statTDiff[statAvg]
    numpTDiff[row]/=(statTDiff[statStd]*2.)
    numpTSumm[row]-=statTSumm[statAvg]
    numpTSumm[row]/=(statTSumm[statStd]*2.)

bandNCorr.WriteArray(numpTCorr.base)
bandNDiff.WriteArray(numpTDiff.base)
bandNSumm.WriteArray(numpTSumm.base)

print "\nCompute Statistics for Norm's Corr,Diff,Summ"
```

```
        bandNCorr.ComputeStatistics(False)
        bandNDiff.ComputeStatistics(False)
        bandNSumm.ComputeStatistics(False)

        statNCorr = bandNCorr.GetStatistics(False,True)
        statNDiff = bandNDiff.GetStatistics(False,True)
        statNSumm = bandNSumm.GetStatistics(False,True)

        print
        print "Corr Stat Norm Corr", statNCorr
        print "Corr Stat Norm Diff", statNDiff
        print "Corr Stat Norm Summ", statNSumm

        #Compute each row to reduce using of memory
        for row in range(numpTCorr.shape[0]):
            #Hyperboloid Index
            numpTCorr[row]**=2.
            numpTDiff[row]**=2.
            numpTSumm[row]**=2.
            numpTCorr[row]+=numpTDiff[row]
            numpTCorr[row]-=numpTSumm[row]
            #+/- Root(Hyperboloid)
            numpTSign = ma.absolute(numpTCorr[row])
            numpTSign = numpTCorr[row]/numpTSign
            numpTCorr[row]=ma.absolute(numpTCorr[row])
            numpTCorr[row]**=0.5
            numpTCorr[row]*=numpTSign

        bandHZscr.WriteArray(numpTCorr.base)
        print "\nCompute Statistics for Hyperboloid Score"
        bandHZscr.ComputeStatistics(False)
        print "\nBuild Overviews ..."
        Target.BuildOverviews('average', [2, 4, 8,16,32,64])
```